SAIC-00/8005:APPAT-239
March 22, 2000

THE STRUCTURE AND DYNAMICS OF THE SOLAR CORONA

NASA SPACE PHYSICS THEORY
NAS5-96081

Third Year (Final) Progress Report

Covering the period June 16, 1998 - August 15, 1999

Science Applications International Corporation
An Employee-Owned Company

Submitted by

ZORAN MIKIC

PRINCIPAL INVESTIGATOR:

SCIENCE APPLICATIONS INTERNATIONAL CORPORATION

10260 CAMPUS POINT DRIVE

SAN DIEGO, CA 92121-1578

MARCH 22, 2000

THIRD YEAR (FINAL) PROGRESS REPORT

This report covers technical progress during the third year of the NASA Space Physics Theory contract "The Structure and Dynamics of the Solar Corona," NAS5-96081, between NASA and Science Applications International Corporation, and covers the period June 16, 1998 to August 15, 1999. This is also the final report for this contract. Under this contract SAIC, the University of California, Irvine (UCI), and the Jet Propulsion Laboratory (JPL), have conducted research into theoretical modeling of active regions, the solar corona, and the inner heliosphere, using the MHD model. During the three-year duration of this contract we have published 49 articles in the scientific literature. These publications are listed in Section 3 of this report. In the Appendix we have attached reprints of selected articles.

In the following sections we summarize our progress during the third year of the contract. Full descriptions of our work can be found in the cited publications, a few of which are attached to this report.

1. PROGRESS REPORT

Predicting the Structure of the Solar Corona for the August 11, 1999 Eclipse

We have used our polytropic 3D MHD model to predict the structure of the solar corona during the total solar eclipse that occurred on August 11, 1999. Our coronal prediction was posted prior to the eclipse on the World Wide Web:

`http://haven.saic.com/corona/modeling.html`

This prediction is our fourth in a series (previous predictions were made for the total solar eclipses in 1995, 1997, and 1998, as detailed on our Web page). The distinguishing feature of this prediction is that it occurred at a time when we were approaching solar maximum, so that the complexity of the Sun is much greater than for our previous predictions. This prediction was presented at the conference "The Last Total Solar Eclipse of the Millennium," which was held in Istanbul, Turkey, August 13–15, 1999. Z. Mikić also witnessed the eclipse in Elazig, Turkey. A manuscript detailing the comparison was submitted for publication in the proceedings of this conference, and will be included in a future progress report. The comparison of our prediction and actual eclipse images is reasonably good. Figure 1 shows images of the predicted coronal polarized brightness, as well as the magnetic field line structure, and a comparison of the prediction with an image of the corona taken by Fred Espenak in Turkey. This coronal simulation is also being used to study the magnetic field as we approach solar maximum, as well as to compare with SOHO, WIND, and Ulysses solar wind observations. A preprint of past comparisons of our MHD model with eclipse observations has been published (Mikić *et al.* 1999), and is included in the Appendix.

Fast Magnetic Reconnection in a 2D "Rosette" Configuration

In conjunction with Dr. Samuel Vainshtein of the University of Chicago, we are studying the 2D reconnection of magnetic fields in a "rosette" topology in search of fast magnetic

Comparison of a 3D MHD Coronal Prediction with an Image of the 11 August 1999 Total Solar Eclipse

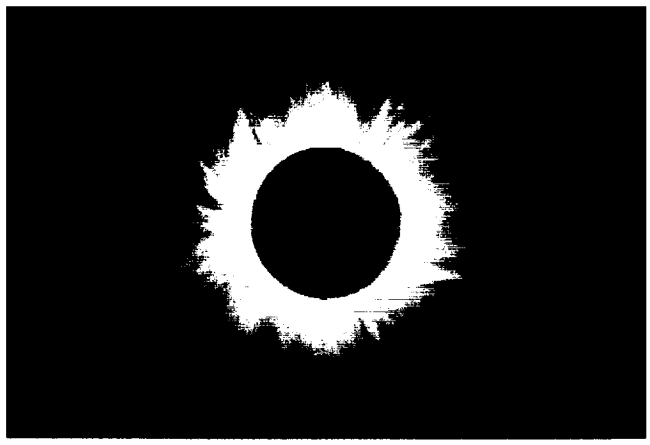

Fred Espenak's Composite Image (Turkey)

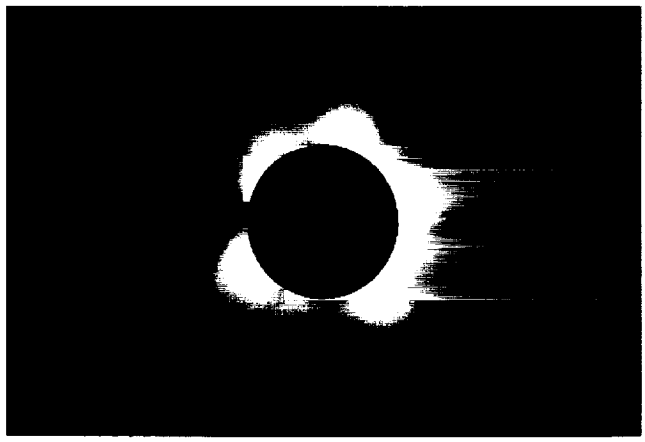

Predicted Polarization Brightness (MHD Model)

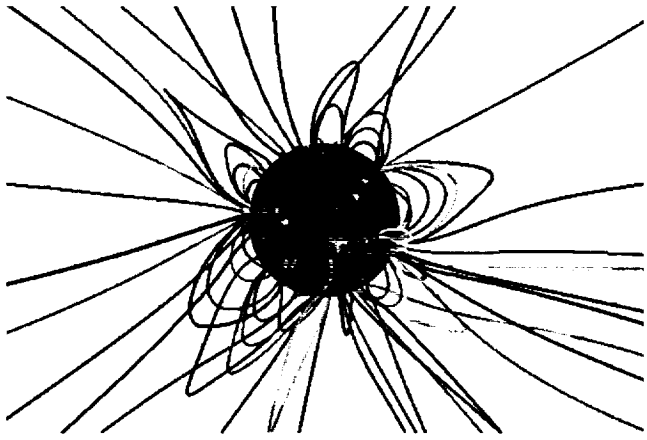

Predicted Magnetic Field Lines (MHD Model)

Figure 1. Comparison between a composite eclipse image created from photographs taken by Fred Espenak in Lake Hazar, Turkey (top) with the predicted polarization brightness of the simulated solar corona from our 3D MHD model (middle). The projected magnetic field lines from the model are also shown (bottom). Terrestrial (geocentric) north is vertically upward. The eclipse image is copyrighted 1999 by Fred Espenak.

reconnection. This is a follow-on to the work reported in the second quarter of this year in which we investigated the formation of a tangential discontinuity in the ideal MHD model. Fast reconnection is defined as one whose rate is weakly dependent on the magnitude of the plasma resistivity. We have found that, if the plasma viscosity is kept small enough, fast reconnection may occur. A series of simulations with $\eta = \nu = 2.5 \times 10^{-5}$, 5×10^{-5}, 10×10^{-5}, and 20×10^{-5} (where η and ν are the plasma resistivity and viscosity, respectively) show that the reconnection rate is almost independent of the resistivity. We are continuing these promising simulations to confirm that the reconnection rate is indeed fast. If this is confirmed, this work would have impact on the applicability of reconnection as an energy release mechanism for coronal heating and solar flare initiation.

Figure 2 shows the reconnection of two current-carrying flux bundles for the case when $\eta = \nu = 5 \times 10^{-5}$. Note that the two flux bundles reconnect in a time that is Alfvénic.

Modeling the "Whole Sun Month" Corona with Improved Thermodynamics

In the previous annual report we described our modeling efforts for the Whole Sun Month (WSM) time period (Aug. 10–Sep. 8, 1996). A paper on this work has been published (Linker *et al.* 1999), and is included in the Appendix. For our first 3D computation with our improved thermodynamic model, we recomputed the WSM case. The new calculation results in more realistic coronal temperatures, as shown in Figure 3. The improved thermodynamic description in our MHD model opens up the possibility of modeling disk emission, just as we have previously done for polarization brightness (pB). The more realistic temperature obtained from the solution can be used to predict the abundance of the coronal iron species and produce "simulated" EIT images. Figure 4a shows an FeXV 284Å EIT image on August 27, 1996, while Figure 4b shows a simulated EIT image that was developed for this time period using the plasma parameters from the MHD computation. The simulated image reproduces the extension of the coronal hole past the solar equator, and also the small coronal hole in the south. The width of the dark emission region is much wider in the simulated image than in the EIT image; this may in part be due to the limited longitudinal resolution that was used for the computation. The active region also does not appear very bright in the simulated image, which may indicate that the coronal heating function used was too simple. Further comparisons of this type can help us to improve the MHD model as well as constrain models of coronal heating.

Including the Transition Region in 2D MHD Models of the Solar Wind

The simplified energy equation in polytropic MHD models fails to reproduce the temperature structure of the corona and the observed contrast in speed between the fast and slow solar wind. We have recently improved the energy equation in our MHD model by including thermal conduction parallel to the magnetic field, radiation, coronal heating, and Alfvén wave pressure. We have also extended our model to include the transition region in our coronal calculations. Our lower boundary is placed at the top of the chromosphere (at a temperature of 20,000°K), so that the transition region is included in the domain of calculation. We specify a magnetic flux distribution on the solar surface and we integrate the time-

Fast MHD Reconnection in a Rosette Configuration

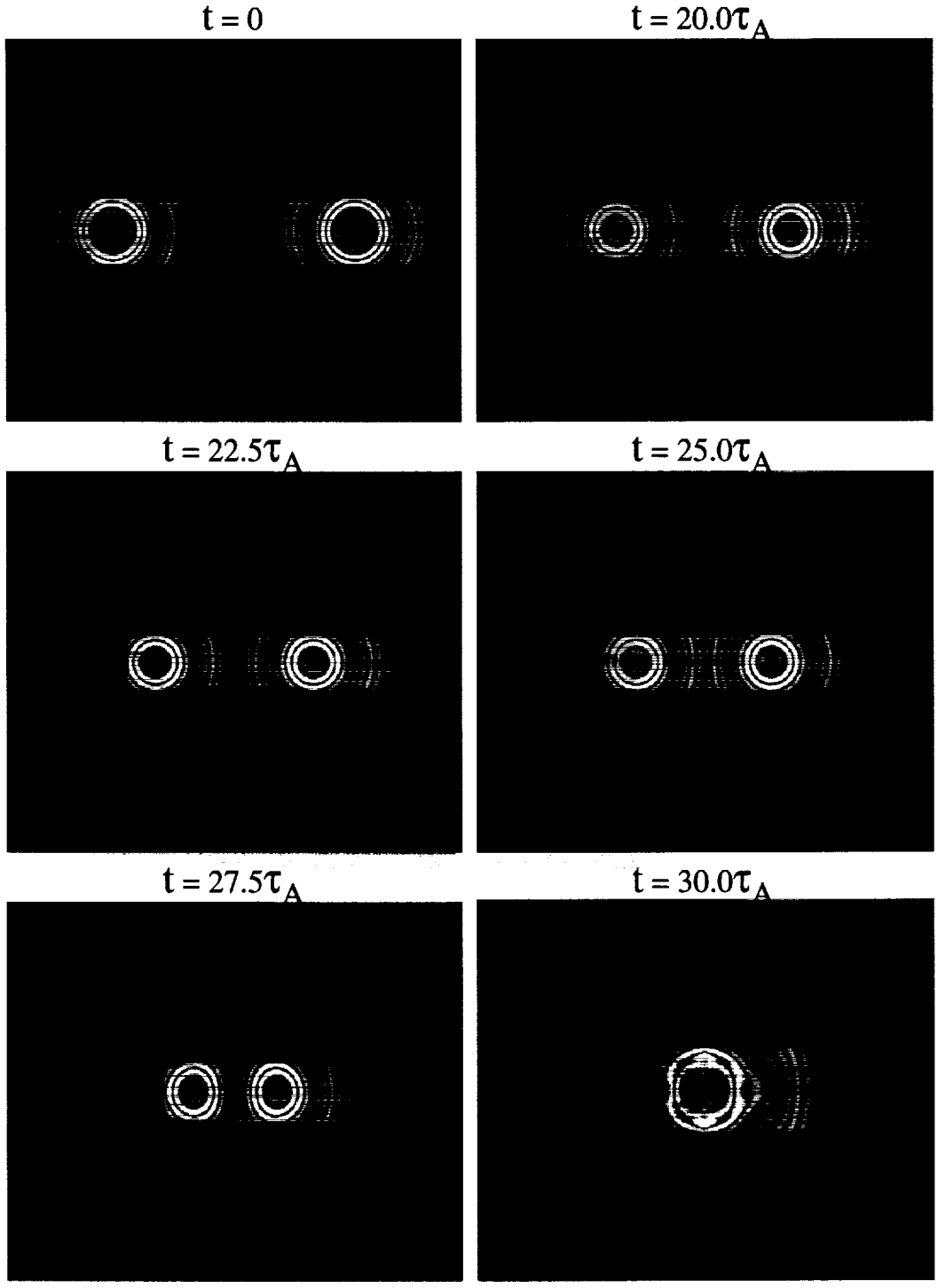

Figure 2. Reconnection of two current–carrying flux bundles. The time it takes to reconect the magnetic flux is on the order of the Alfven time.

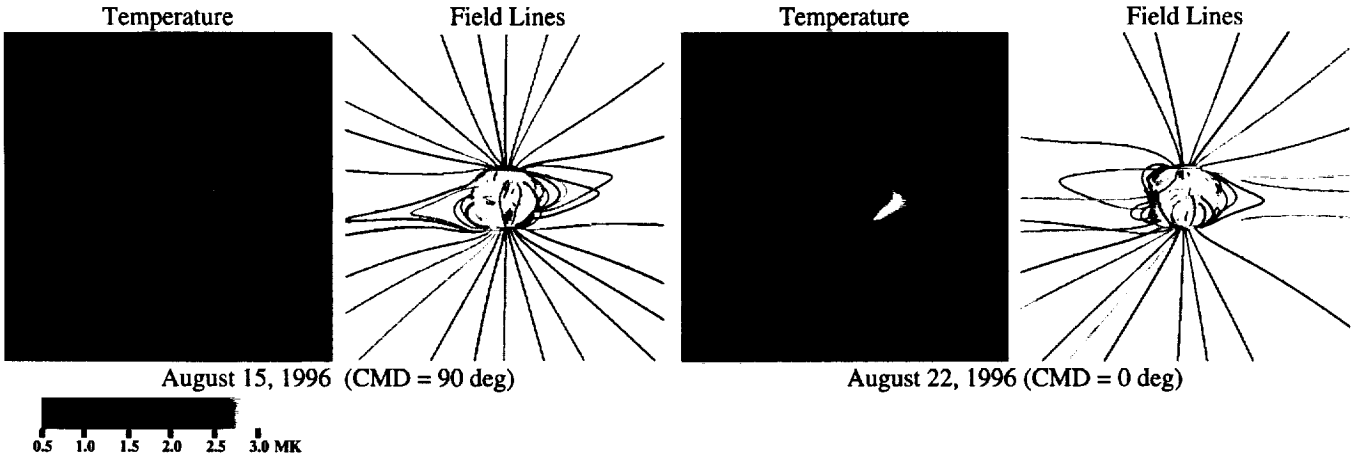

Figure 3. The temperature in the corona for the model with an improved energy equation. Note that the closed–field regions (streamers) have higher temperatures, and the polar coronal holes have low temperatures.

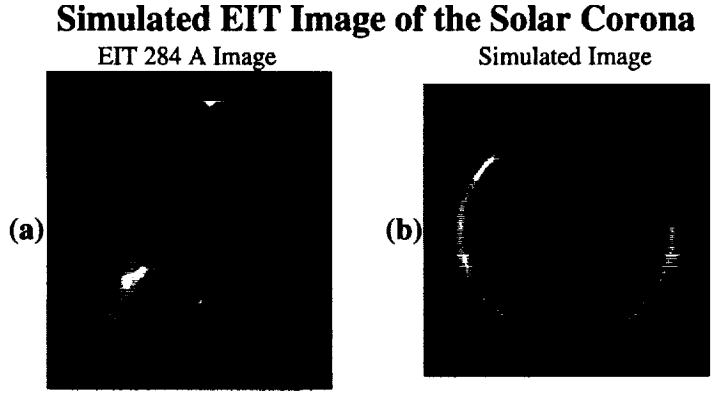

Figure 4. A comparison between (a) observed EUV emission at 284A from the SOHO EIT telescope and (b) a simulated emission image using plasma parameters from the MHD model.

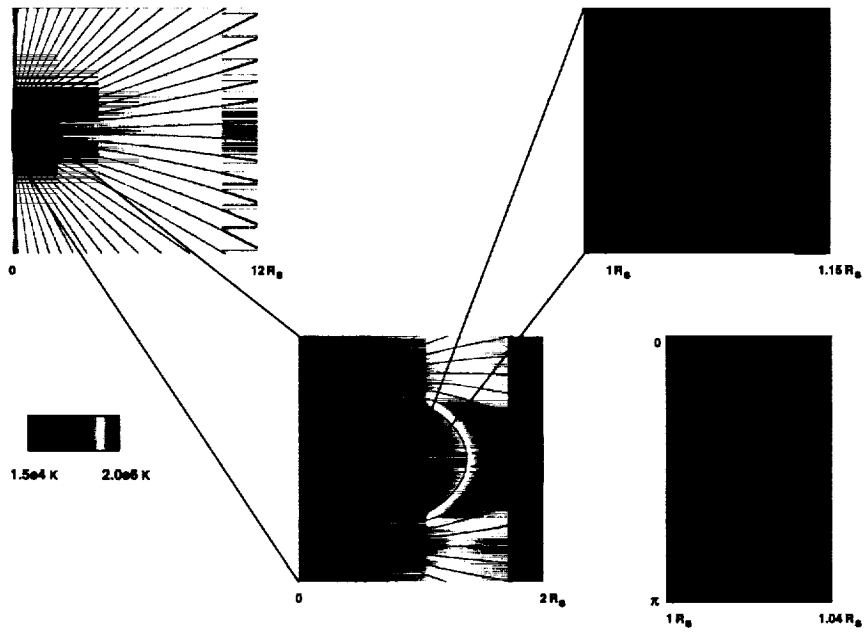

Figure 5. The plasma temperature (T) in the solar corona from an MHD simulation that includes the upper chromosphere and transition region. Also shown are magnetic field lines. Blue shows the lowest temperatures and red the highest. T varies from less than 20,000 K in the upper chromosphere to more than 2,000,000 K in the corona.

dependent MHD equations to steady state. The resulting solutions can be used to compare with the properties of the corona and of the solar wind. In this model, the solar wind is described self-consistently from its origins in the top of the chromosphere all the way out as it expands into interplanetary space.

We have performed 2D (axisymmetric) MHD simulations of the solar corona, including the transition region, for a dipole magnetic flux distribution. This is a challenging computation because quantities vary by many orders of magnitude across short length scales in the transition region (down to $0.0005R_S$). To model the transition region, we have incorporated several enhancements to our MHD code, including a more sophisticated treatment of the characteristic equations at the solar boundary, and an implicit advancement of the radiation loss term in the energy equation.

Figure 5 shows the temperature at increasingly smaller scales with superimposed magnetic field lines. The temperature maximum of about 2×10^6 K is in the closed field regions under the streamer, where hot plasma is trapped by the magnetic field. Notice that the simulation is able to capture the sharp gradients in the transition region. A projection in Cartesian coordinates shows that the height at which the transition region forms varies with latitude. We presented a poster paper at the American Astronomical Society Meeting (Solar Physics Division), held in Chicago, Illinois, May 31–June 3, 1999, on "MHD Modeling of the Solar Wind Including the Transition Region," by R. Lionello, J. A. Linker, and Z. Mikić.

Modeling the Eruption of Arcades by Changes in Magnetic Flux

Magnetic structures of various geometries, including loops and arcades, are present in the solar corona. Observations indicate that the magnetic field in some of these structures can be highly sheared, implying that a substantial amount of non-potential field energy is stored in the structure. If there is a physical mechanism that can induce a transition to a lower-energy state, the magnetic energy can be released into kinetic energy of plasma motions or thermal energy. We have studied the interactions between highly sheared structures (loops and arcades) and an emerging potential field structure by 3D numerical simulations. We found that the emerging field can destabilize an existing configuration, leading to the release of magnetic energy into plasma kinetic energy. A specific example is the eruption along the neutral line of a long, narrow, sheared arcade, which can be used to model a prominence eruption or a coronal mass ejection.

We presented our progress at a contributed talk and a poster paper at the American Astronomical Society Meeting (Solar Physics Division), held in Chicago, Illinois, May 31–June 3, 1999. The talk was on the "Initiation of Coronal Mass Ejections by Changes in Photospheric Flux," by Z. Mikić and J. A. Linker. The poster paper was on "Eruption of Magnetic Structures in the Solar Corona," by Y. Mok, Z. Mikić, and J. A. Linker.

Publication on Modeling of the Magnetic Structure of Prominences

A paper that explores the three-dimensional magnetic field topology for prominence support has been published in the *Astrophysical Journal* (Amari *et al.* 1999), and is included in the Appendix.

Presentation at the "Workshop on Physics of the Solar Corona and Transition Region," Monterey, California

We have investigated the effect of changes in photospheric magnetic fields on the stability of helmet streamers and active region arcades. Changes in the magnetic flux in the vicinity of the neutral line can lead to disruption, with liberation of a significant fraction of the stored magnetic energy. When the amount of emerged flux is below a threshold, a stable equilibrium with a filament results. When the threshold is exceeded, the configuration erupts and leaves the Sun with a substantial amount of kinetic energy. This mechanism is a promising trigger for launching CMEs. The results were presented in an invited talk at the Workshop on the Physics of the Solar Corona and Transition Region, held in Monterey, California, from 24–27 August, 1999, in the talk "Modeling the Evolution of the Coronal Magnetic Field," by Z. Mikić, J. A. Linker, and T. Amari.

Reconstructing Force-Free Fields in the Corona

During a visit by Dr. Tahar Amari (Ecole Polytechnique, Paris) to SAIC in July–August 1999, we collaborated on techniques to deduce coronal magnetic fields from vector magnetograph measurements of the magnetic field in the photosphere, using the force-free assumption. A paper on the mathematical aspects of a technique developed by Dr. Amari (Amari, Boulmezaoud, & Mikić 1999), with our collaboration, is included in the Appendix.

Emergence and Interaction of Coronal Loops

Recent observations from TRACE and SOHO indicate that magnetic loops are ubiquitous in the solar atmosphere. This discovery underscores the importance of understanding the dynamics and the potential consequences of these loops in the corona, as it is well known that dynamical events, such as solar flares, are often associated with these loops in active regions. Furthermore, how multiple loops form and coexist in a neighborhood is of fundamental importance because their interaction among each other could lead to the change of magnetic topology, resulting in the release of stored magnetic energy, which is believed to be the energy source of many dynamical phenomena. In our previous work, we have demonstrated a mechanism that leads to the dynamic formation of these loops, namely, by vortex plasma flows on the photosphere (Van Hoven *et al.* 1995). We have extended this loop formation study into the direct emergence of current-carrying loops from the photosphere. The physical mechanism and numerical method have been developed to show that a current-carrying loop with the observed properties can be dynamically formed in our proposed model (Mok *et al.* 1997). By modeling the time-dependent, normal components of the emerging loop's magnetic field and

current density on the surface, we showed that the coronal field responds dynamically by forming a rising current carrying loop as if it emerges through the surface.

A natural extension of this study is into an environment with multiple loops, such as those observed recently. In order to understand the dynamics of the multiple-loop configuration, we started by investigating a system of two loops, one loop emerging from the surface into a background with an existing overlying loop of comparable size and total flux in the neighborhood. This situation is not uncommon in an active region, where magnetic flux emerges frequently in the form of flux ropes. Using the same technique that we developed for the single-loop emergence, we simulated the formation of the second loop in a number of configurations. Due to the fact that the parameter space is quite large even for a two-loop combination as shown below, we have studied only the cases that we believe will have a potential impact on the environment. In our study, each loop has a dominant toroidal magnetic-field component, and a poloidal component generated by the toroidal current. We found that the interaction of a two-loop system has four major critical parameters:

(1) The angle between the two loop planes: we have studied three angles, i.e., 18 degrees, 45 degrees and 80 degrees.

(2) The relative direction of the toroidal magnetic fields: they can be "parallel" ($\mathbf{B}_1 \cdot \mathbf{B}_2 > 0$), or "anti-parallel" ($\mathbf{B}_1 \cdot \mathbf{B}_2 < 0$).

(3) The relative direction of the toroidal current densities: they can be parallel ($\mathbf{J}_1 \cdot \mathbf{J}_2 > 0$, or anti-parallel ($\mathbf{J}_1 \cdot \mathbf{J}_2 < 0$). The combination of (2) and (3) determines the relative sign of magnetic helicity of the loops, i.e., whether they have the same sign or opposite sign.

(4) The aspect ratios of the two loops and the relative size between their magnetic and current minor radii.

The interaction in some of these combinations releases more magnetic energy than others on a shorter time scale, resembling a solar flare, although most of the combinations do not result in a violent interaction. The simulations start with a single magnetic loop, which has emerged and settled into an equilibrium state as discussed above. The results of one the most dynamical cases are described as follows. The second loop emerges underneath with a time scale that is long compared to the Alfvén transition time along the loop in order to preserve the time scale ordering in the corona. One of the most dynamic cases is when the two loops are at 45 degrees with respect to each other. The toroidal magnetic field of the two are in opposite directions, i.e., $\mathbf{B}_1 \cdot \mathbf{B}_2 < 0$, while their toroidal current densities are in the same direction, i.e., $\mathbf{J}_1 \cdot \mathbf{J}_2 > 0$. In other words, the loops have opposite sense of magnetic helicity. The (magnetic) aspect ratios of the loops are 3.3 and 6.6 respectively, while the radii of the current channel are half of the (minor) magnetic radii. The total magnetic fluxes of the two loops are the same. The time profile of the kinetic energy in the system is shown in Figure 6. The second loop begins to emerge at $t = 300$, when the first loop has reached equilibrium. After the decay of some initial disturbances, the kinetic energy rises on a time scale of 40 normalized Alfvén times, compared

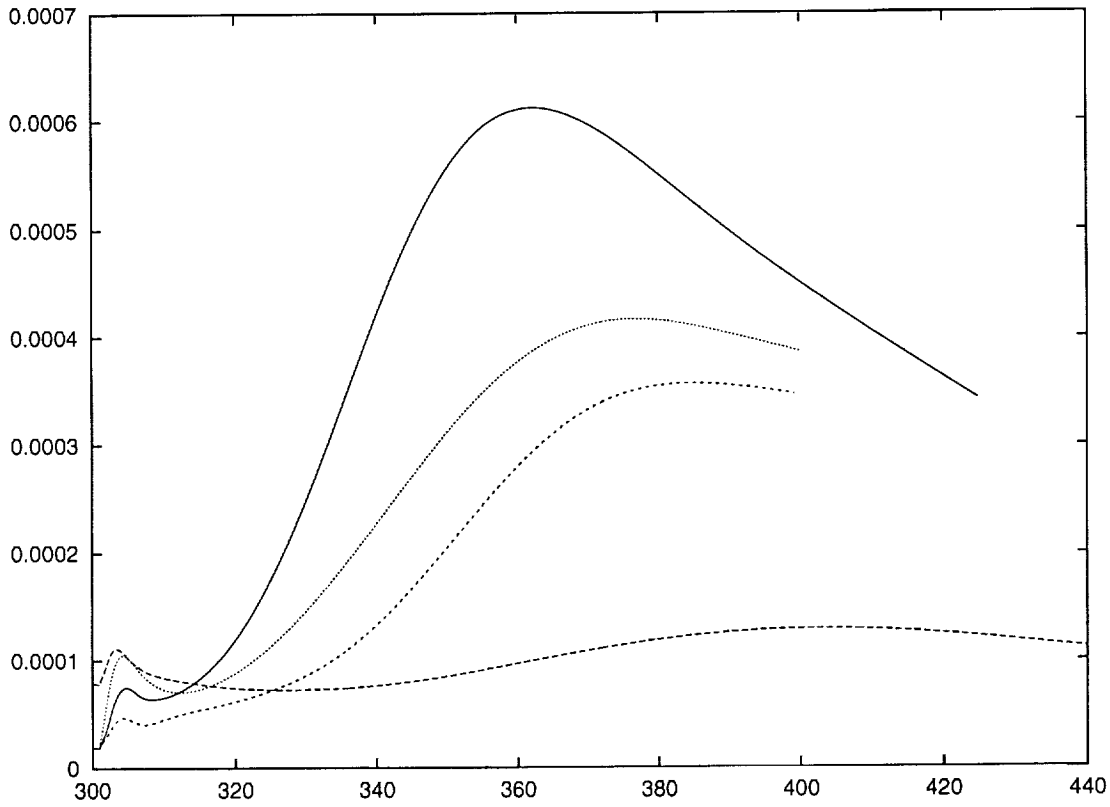

Figure 6. Time profile of kinetic energy released from the magnetic field. The solid curve corresponds to the case described in the text. The next three (lower) curves correspond to the cases with (18 degrees, $\mathbf{B}_1.\mathbf{B}_2 > 0$, $\mathbf{J}_1.\mathbf{J}_2 > 0$),(18 degrees, $\mathbf{B}_1.\mathbf{B}_2 < 0$, $\mathbf{J}_1.\mathbf{J}_2 > 0$), and (80 degrees, $\mathbf{B}_1.\mathbf{B}_2 < 0$, $\mathbf{J}_1.\mathbf{J}_2 < 0$).

to the rise time of 200 of the emerging field. Taking the nominal values of B = 200 Gauss, $n = 5 \times 10^8/\text{cm}^3$, major-radius = 10^9 cm, the Alfvén transit time along the loop is ~ 10 seconds, and the time scale of the kinetic energy burst is ~ 21 seconds. Although the rise time of the emerging field in the simulations is somewhat faster than observations indicate, we believe that it is sufficiently slow to keep it separated from the kinetic energy rise time, so that the simulations do not consume excessive computer time. The total kinetic energy at its maximum is 2.4×10^{28} erg, an appropriate amount for a small flare. The kinetic energy is contributed mostly by the horizontal velocity components. This is indicative of field line reconnection in the location where the rising apex of the emerging loop collides with the existing flux of the overlying loop. Since the toroidal components of **B** from the two loops have nearly opposite direction, the sharply bent reconnected field lines carry the plasma away from the reconnecting site in the classical FKR geometry. The interaction of the two structures takes place rather early, i.e., as soon as the apex of the emerging loop rises into the corona and is still at a distance from the major axis of the first loop. The evolution of the structure is shown in the sequence of Figure 7. The field lines gradually settle into a three-loop system. This interaction is a viable mechanism for the formation of multiple-loop configurations as recently observed in TRACE. The time profiles of several other cases are also shown in Figure 6. They typically evolve slowly into a new configuration with three to four loops connecting the four magnetic poles on the surface.

Although a solar flare is a highly dynamical event and requires kinetic theory for a full treatment of the physical processes, such as particle acceleration, we have demonstrated that a substantial amount of stored magnetic energy is available to be released within the MHD framework. Exactly how the energy is converted into other forms, such as accelerated particles, X-rays, EUV, and microwaves, remains an open question and needs to be investigated. The results of this study are presently being prepared for publication (Mok, Mikić, & Linker 2000).

Massively Parallel Version of the MAS Code

During this year, we have spent a significant effort to port our spherical 3D MHD code (MAS) to massively parallel computers. This task was driven by the fact that high performance computing is being performed on massively parallel architectures. MAS is a FORTRAN 77 code that was originally designed to run on vector supercomputers.

The parallelization of a large scalar code can be accomplished in two fundamentally different ways: a) the code is entirely redesigned and rewritten from scratch, or b) the existing code is converted to the new architecture with the minimum number of modifications. After careful deliberation, we determined that the second approach would be most efficient.

The Parallel Data Structure

The parallel code was designed for a distributed-memory machine using the message-passing interface (MPI). The parallelization is obtained by considering a decomposition of the spatial domain and by assigning each sub-domain to a different processor. In other words, each processor stores in its memory and performs computations only on data that refer to a fraction

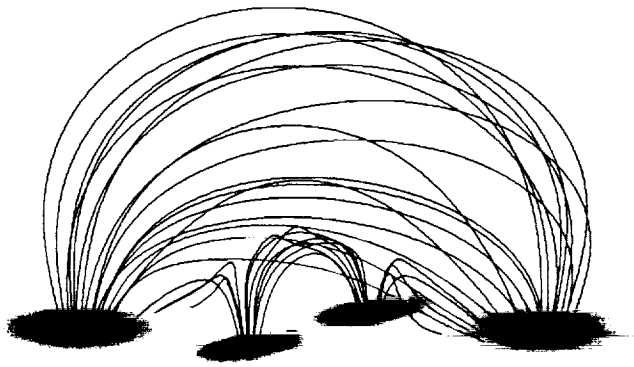

Figure 7a. Field lines at t = 325. The second loop (center) is emerging, and some of its field lines have reconnected to those of the outer loop.

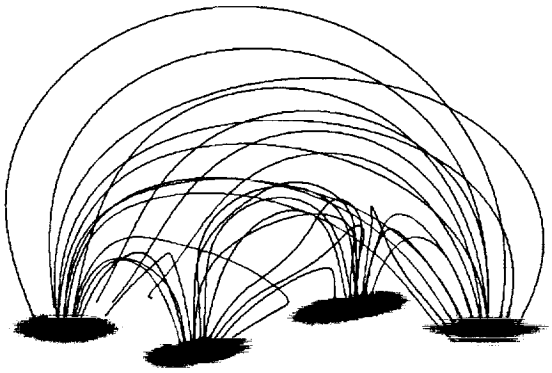

Figure 7b. Field lines at t = 350. More field lines from the lower loop have reconnected to those of the overlying loop, showing sharp turns in direction.

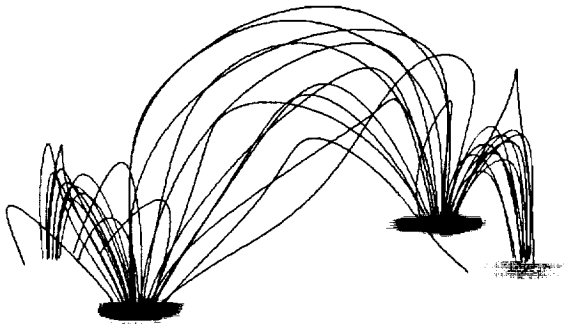

Figure 7c. Field lines at t = 425. The field lines are settling into a three loop system. The original overlying loop is more or less gone.

of the overall domain considered in the simulation. The difficult part of the port was to "seam" properly the data on the different processors and to provide the required synchronization.

As a general guideline, every variable in the old code becomes a "local" variable, in the sense that it refers only to the spatial sub-domain of each processor. The variables are still named in the same way but their value will be in general different on different processors. Naturally, a few exceptions are required and few new "global" variables, i.e., referring to the original whole domain, are introduced. These global variables are also defined on every processor, and their value is the same on every processor.

Implementing the Domain Decomposition

The MAS code is essentially a time-dependent solver for a set of fields on a spatial domain, given specified boundary and initial conditions. This is a very general structure that applies to large variety of codes. There are two independent parts of the calculation: the time evolution and the field solution at each given time. The former is implemented with a time-stepping scheme, the latter by discretizing the field equations on a spatial grid. The parallelization concerns only the field solution, at each time step. Needless to say, nothing can be done to compute the time evolution in parallel; that is an intrinsically sequential calculation.

The field equations in the MAS code are discretized with a finite-difference scheme on a structured mesh in spherical coordinates (r,θ,ϕ). A Fourier expansion is considered along the ϕ coordinate, leaving only a 2D mesh in the r–θ plane for the spatial domain decomposition. The number of sub-domains along each of the two coordinates r and θ is specified as an input; for example, by dividing the r-domain by 10 and the θ-domain by 6, the simulation will require 60 processors (assuming that there is one sub-domain per processor).

The domain decomposition must allow a certain overlapping between adjacent sub-domains to minimize the communication required between processors. The amount of overlapping is determined by the nature of the discretized differential operators that are used to represent the field equations. In the case of the MAS code, because a staggered mesh is used to discretize the equations, it turns out that a three-point overlapping along each linear dimension is required. For example, a domain decomposition into two equal sub-domains of a 40-point mesh along r will require the storage of mesh points 1–21 in the first sub-domain, and mesh points 19–40 in the second one. The three mesh points 19–21 are common to both sub-domains.

Communication Among Processors

At different times in the computation, data needs to be exchanged among processors. This communication has been implemented by using MPI, a standard "message passing" library for parallel computing. All the global operations in the code require communication between processors. Here "global" refers to the whole simulation domain, as opposed to "local," which refers to each sub-domain "owned" by each processor. Since communication time between processors is much slower than computation time on a processor, for optimum efficiency it is critical to reduce communication between processors to the minimum required.

The details of the MPI calls have been "hidden" in the code by writing the appropriate interface routines. Future improvements to the physics and/or to the numerical algorithms will be possible without requiring detailed knowledge of the inter-process communication procedures.

Status of the Parallel MAS Code

The parallelization of the MAS code has been fundamentally completed. The domain decomposition can be performed with an arbitrary number of processors along both the r and θ coordinates. Significant effort has been expended on the input/output interfaces to ensure that the input and output files are equivalent to the ones produced by the single-processor code. The parallel code has been validated by comparing with single-processor runs, and by varying the number of processors on multiple-processor runs.

Presently, the efficiency of the scaling of the code on multiple processors is being investigated. Some accessory routines still need to be parallelized and/or revised to improve the parallel efficiency. We have found that the parallel scaling is strongly dependent on the number of mesh-points per processor: the greater this number, the smaller is the inter-process communication relative to the actual computation performed by each processor. More precisely, the "surface to volume" ratio of each sub-domain is in general the most significant figure to determine the impact of the data communication among processors. Optimization efforts, especially in regards to the communication routines, are presently in progress. We are presently still testing the code and will soon use it to do "production runs" with large meshes.

Mapping *in situ* Solar Measurements Back to the Sun

During this reporting period, our investigation has focused on mapping Ulysses and WIND *in situ* measurements back to the Sun using a combination of MHD models. We used a two-dimensional (r,ϕ), single-fluid, time-independent MHD model (Pizzo 1981) to map solar wind measurements back to the Sun as far as possible (typically 30–60 solar radii). This model makes the assumption that the measurements are in fact reversible, which may limit the applicability of the results. Test simulations, however, showed that the non-reversibility is localized in the vicinity of shocks and that overall, the solution may be considered "quasi-reversible." The Pizzo model is applicable only outside of the outermost solar critical point. Furthermore, near the Sun there is considerable divergence of the flow in the meridional plane and thus modeling the flow in two dimensions becomes inappropriate. Therefore, to map the measurements from 30 solar radii to the solar surface we used our 3D solar coronal MHD model. Briefly, we traced field lines at the position of each of the mapped measurements (at 30 solar radii) back to the solar surface to deduce the source of the solar wind on the Sun.

Figure 8 displays two views of these mapped measurements: (a) on the surface of a sphere; and (b) as a synoptic chart. In both cases, the poleward-most trace corresponds to Ulysses and the equatorward-most trace corresponds to WIND. The solar surface has been color-coded according to the topology of the magnetic field lines: black indicates open field lines (i.e., field lines connected to the Sun at one end only), and gray indicates closed field lines.

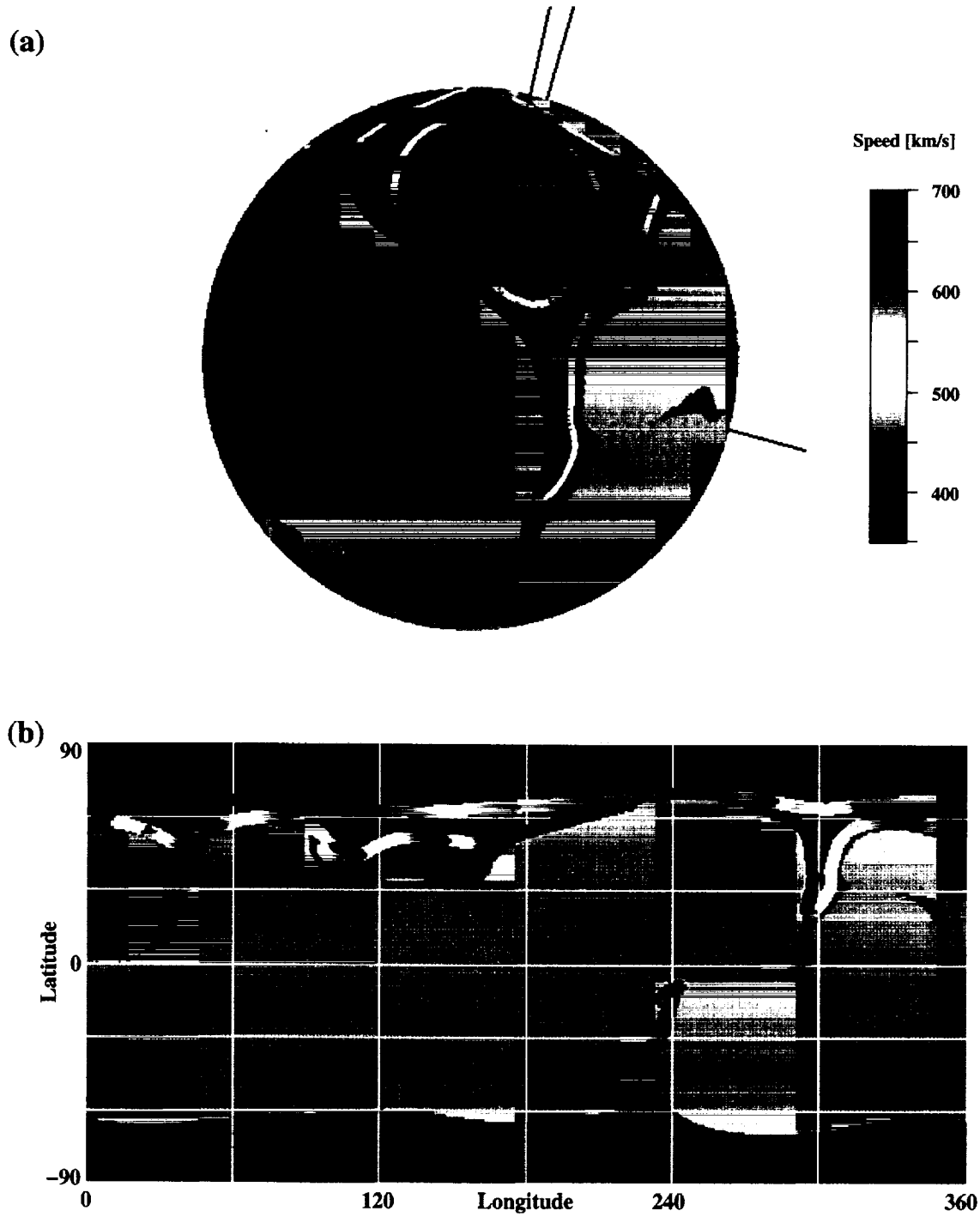

Figure 8. Ulysses and WIND trajectories are shown mapped back to the solar surface (for Carrington rotation 1913) and displayed (a) on the surface of a sphere; and (b) as a synoptic chart. The poleward–most trace corresponds to Ulysses and the equatorward–most trace corresponds to WIND. The solar surface has been colored according to the topology of the magnetic field lines; black indicates open field lines and gray indicates closed field lines. The trajectories are color–coded with their respective mapped speeds at approximately 30 solar radii; speeds 350 km/s and below are colored blue, speeds 700 km/s and above are colored red, and speeds in between are colored according to the color bar.

A striking feature of this mapping is the significant variation in solar latitude, particularly at WIND. During this interval, Ulysses was located at a heliographic latitude of 27°N and 4.25 AU, which maps back to a solar source latitude of approximately 70°N. In contrast, WIND was located in the ecliptic plane at 1 AU. These results, however, suggest that the source of the flow measured at WIND varied between 15°S and 70°N. WIND intercepted field lines from a small equatorial hole in the southern hemisphere and also intercepted flow from the equatorward extension of the northern polar coronal hole (the so-called "elephant's trunk"). The mapped trajectories have also been color-coded with the inferred mapped speed at 30 solar radii. We remark that low speed (blue) maps back to the vicinity between the open (black) and closed (gray) field line regions. Moreover, for both spacecraft, speed tends to increase with distance away from this boundary. This is consistent with the view that fast solar wind originates in coronal holes and slow solar wind is associated with the boundary between open and closed field lines (Neugebauer *et al.* 1998; Linker *et al.* 1999).

Modeling the Inner Heliosphere

We have developed a three-dimensional MHD model to investigate the large-scale structure of the heliosphere (between 30 solar radii and 5 AU). Ultimately, we plan to drive this heliospheric model self-consistently using output from the coronal model. Currently, however, the simplified prescription of the polytropic energy equation employed in the algorithm does not yield sufficiently high plasma speeds necessary to drive a realistic heliospheric solution. Thus, as an interim solution, we utilize the magnetic field topology from the coronal solution to generate flow fields at the inner boundary of the heliospheric model. The coronal model itself is driven by the observed line-of-sight component of the photospheric magnetic field, and so the models can be, and are, run for specific time periods of interest. The results are compared with both remote solar observations as well as *in situ* observations and can be used as a basis for interpreting observations from a variety of disparate data sets. Figure 9 summarizes the heliospheric solution for the Whole Sun Month (a solar rotation involving parts of Carrington rotations 1912 and 1913). The heliospheric current sheet (inferred from the iso-surface $B_r = 0$) is displayed out to 5 AU. The central sphere marks the inner boundary at 30 solar radii. A meridional slice of the radial velocity is shown at an arbitrary longitude. Blue corresponds to slowest speeds (350 km/s) and red corresponds to fastest speeds (750 km/s). Superimposed are a selection of interplanetary magnetic field lines, all emanating from the same heliographic longitude, but at different latitudes. Finally, the trajectories of the WIND and Ulysses spacecraft are displayed. A comparison of Ulysses and WIND measurements with the simulation indicates that the model has reproduced the essential large-scale features of the heliosphere during this time period. Figure 10 shows equatorial and meridional cuts of the solar wind velocity in the inner heliosphere during this time.

Presentation at the Ulysses Science Working Team Meeting, San Diego

In October 1999, Pete Riley presented a status report on our modeling efforts of the inner heliosphere, including the comparison with Ulysses *in situ* measurements.

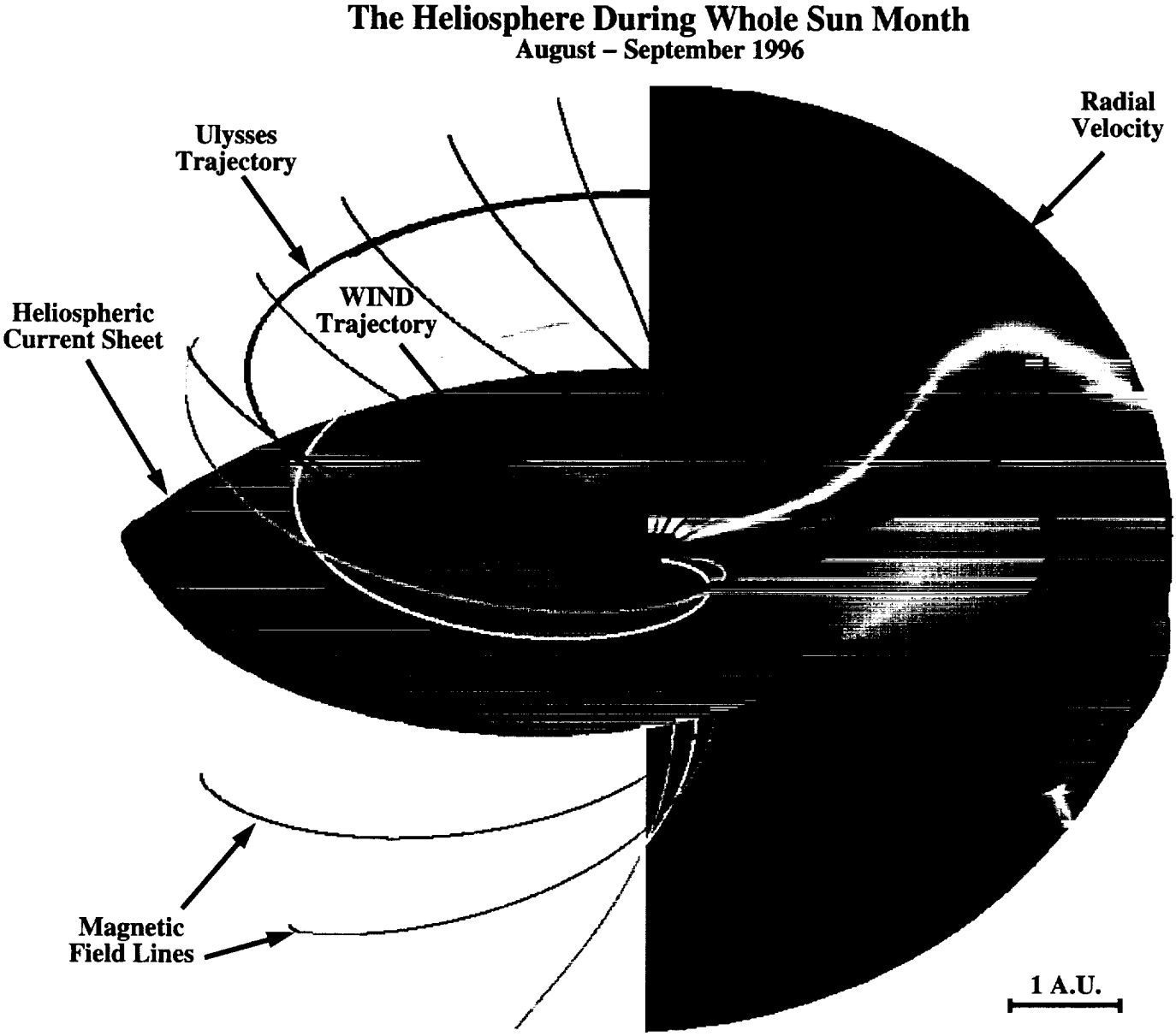

Figure 9. Structure of the solar wind speed, magnetic field lines, and heliospheric current sheet in the inner heliosphere during the Whole Sun Month time period.

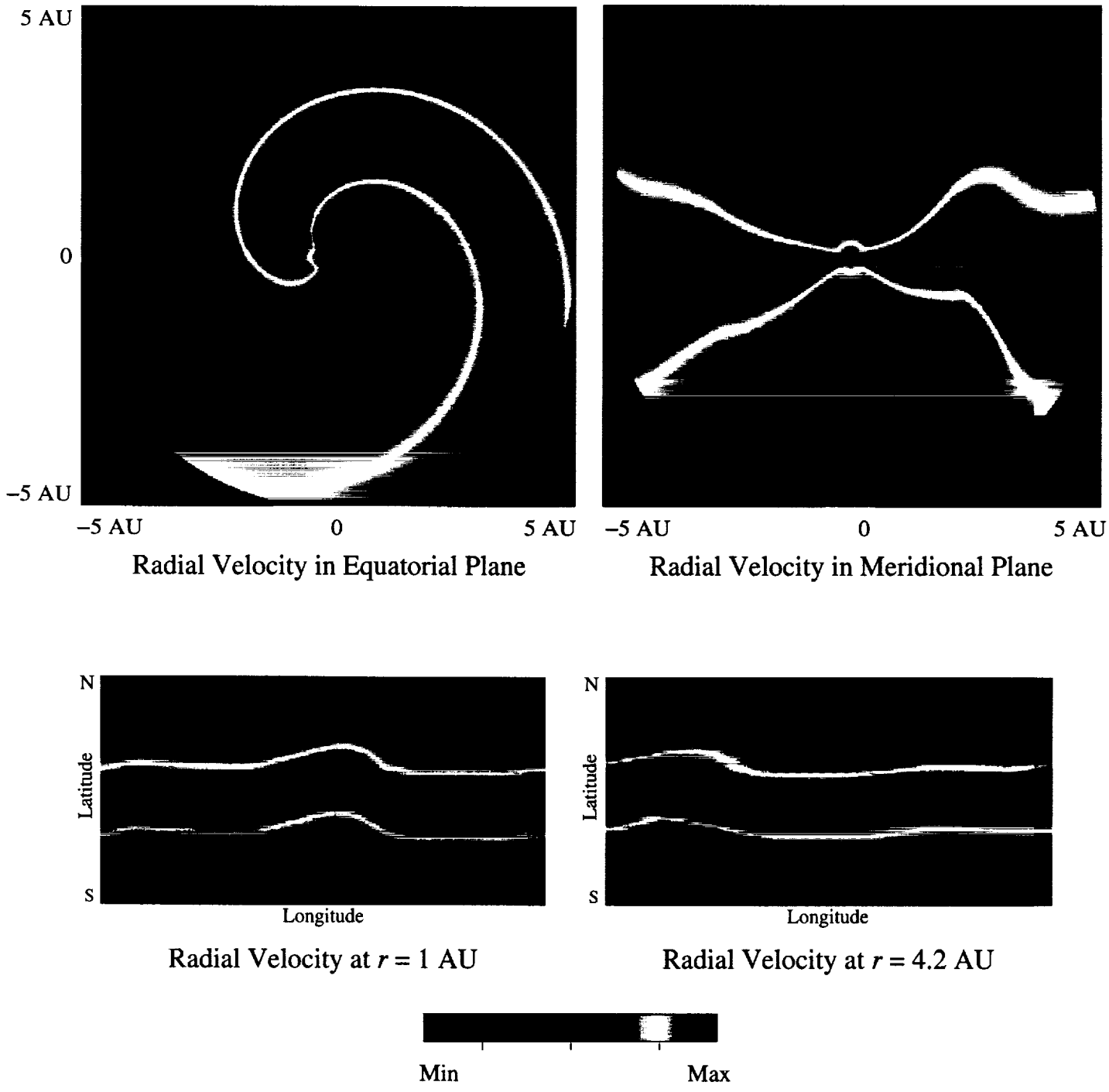

Figure 10. Structure of the solar wind speed in the inner heliosphere during the Whole Sun Month time period. Note the flow in the equatorial plane illustrates the characteristic "Parker spiral."

Presentation at the Western Pacific Geophysics Meeting, Taiwan

In July 1998, Jon Linker presented an invited talk, "Magnetohydrodynamic Modeling of the Solar Corona For Space-Weather Applications," at the Western Pacific Geophysics Meeting held in Taipei, Taiwan.

Presentations at the Spring AGU Meeting and the SHINE 99 Workshop

We presented the poster paper "Probing the Relationship Between the Solar Corona and Solar Wind Structure using MHD Models," by P. Riley, Z. Mikić, J. A. Linker, J. T. Gosling, and V. J. Pizzo, at the Spring American Geophysical Union meeting, held in Boston, MA, May 31–June 4, 1999, and at the SHINE 99 Summer Workshop, held in Boulder, Colorado, June 14–17, 1999. We also presented the poster paper "Initiation of Coronal Mass Ejections by Changes in Photospheric Flux," by Z Mikić, J. A. Linker, T. Amari, and J.-F. Luciani, and the poster paper "Relationship Between Electron Density and Temperature Within CMEs," by P. Riley. J. A. Linker gave an invited review talk on "Existing Solar Wind Propagation Models" at the SHINE 99 meeting.

2. REFERENCES

Mikić, Z., Linker, J. A., Schnack, D. D., Lionello, R., & Tarditi, A. 1999, *Phys. Plasmas*, **6**, 2217.

Mikić, Z., Linker, J. A., Riley, P., & Lionello, R. 1999, "Predicting the Structure of the Solar Corona During the 11 August 1999 Total Solar Eclipse," in *The Last Total Solar Eclipse of the Millennium* (W. Livingston and A. Ö zgüç, eds.), Astronomical Society of the Pacific Conference Series, to appear.

Amari, T., Luciani, J.-F., Mikić, Z., & Linker, J. A. 1999, *Ap. J.*, **518**, L57.

Amari, T., Boulmezaoud, T. Z., & Mikić, Z. 1999, *Astron. Astrophys.*, **350**, 1051.

Van Hoven, G., Mok, Y., & Mikić, Z. 1995, *Ap. J.*, **440**, L105.

Mok, Y., Van Hoven, G., & Mikić, Z. 1997, *Ap. J.*, **490**, L107.

Pizzo, V. J. 1981, *J. Geophys. Res.*, **86**, 6685.

Neugebauer, M., Forsyth, R. J., Galvin, A. B., Harvey, K. L., Hoeksema, J. T., Lazarus, A. J., Lepping, R. P., Linker, J. A., Mikić, Z., Steinberg, J. T., von Steiger, R., Wang, Y.-M., & Wimmer-Schweingruber, R. 1998, *J. Geophys. Res.*, **103**, 14587.

3. PUBLICATIONS SUPPORTED FULLY OR IN PART BY SPACE PHYSICS THEORY CONTRACT NAS5-96081

1. J. A. Linker and Z. Mikić, "Disruption of a Helmet Streamer by Photospheric Shear," *Astrophys. J.*, **438**, L45 (1995).
2. Y. Mok and G. Van Hoven, "The Solar-Surface Boundary Conditions of Coronal Magnetic Loops," *Solar Phys.*, **161** 67 (1995).
3. G. Van Hoven, D. L. Hendrix, and D. D. Schnack. "The Diagnosis of General Magnetic Reconnection," *J. Geophys. Res.*, **100**, 19819 (1995).
4. G. Van Hoven, Y. Mok, and Z. Mikić, "Coronal Loop Formation Resulting from Photospheric Convection," *Astrophys. J.*, **440**, L105 (1995).
5. G. Van Hoven, J. A. Linker, and Z. Mikić, "The Evolution, Structure, and Dynamics of the Magnetized Solar Corona," Gather/Scatter (San Diego Supercomputer Center Newsletter), Vol. **11**, No. 3, p. 6, July–September (1995).
6. D. L. Hendrix, "A Study of the Formation and Dissipation of Current Filaments as a Coronal Heating Mechanism," Ph. D. Thesis, University of California, Irvine (1996).
7. D. L. Hendrix and G. Van Hoven, "Magnetohydrodynamic Turbulence and Implications for Solar Coronal Heating," *Astrophys. J.*, **467**, 887 (1996).
8. D. L. Hendrix, G. Van Hoven, Z. Mikić, and D. D. Schnack, "The Viability of Ohmic Dissipation as a Coronal Heating Source," *Astrophys. J.*, **470**, 1192 (1996).
9. J. A. Linker, Z. Mikić, and D. D. Schnack, "Global Coronal Modeling and Space Weather Prediction," in *Solar Drivers of Interplanetary and Terrestrial Disturbances* (K. S. Balasubramaniam, S. L. Keil, and R. N. Smartt, eds.), Astronomical Society of the Pacific Conference Series, Vol. **95**, p. 208 (1996).
10. Z. Mikić and J. A. Linker, "The Large-Scale Structure of the Solar Corona and Inner Heliosphere," in *Solar Wind Eight: Proc. of the Eight Intl. Solar Wind Conf.* (D. Winterhalter, J. T. Gosling, S. R. Habbal, W. S. Kurth, and M. Neugebauer, eds.), AIP Conf. Proceedings, **382**, AIP Press, Woodbury, N. Y., p. 104 (1996).
11. Z. Mikić, J. A. Linker, and D. D. Schnack, "Modeling of Active-Region Magnetic Fields," in *Solar Drivers of Interplanetary and Terrestrial Disturbances* (K. S. Balasubramaniam, S. L. Keil, and R. N. Smartt, eds.), Astronomical Society of the Pacific Conference Series Vol. **95**, p. 108 (1996).
12. S. P. Ruden, A. V. Ṙ. Schiano, and G. Van Hoven, "A Dynamic Model of the Three-Fluid Solar Wind: Equilibrium Structures and Fluxes," in *Solar Wind Eight: Proc. of the Eight Intl. Solar Wind Conf.* (D. Winterhalter, J. T. Gosling, S. R. Habbal, W. S. Kurth, and M. Neugebauer, eds.), AIP Conf. Proceedings **382**, AIP Press, Woodbury, N. Y., p. 137 (1996).

13. G. Van Hoven, Y. Mok, and D. L. Hendrix, "Surface Driven Evolution and Activity of Atmospheric Magnetic Structures," in *Magnetodynamic Phenomena in the Solar Atmosphere: Proc. IAU Colloquium 153* (Y. Uchida, T. Kosugi, and H. S. Hudson, eds.), Proc. IAU Colloquium 153, Kluwer, Dordrecht, p. 51 (1996).

14. T. Amari, J. J. Aly, J. F. Luciani, T. Boulmezaoud, and Z. Mikić, "Reconstructing The Solar Coronal Magnetic Field as a Force-Free Magnetic Field," *Solar Phys.*, **174**, 129 (1997).

15. T. Amari, J. F. Luciani, J. J. Aly, and Z. Mikić, "Opening Solar Magnetic Fields: Some Analytical and Numerical MHD Aspects," in *Coronal Mass Ejections* (N. Crooker, J. Joselyn, and J. Feynman, eds.), Geophysical Monograph **99**, American Geophysical Union, p. 101 (1997).

16. G. Einaudi, R, Lionello, and M. Velli, "Magnetic Reconnection in Solar Coronal Loops," *Adv. Space. Res.*, **19**, 1875 (1997).

17. D. L. Hendrix, and G. Van Hoven, "Dynamical Magnetic Reconnection in Parker's Coronal Heating Model," *Adv. Space Res.*, **19**, 1865 (1997).

18. L. Jiao, A. N. McClymont, and Z. Mikić, "Reconstruction of the Three-Dimensional Coronal Magnetic Field," *Solar Phys.*, **174**, 311 (1997).

19. J. A. Linker and Z. Mikić, "Extending Coronal Models to Earth Orbit," in *Coronal Mass Ejections* (N. Crooker, J. Joselyn, and J. Feynman, eds.), Geophysical Monograph **99**, American Geophysical Union, p. 269 (1997).

20. R. Lionello, "Three Dimensional Imaging for Magnetohydrodynamic Computations," *WSCG'97 Proceedings* (1997).

21. A. N. McClymont, L. Jiao, and Z. Mikić, "Problems and Progress in Computing Three-Dimensional Coronal Active Region Magnetic Fields from Boundary Data," *Solar Phys.*, **174**, 191 (1997).

22. Z. Mikić and J. A. Linker, "The Initiation of Coronal Mass Ejections by Magnetic Shear," in *Coronal Mass Ejections* (N. Crooker, J. Joselyn, and J. Feynman, eds.), Geophysical Monograph **99**, American Geophysical Union, p. 57 (1997).

23. Y. Mok, G. Van Hoven, and Z. Mikić, "The Emergence of Current-Carrying Magnetic Loops into the Solar Corona," *Astrophys. J.*, **490**, L107 (1997).

24. A. Ruzmaikin, J. D. Anderson, S. Asmar, M. Bird, A. Cacciani, W. Coles, J. Feynman, J. Harvey, K. Harvey, J. Hollweg, J. Linker, Z. Mikić, M. Patzold, and E. J. Smith, "A Spacecraft Going Behind the Sun will Support SOHO," in *The Corona and Solar Wind Near Minimum Activity* (Proceedings of the Fifth SOHO Workshop), ESA SP-404, 653 (1997).

25. M. Velli, R. Lionello, and G. Einaudi, "Kink Modes and Current Sheets in Coronal Loops," *Solar Phys.*, **172**, 257 (1997).

26. N. U. Crooker, A. H. McAllister, R. J. Fitzenreiter, J. A. Linker, D. E. Larson, R. P. Lepping, A. Szabo, J. T. Steinberg, A. J. Lazarus, Z. Mikić, and R. P. Lin, "Sector

Boundary Transformation by an Open Magnetic Cloud," *J. Geophys. Res.*, **103**, 26859 (1998).

27. J. Lee, A. N. McClymont, Z. Mikić, S. M. White, and M. R. Kundu, "Coronal Currents, Magnetic Fields, and Heating in a Solar Active Region," *Astrophys. J.*, **501**, 853 (1998).
28. J. Lee, S. M. White, M. R. Kundu, Z. Mikić, and A. N. McClymont, "Microwave Mode Coupling above Active Regions as a Coronal Density Diagnostic," *Solar Phys.*, **180**, 193 (1998).
29. R. Lionello, Z. Mikić, and D. D. Schnack, "Magnetohydrodynamics of Solar Coronal Plasmas in Cylindrical Geometry," *J. Comput. Phys.*, **140**, 172 (1998).
30. R. Lionello, M. Velli, G. Einaudi, and Z. Mikić, "Nonlinear Magnetohydrodynamic Evolution of Line-Tied Coronal Loops," *Astrophys. J.*, **494**, 840 (1998).
31. M. Neugebauer, R. J. Forsyth, A. B. Galvin, K. L. Harvey, J. T. Hoeksema, A. J. Lazarus, R. P. Lepping, J. A. Linker, Z. Mikić, J. T. Steinberg, R. von Steiger, Y.-M. Wang, and R. Wimmer-Schweingruber, "Spatial Structure of the Solar Wind and Comparisons with Solar Data and Models," *J. Geophys. Res.*, **103**, 14587 (1998).
32. D. D. Schnack, I. Lottati, Z. Mikić, and P. Satyanarayana, "A Finite-Volume Algorithm for Three-Dimensional Magnetohydrodynamics on an Unstructured, Adaptive Grid in Axially Symmetric Geometry," *J. Comput. Phys.*, **140**, 71 (1998).
33. R. Lionello, D. D. Schnack, G. Einaudi, and M. Velli, "Current sheet formation due to nonlinear kink modes in periodic and line-tied configurations," *Phys. Plasmas*, **5**, 3722 (1998).
34. P. Riley, "CME Dynamics in a Structured Solar Wind," in *Solar Wind Nine: Proc. of the Ninth Intl. Solar Wind Conf.* (S. R. Habbal, R. Esser, J. V. Hollweg, and P. A. Isenberg,, eds.), AIP Conf. Proceedings, **471**, AIP Press, Woodbury, N. Y., p. 131 (1999).
35. A. R. Breen, Z. Mikić, J. A. Linker, A. J. Lazarus, B. J. Thompson, D. A. Biesecker, P. J. Moran, C. A. Varley, P. J. S. Williams, and A. Lecinski, "Interplanetary Scintillation Measurements of the Solar Wind During Whole Sun Month: Comparisons with Coronal and *In-Situ* Observations," *J. Geophys. Res.*, **104**, 9847 (1999).
36. S. E. Gibson, D. A. Biesecker, M. Guhathakurta, J. T. Hoeksema, A. J. Lazarus, J. A. Linker, Z. Mikić, Y. Pisanko, J. T. Steinberg, B. J. Thompson, and X. P. Zhao, "The Three-Dimensional Coronal Magnetic Field During Whole Sun Month," *Astrophys. J.*, **520**, 871 (1999).
37. J. Lee, S. M. White, M. R. Kundu, Z. Mikić, and A. N. McClymont, "A Test for Coronal Magnetic Field Extrapolations," *Astrophys. J.*, **510**, 413 (1999).
38. J. A. Linker, Z. Mikić, D. A. Biesecker, R. J. Forsyth, S. E. Gibson, A. J. Lazarus, A. Lecinski, P. Riley, A. Szabo, and B. J. Thompson, "Magnetohydrodynamic Modeling of the Solar Corona During Whole Sun Month," *J. Geophys. Res.*, **104**, 9809 (1999).

39. A. Posner, V. Bothmer, B. J. Thompson, H. Kunow, B. Heber, R. Müller-Mellin, A. J. Lazarus, A. Szabo, Z. Mikić, and J. A. Linker, "In-Ecliptic CIR-Associated Energetic Particle Events and Polar Coronal Hole Structures: SOHO/COSTEP Observations for the Whole Sun Month Campaign," *J. Geophys. Res.*, **104**, 9881 (1999).

40. R. Lionello, Z. Mikić, and J. A. Linker, "Stability of Algorithms for Waves with Large Flows," *J. Comput. Phys.*, **152**, 346 (1999).

41. Z. Mikić, J. A. Linker, D. D. Schnack, R. Lionello, and A. Tarditi, "Magnetohydrodynamic Modeling of the Global Solar Corona," *Phys. Plasmas*, **6**, 2217 (1999).

42. T. Amari, J. F. Luciani, Z. Mikić, and J. A. Linker, "Three-Dimensional Solutions of Magnetohydrodynamic Equations for Prominence Magnetic Support: Twisted Magnetic Flux Rope," *Astrophys. J.*, **518**, L57 (1999).

43. T. Amari, T. Z. Boulmezaoud, and Z. Mikić, "An Iterative Method for the Reconstruction of the Solar Coronal Magnetic Field: I. Method for Regular Solutions," *Astron. Astrophys.*, **350**, 1051 (1999).

44. T. Amari, J. F. Luciani, Z. Mikić, "On the Role of Magnetic Flux Ropes for Helicity Injection and Ejection in the Solar Corona," in *Third Advances in Solar Physics Euroconference: Magnetic Fields and Oscillations* (B. Schmieder, A. Hofmann, and J. Staude, eds.), Astronomical Society of the Pacific Conference Series, Vol. **184**, p. 70 (1999).

45. R. Lionello, J. A. Linker, and Z. Mikić, "Magnetohydrodynamics of the Solar Corona and the Transition Region," in *Proc. of the 9th European Meeting on Solar Physics: Magnetic Fields and Solar Processes*, Florence, Italy, Sept. 12–18, 1999, ESA SP-448, p. 1181 (1999).

46. T. Amari, J. F. Luciani, and Z. Mikić, "Magnetohydrodynamic Models of Solar Coronal Magnetic Fields," *Plasma Phys. Control. Fusion*, **41**, A779 (1999).

47. A. Balogh, V. Bothmer, N. U. Crooker, R. J. Forsyth, G. Gloeckler, A. Hewish, M. Hilchenbach, R. Kallenbach, B. Klecker, J. A. Linker, E. Lucek, G. Mann, E. Marsch, A. Posner, I. G. Richardson, J. M. Schmidt, M. Scholer, Y.-M. Wang, R. F. Wimmer-Schweingruber, M. R. Aellig, P. Bochsler, S. Hefti, and Z. Mikić, "The Solar Origin of Corotating Interaction Regions and Their Formation in the Inner Heliosphere," *Space Science Reviews*, **89**, 141 (1999).

48. S. Vainshtein, Z. Mikić, R. Rosner, and J. A. Linker, "Evidence for Topological Nonequilibrium in Magnetic Configurations," *Phys. Rev. E*, submitted (1999).

49. Z. Mikić, J. A. Linker, P. Riley, and R. Lionello, "Predicting the Structure of the Solar Corona During the 11 August 1999 Total Solar Eclipse," in *The Last Total Solar Eclipse of the Millennium* (W. Livingston and A. Ö zgüç, eds.), Astronomical Society of the Pacific Conference Series, to appear (1999).

4. APPENDIX

SELECTED REPRINTS

JOURNAL OF GEOPHYSICAL RESEARCH, VOL. 104, NO. A5, PAGES 9809–9830, MAY 1, 1999

Magnetohydrodynamic modeling of the solar corona during Whole Sun Month

J. A Linker,[1] Z. Mikić,[1] D. A. Biesecker,[2,3] R. J. Forsyth,[4] S. E. Gibson,[5,6] A. J. Lazarus,[7] A. Lecinski,[8] P. Riley,[9,10] A. Szabo,[11] and B. J. Thompson[11]

Abstract. The Whole Sun Month campaign (August 10 to September 8, 1996) brought together a wide range of space-based and ground-based observations of the Sun and the interplanetary medium during solar minimum. The wealth of data collected provides a unique opportunity for testing coronal models. We develop a three-dimensional magnetohydrodynamic (MHD) model of the solar corona (from 1 to 30 solar radii) applicable to the WSM time period, using measurements of the photospheric magnetic field as boundary conditions for the calculation. We compare results from the computation with daily and synoptic white-light and emission images obtained from ground-based observations and the SOHO spacecraft and with solar wind measurements from the Ulysses and WIND spacecraft. The results from the MHD computation show good overall agreement with coronal and interplanetary structures, including the position and shape of the streamer belt, coronal hole boundaries, and the heliospheric current sheet. From the model, we can infer the source locations of solar wind properties measured in interplanetary space. We find that the slow solar wind typically maps back to near the coronal hole boundary, while the fast solar wind maps to regions deeper within the coronal holes. Quantitative disagreements between the MHD model and observations for individual features observed during Whole Sun Month give insights into possible improvements to the model.

1. Introduction

The solar magnetic field plays a central role in coronal and interplanetary physics, defining the structure of the solar corona and inner heliosphere. Just as the number and complexity of sunspot groups vary with the (approximate) 11-year solar cycle, the complexity of the Sun's global magnetic field also varies, and this level of complexity is reflected in the structure of the solar corona. During solar minimum, solar activity is less frequent and the large-scale corona exhibits its simplest behavior. Long-lived helmet streamers and coronal holes may persist over several solar rotations. Solar minimum conditions provide us with an opportunity to separate the basic underlying structure of the corona from the solar active phenomena that disrupt it (such as coronal mass ejections), to understand how the solar magnetic field controls and influences the structures we see in the corona in various wavelengths, and to determine the solar source of phenomena measured in interplanetary space.

With these goals in mind, a coordinated observing campaign of the solar minimum Sun was carried out for 1 solar rotation. The campaign, known as Whole Sun Month (WSM), occurred from August 10 to September 8, 1996, utilizing Solar and Heliospheric Observatory (SOHO), WIND, Ulysses, and ground-based data. The wide range of different solar observations collected allows us to obtain a more comprehensive understanding of the solar corona and its influence on the heliosphere during solar minimum.

A fundamental difficulty in understanding coronal structure is that while the magnetic field is recognized

[1]Science Applications International Corporation, San Diego, California.
[2]University of Birmingham, Birmingham, England.
[3]Now at SM&A Corporation, Greenbelt, Maryland.
[4]Blackett Laboratory, Imperial College, London.
[5]Catholic University of America, Washington, D.C.
[6]Now at Department of Applied Mathematics and Theoretical Physics, University of Cambridge, Cambridge, England.
[7]Center for Space Research, Massachusetts Institute of Technology, Cambridge.
[8]High Altitude Observatory, National Center for Atmospheric Research, Boulder, Colorado.
[9]SciberNet, Inc., San Diego, California.
[10]Now at Science Applications International Corporation, San Diego, California.
[11]NASA Goddard Space Flight Center, Greenbelt, Maryland.

Paper number 1998JA900159.
0148-0227/99/1998JA900159$09.00

to play a crucial role, there are few measurements of the coronal magnetic field. However, the line-of-sight component of the magnetic field has been measured in the photosphere for many years (for example, at the Wilcox Solar Observatory and at the National Solar Observatory at Kitt Peak). A key to understanding the structure of the corona and solar wind is to accurately extrapolate the measured photospheric field outward. The simplest and most widely used techniques for accomplishing this task are based on potential field models (e.g., the potential field source-surface model [*Schatten et al.*, 1969; *Altschuler and Newkirk*, 1969] and the potential field current sheet model [*Schatten*, 1971]). While these models do not directly describe the coronal plasma, they can address many aspects of coronal and interplanetary data [e.g., *Hoeksema et al.*, 1983; *Wang and Sheeley*, 1988, 1992, 1995], and the models are still being refined and improved [e.g., *Zhao and Hoeksema*, 1995]. *Zhao et al.* [this issue] discuss source-surface modeling for the WSM time period.

Ideally, a model should not only extrapolate the magnetic field, but also should self-consistently describe the plasma as well. Magnetostatic models [*Bogdan and Low*, 1986; *Bagenal and Gibson*, 1991; *Gibson and Bagenal*, 1995; *Gibson et al.*, 1996] include the plasma force balance in the lower corona (neglecting flow terms) and have been used to quantitatively model specific time periods (with assumptions of azimuthal symmetry). *Gibson et al.* [1997] and *Gibson et al.* [The three-dimensional coronal magnetic field during Whole Sun Month, submitted to *Astrophysical Journal*, 1998] describe magnetostatic modeling for WSM.

Full magnetohydrodynamic (MHD) computations can, in principle, describe both the lower solar corona and solar wind. One advantage to this approach is that no assumptions are made about the nature of coronal currents or other properties of the solution; an initial value problem is specified and the solution is computed. While MHD computations have been performed since the 1970s [e.g., *Endler*, 1971; *Pneuman and Kopp*, 1971], they have usually addressed idealized properties of the corona and not specific observations. Recently, MHD computations that incorporate observed photospheric fields into the boundary conditions [*Mikić and Linker*, 1996; *Usmanov*, 1996] have been used to model specific time periods and have been compared with eclipse and interplanetary observations [*Mikić and Linker*, 1996; *Linker et al.*, 1996; *Linker and Mikić*, 1997]. In principle, MHD modeling is a very powerful approach for studying the solar corona and solar wind when a coordinated set of observations is available, as a comprehensive model is then required to synthesize the different measurements into a coherent picture. However, the use of this approach to address specific observations is relatively new and is still being explored. The WSM campaign provides an extensive number of observations with which to compare, from which we can determine the strengths and weaknesses of the model.

In this paper, we present MHD solutions of the solar corona out to $30R_s$ (solar radii) for the WSM time period and we compare the results with available coronal observations. Section 2 briefly describes the methodology. In section 3, we show some of the basic properties of the MHD solution we obtained, and we compare the global structure predicted by the model with white-light and emission line images, especially the structure of the streamer belt and the location of coronal hole boundaries. We focus on a particular feature of interest, the extended coronal hole known as the "elephant's trunk" (named because of its elongated shape) that was observed in late August 1996. In principle, MHD solutions can be extended beyond $30R_s$ far into interplanetary space (for example, MHD solutions of the solar wind from $30R_s$ out to 1 AU have been performed [*Pizzo*, 1991]), but with the present model the extra computational expense is probably not warranted, given the simplicity of the energy equation (as discussed in sections 2 and 3, more sophisticated thermodynamic processes must be included to accurately describe fast and slow solar wind streams). Therefore, to compare the model with available solar wind data, we take the approach of mapping solar wind features back into the computational domain, as has been done previously with potential field models (see *Neugebauer et al.* [1998] for a comparison of several models). Using this technique, we describe predictions by the model for the solar source of solar wind features observed at 1 AU by WIND and at 4 AU by Ulysses (1 astronomical unit (AU) = 1.49×10^8 km = 214 solar radii). Section 4 discusses our results in the context of present and future coronal modeling.

2. Methodology

To compute MHD solutions for the large-scale corona, we solve the following form of the equations in spherical coordinates:

$$\nabla \times \mathbf{B} = \frac{4\pi}{c}\mathbf{J} \tag{1}$$

$$\frac{1}{c}\frac{\partial \mathbf{B}}{\partial t} = -\nabla \times \mathbf{E} \tag{2}$$

$$\mathbf{E} + \frac{\mathbf{v} \times \mathbf{B}}{c} = \eta \mathbf{J} \tag{3}$$

$$\frac{\partial \rho}{\partial t} + \nabla \cdot (\rho \mathbf{v}) = 0 \tag{4}$$

$$\rho\left(\frac{\partial \mathbf{v}}{\partial t} + \mathbf{v} \cdot \nabla \mathbf{v}\right) = \frac{1}{c}\mathbf{J} \times \mathbf{B} - \nabla p + \rho \mathbf{g} + \nabla \cdot (\nu \rho \nabla \mathbf{v}) \tag{5}$$

$$\frac{\partial p}{\partial t} + \nabla \cdot (p\mathbf{v}) = (\gamma - 1)(-p \nabla \cdot \mathbf{v} + S) \tag{6}$$

where $\mathbf{B}$ is the magnetic field intensity; $\mathbf{J}$ is the electric current density; $\mathbf{E}$ is the electric field; and $\mathbf{v}$, ρ, and p are the plasma velocity, mass density, and pressure, respectively. The gravitational acceleration is $\mathbf{g}$, γ is the

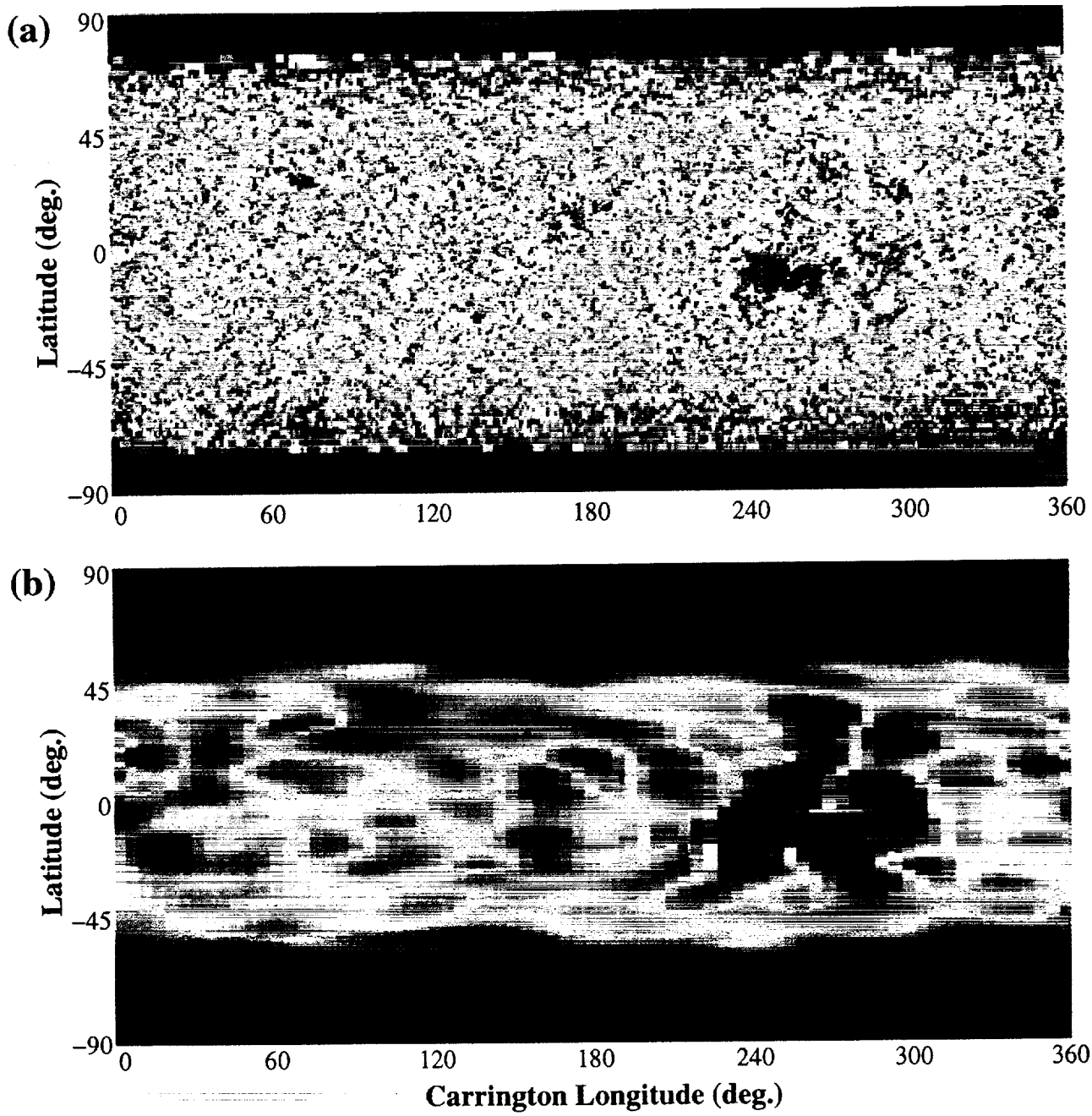

Plate 1. (a) Composite synoptic radial magnetic field map developed from synoptic National Solar Observatory at Kitt Peak (NSO/Kitt Peak) maps for Carrington rotations 1912 and 1913 (see text). Blue (red) values indicate field directed into (out of) the Sun. (b) The radial magnetic field map used in the MHD calculation. This map was developed from the map in Plate 1a by interpolation and smoothing. The scaling in the two images is not identical but was chosen to emphasize the small-scale fields.

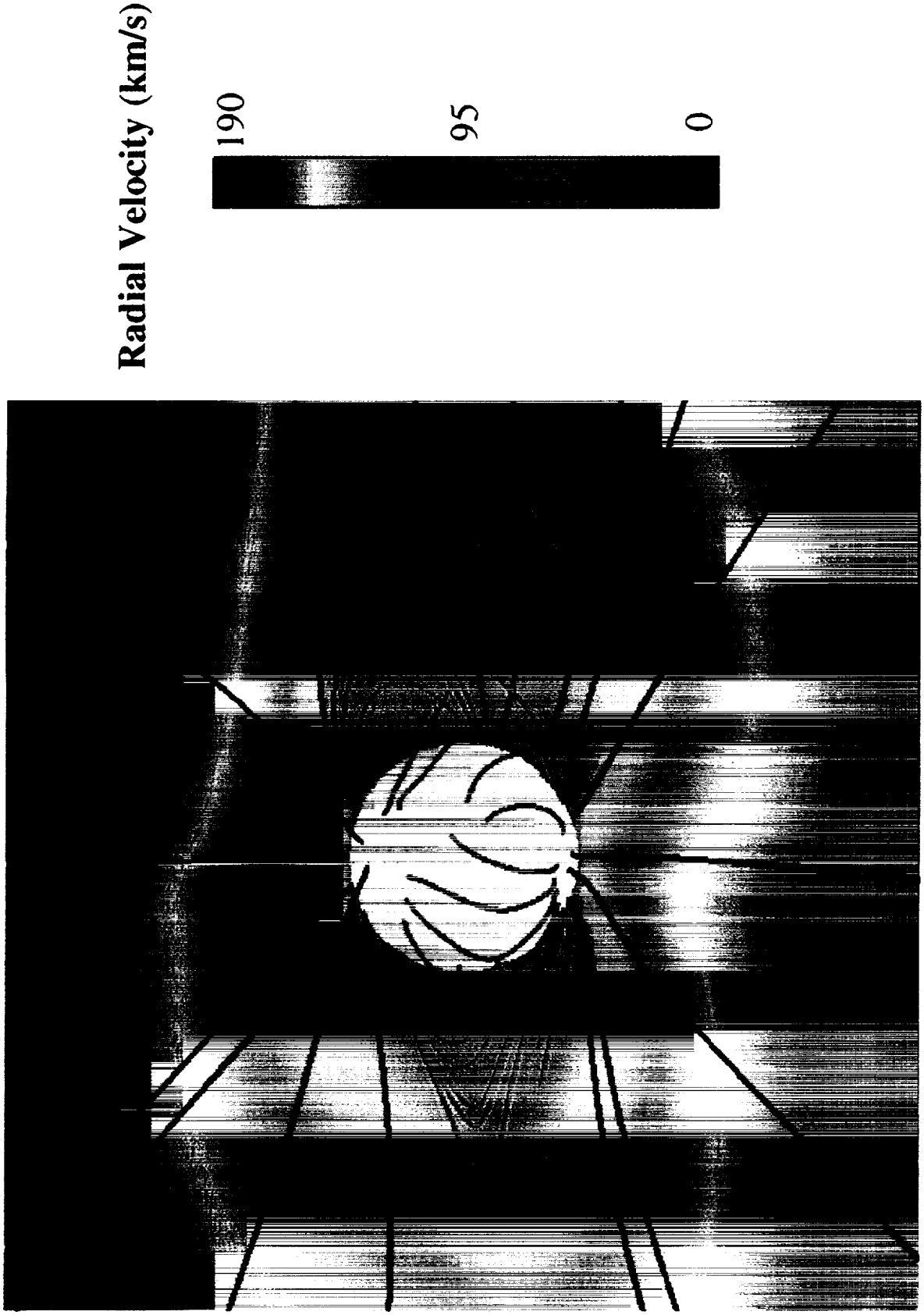

Plate 2. Magnetic field lines from the MHD calculation superimposed on the radial velocity, corresponding to a central meridian longitude of 191° (September 3, 1996). The radial velocity has been color contoured in the plane perpendicular to the line of sight. Closed magnetic fields are shown in red, and open field lines are shown in black. The solar surface is shown in yellow. Red field lines that appear to be open actually close behind the plane depicting the velocity.

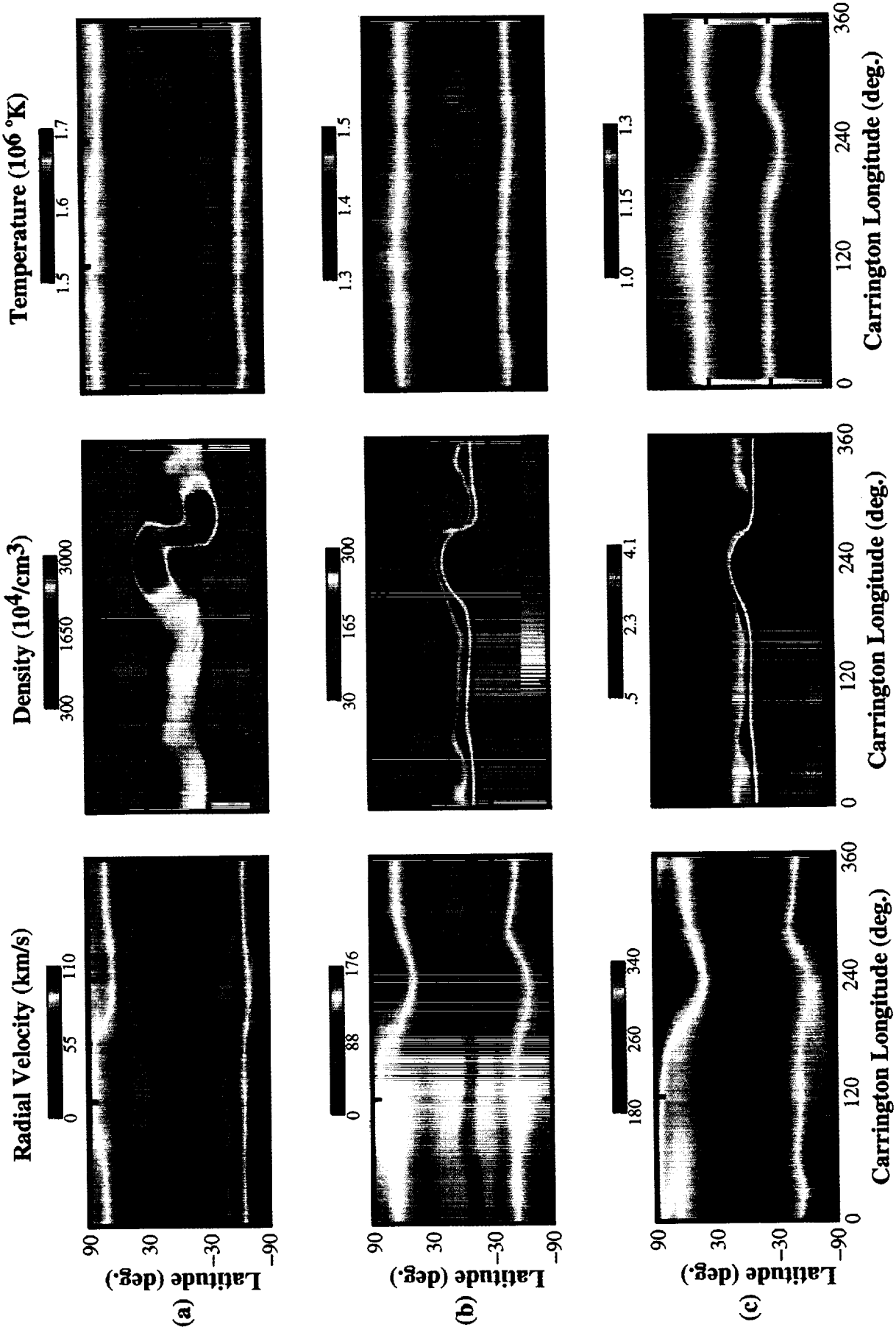

Plate 3. The radial velocity, number density, and temperature versus latitude and longitude from the MHD calculation for 3 different heights in the corona, (a) $r = 1.5R_s$, (b) $r = 2.5R_s$, and (c) $r = 10R_s$.

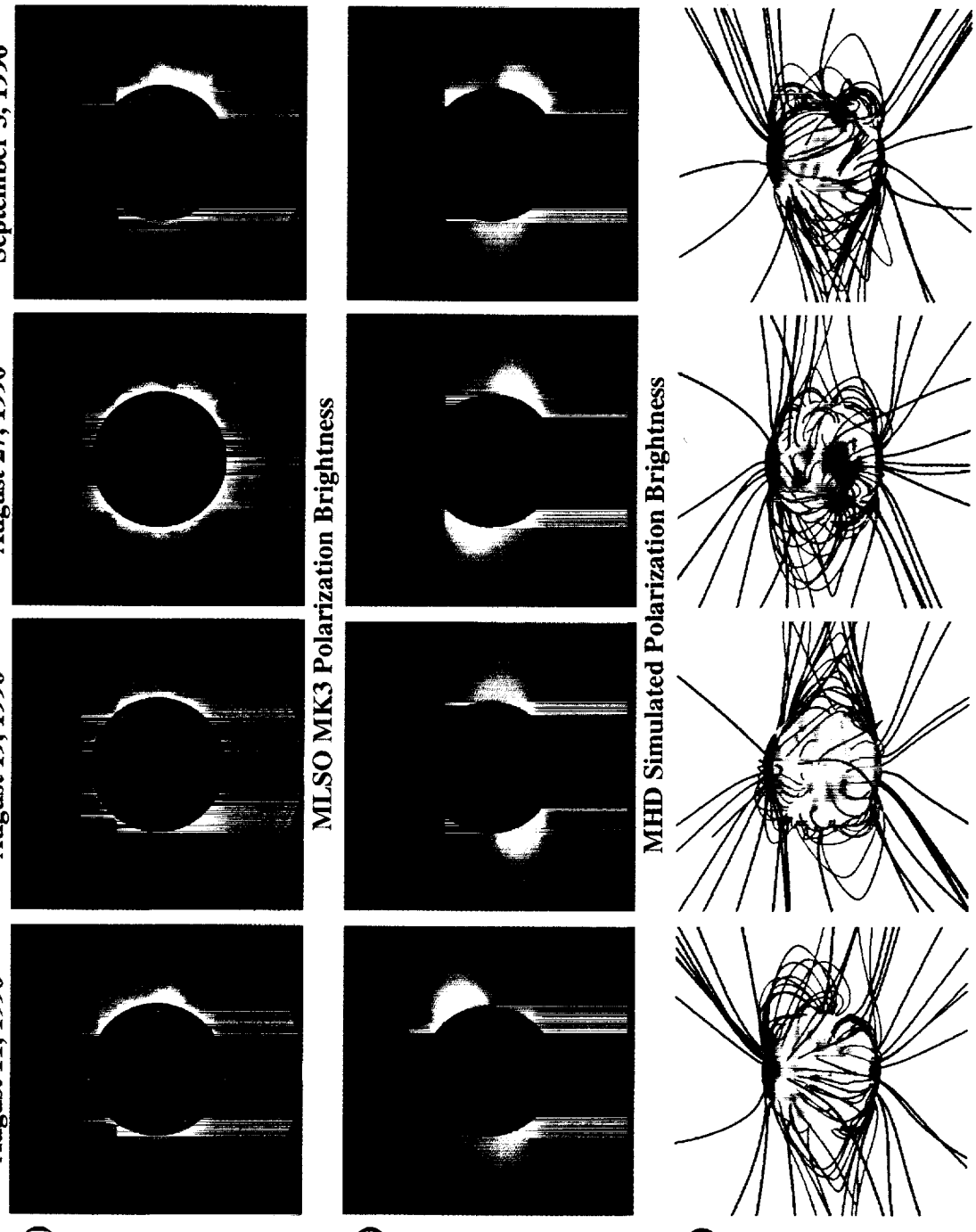

Plate 4. Comparison of the MHD model with daily white-light coronal images. (a) Images of the polarization brightness *pB* from the Mauna Loa Solar Observatory's (MLSO) Mark III K-coronameter, for 4 days during the Whole Sun Month time period. (b) the *pB* predicted by the MHD computation for the same days shown in Plate 4a. (c) Magnetic field lines from the MHD computation for the same days shown in Plates 4a and 4b. B_r is contoured on the surface of the Sun, with blue (red) values indicating fields directed into (out of) the Sun. Green and blue field lines are closed, black field lines are open.

ratio of specific heats, η is the resistivity, ν is the viscosity, and S represents energy source terms. The method of solution of (1)-(6) has been described by *Mikić and Linker* [1994]; details of the algorithm are also described by *Lionello et al.* [1998] and *Lionello et al.* [Stability of algorithms for waves with large flows, submitted to *Journal of Computational Physics*, 1998]. In practice, we use the vector potential $\mathbf{A}$, where $\mathbf{B} = \nabla \times \mathbf{A}$, to implement the algorithm. Through the use of staggered meshes, the vector identity $\nabla \cdot \nabla \times \mathbf{A} = 0$ is preserved in discretized form, so that $\nabla \cdot \mathbf{B} = \nabla \cdot \mathbf{J} = 0$ is satisfied to within round-off error throughout the computation.

The calculation described here was performed on a $85 \times 81 \times 64$ nonuniform r, θ, ϕ mesh, with $\Delta r \approx 0.013 R_s$ near the base of the corona and $\Delta\theta \approx 1.6°$ near the equator. The ϕ mesh was uniform, with $\Delta\phi = 5.6°$. The simulation domain extended out to $30 R_s$. A uniform resistivity η was used, corresponding to a resistive diffusion time $\tau_R = 4\pi R_s^2/\eta c^2 = 400$ hours. The Alfvén travel time at the coronal base ($\tau_A = R_s/V_A$) for $|\mathbf{B}| = 10$ G (typical of the high-latitude fields) was 8.3 min (Alfvén speed $V_A = 1400$ km/s), so the Lundquist number τ_R/τ_A was ≈ 2900. A uniform viscosity ν was also used, corresponding to a viscous diffusion time ($\tau_\nu = R_s^2/\nu$) of 40 hours. A well-known problem with numerical MHD computations is that the achievable values of resistivity and viscosity are much larger than solar values [e.g., *Mikić and Linker*, 1994]. Our two-dimensional calculations of helmet streamer equilibria [e.g., *Linker and Mikić*, 1995] indicate that solutions with larger diffusion typically have slightly larger closed field regions and smaller magnetic energies than those with smaller diffusion, but the solutions are qualitatively similar.

The term S in the energy equation (6) includes resistive and viscous dissipation ($\eta J^2 + \nu\rho\nabla\mathbf{v} : \nabla\mathbf{v}$). Because we use enhanced values of the viscosity and resistivity relative to coronal values, the heating rate associated with these terms may be unphysically large, and in the calculations presented here we set $S = 0$. Typically, we find that inclusion of resistive and viscous dissipation has little effect on the overall magnetic field solution [*Mikić and Linker*, 1994]. With $S = 0$, (6) yields polytropic solutions; that is, $d(p\rho^{-\gamma})/dt = 0$ (where d/dt is an advective derivative). (In this case, γ becomes the polytropic index and is not necessarily related to the ratio of specific heats.) These solutions have the advantage that relatively simple models can match many of the properties of the corona. However, values of γ close to 1 ($\gamma = 1.05$ for the calculations reported here) are necessary to produce radial density and temperature profiles that are similar to coronal observations; this reflects the fact that important thermodynamic processes have been omitted from the energy equation [*Parker*, 1963]. The inclusion of more sophisticated thermodynamics in (6), such as coronal heating, thermal conduction parallel to $\mathbf{B}$, radiative losses, and Alfvén wave dissipation, will be the subject of a future paper. These processes have been considered previously in one-dimensional (1-D) models [e.g. *Withbroe*, 1988; *Habbal et al.*, 1995], and some of these effects have been incorporated in two-dimensional (2-D) models [*Suess et al.*, 1996; *Mikić et al.*, 1996a].

To perform a computation of the solar corona applicable to the WSM time period, we obtained synoptic maps (collected during a solar rotation by daily measurements of the line-of-sight magnetic field at central meridian) from the National Solar Observatory at Kitt Peak (NSO/Kitt Peak). Using the NSO/Kitt Peak maps for Carrington rotations 1912 and 1913, we developed a composite map using data from the period August 12 (CR1912, 122° Carrington longitude) to September 9, 1996 (CR1913, 122° longitude). This interval is centered on August 26 (CR1913, 303°), about the time that the "elephant's trunk" coronal hole was at disc center. The composite NSO/Kitt Peak map was used to specify the radial magnetic field at the photosphere B_{r0} (in the manner described by *Wang and Sheeley* [1992]). Line-of-sight projection effects make accurate measurement of the polar fields difficult, so that the measured polar fields are less reliable. For the case shown here, we replaced the magnetic field within 11° of each pole with values extrapolated from a smooth fit of the axisymmetric component of the measured field between 11° and 30° of the poles. A very small monopolar component present in the data was subtracted out. The NSO/Kitt Peak data are interpolated to the grid resolution used in the calculation, with care taken to preserve the magnetic flux in the interpolation. Plate 1 shows the original NSO/Kitt Peak synoptic map, as well as the resulting map used for the MHD computation. In the map used in the computation, fields near the poles had strengths of 10-12 G, while fields near the active region were ~ 40 G.

In addition to B_{r0}, the MHD calculations require the specification of density ρ_0 and pressure p_0 at the coronal base [(*Linker and Mikić* [1997] describe the boundary conditions in more detail). We assumed N, the plasma number density (that is, $N = n_e = n_i$, where n_e and n_i are the electron and ion number densities, respectively) at the coronal base to be 2×10^8 cm^{-3} and the temperature T_0 (defined by the ideal gas law $p = 2NKT$) to be 1.8×10^6 K. Rigid rotation corresponding to a sidereal period of 26 days was also imposed.

For the initial condition for the fluid variables (ρ, p, and $\mathbf{v}$), we choose the spherically symmetric transonic Parker solar wind solution [*Parker*, 1963] consistent with the boundary values of ρ and p. In the absence of a magnetic field and with no rotation, this solution yields a steady state. For the initial magnetic field, we compute a potential field by numerically solving Laplace's equation with boundary conditions on B_r specified as B_{r0} (shown in Plate 1) at $r = R_s$ and zero at the outer boundary. This yields an initial (current free) field of entirely closed field lines. Together, this specification of ρ, p, $\mathbf{v}$, and $\mathbf{B}$ describes a nonequilib-

rium initial state for the time-dependent computation. We integrate the MHD equations (1-6) forward in time until a steady state is reached. The solution obtained provides a 3D description of the solar corona, under the assumption that the large-scale coronal magnetic field is not changing significantly for the time period of interest (an assumption that, while never strictly true, is often reasonably well satisfied during minimum solar activity).

3. Results

The typical solar minimum corona exhibits a well-defined streamer belt with coronal holes in the polar regions. The streamer belt is believed to be formed by closed magnetic field lines that have confined the solar plasma, while in coronal holes the solar wind streams outward freely along open magnetic field lines. In section 3.1, we show that the 3-D MHD solution we have obtained exhibits these basic properties. However, the primary purpose of our paper is to compare the solutions with available coronal and heliospheric data. This requires us to view the results in a manner that is similar to the actual observations. In sections 3.2 and 3.3, we describe comparisons of the MHD computations with white-light measurements and disc emission and absorption images. The magnetic field structure predicted by the model can also be tested with interplanetary measurements. In section 3.4, we discuss comparisons of this type, and we use the MHD model to infer the source location of solar wind properties measured by WIND and Ulysses.

3.1. MHD Solution

We first show some of the general properties of the 3-D MHD solution. The properties of the plasma density and velocity from the solution are closely related to the associated magnetic field topology. This can be seen in Plate 2, which shows magnetic field lines from the MHD calculation superimposed on a color contour plot of the radial velocity v_r in the plane perpendicular to the line of sight (v_r is the dominant component of the velocity and closely resembles $|v|$). The plate shows that, as expected, the closed field regions are associated with nearly stagnant plasma flow. There is slow flow near the streamer belt in the equatorial regions, and faster flows are associated with the polar regions of the corona.

The contrast of plasma properties between the open and closed field regions can also be seen in Plate 3, which shows v_r, N (the plasma number density), and T (the plasma temperature) at $r = 1.5R_s$ (Plate 3a), $r = 2.5R_s$ (Plate 3b), and $r = 10R_s$ (Plate 3c). The streamer belt can be identified as the region of nearly zero flow velocity and increased plasma density at $r = 1.5R_s$ and $r = 2.5R_s$ (we demonstrate the closed magnetic field topology of this region in Figure 2). The strong "warp" in the structure of the streamer belt seen at 240° and 300° longitude is associated with northern and southern extensions of the coronal hole boundaries, which are discussed in subsequent sections. Higher N in the streamer belt at $r = 1.5R_s$ is associated with the active region near 240° longitude. The plasma temperature also shows different properties between open and closed field regions; however, we caution the reader that because of the simplistic nature of the energy equation chosen, T is likely to be the least realistic aspect of the calculation. Variations in T at each height are typically less than 10%, and isothermal (T = constant) solutions would probably yield qualitatively similar properties to those shown here.

At $10R_s$, the magnetic field is essentially open everywhere. Faster flow is still present at the poles relative to the equatorial regions, and the region near the heliospheric current sheet is marked by higher N than the surroundings. The low plasma pressure region (both low N and T near 240° longitude) is spatially coincident with stronger magnetic fields arising in the extension of the coronal hole here. At $10R_s$ and above, the flow is super-Alfvénic and supersonic nearly everywhere. At this height and outward, the morphological features of the solution change very little, because information propagates outward only. Quantitatively, N and T decrease with radius while v_r increases, as is shown in Figure 1.

The MHD solution shows the qualitative features we expect of the corona: stagnant flow and higher density in the closed field regions, faster flows near the poles, and slower flow near the streamer belt. To demonstrate that the solution can describe specific coronal observations, we must cast the results in a form that is similar to the measurements. Two of the most common forms of coronal data are white-light and disc emission images. Views of streamers on the limb and coronal holes on the solar disk together provide diagnostics of the three-dimensional structure of the corona that can be used to test coronal models. In the following two sections we show how the MHD solution compares with these observations.

Despite the qualitative similarities, the solution has important quantitative differences from the real corona and solar wind. In particular, the density contrast between open and closed field regions is smaller than observed, and the fast solar wind speed in the simulation is too low compared to measurements. These inaccuracies in the solution are directly related to the simple energy equation assumed; improvements of these aspects of the solution are discussed further in section 4.

3.2. Comparison With White-Light Images

White light emitted from the solar corona is predominantly produced by electron scattering in the coronal plasma. The signal measured by a coronagraph is thus sensitive to the line-of-sight integrated electron density of coronal structures. When the limbs of the Sun are viewed in white light (with the photosphere occulted), the dense streamers show up as bright regions while

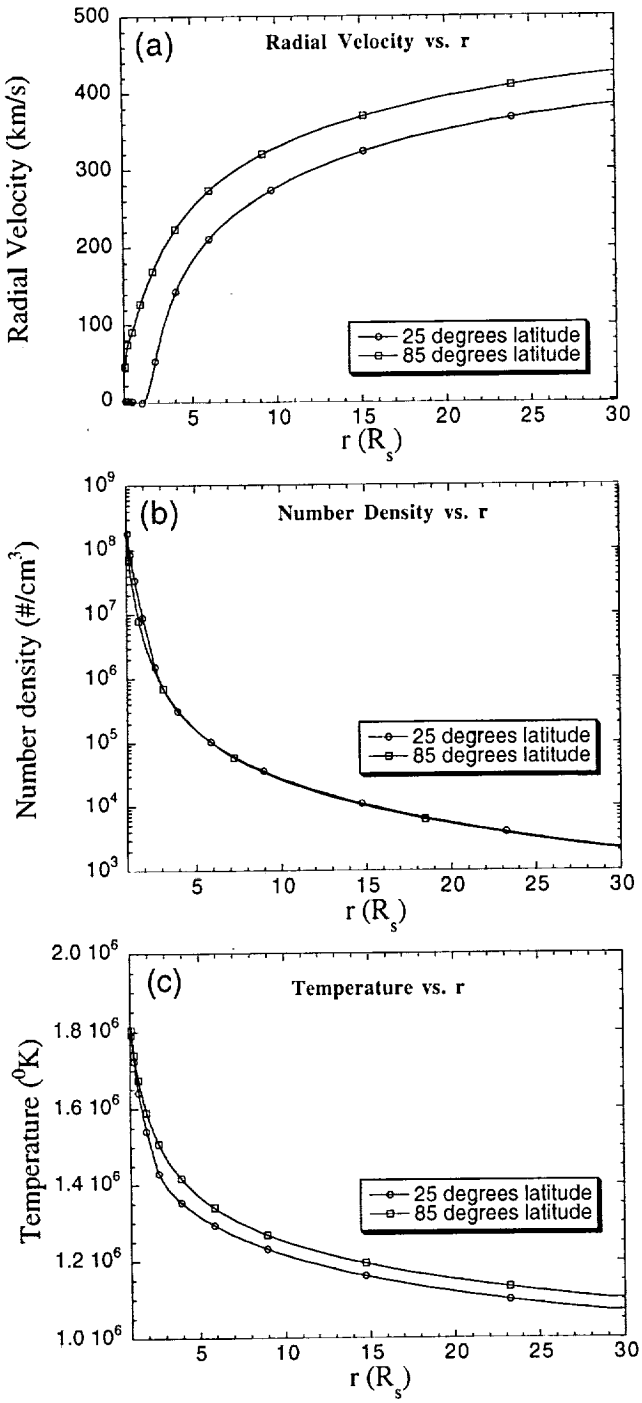

Figure 1. (a) Radial velocity, (b) number density, and (c) temperature versus radius at two different latitudes, for longitude 281° (corresponding to the west limb of Plate 2). The radial cut at 25° latitude passes through the closed-field region and then cuts across open field lines that bend toward the equator. The cut at 85° latitude is strictly in the open field region.

the less dense coronal holes appear dark. Deducing the three-dimensional plasma density directly from coronagraph images is possible using tomographic techniques [*Zidowitz et al.*, 1996; *Zidowitz*, this issue]. On the other hand, it is relatively straightforward to use the plasma density from a model to develop a simulated coronal image. Frequently, the polarization brightness pB is the observed quantity. The distribution of pB in the plane of the sky is proportional to the line-of-sight integral of the product of the electron density and a scattering function that varies along the line of sight [*Billings*, 1966]. Plate 4 shows simulated pB images from the MHD model for 4 days during the WSM time period. Also shown are tracings of magnetic field lines for the same views. For comparison, pB observed with the Mauna Loa Solar Observatory's Mark 3 K-coronameter (MLSO MKIII) are also shown. The streamer belt structure predicted by the model is qualitatively similar to the observations, although there are also significant differences.

Another way of examining coronal structure during a solar rotation is to assemble the white-light measurements throughout the rotation at a particular radius into a chart of brightness versus latitude and longitude. These are often called synoptic images. An example for MLSO MKIII data taken during WSM at $r = 1.15R_s$ and $r = 1.75R_s$ is shown in Plates 5a and 5b. Plates 5c and 5d (same format as Plates 5a and 5b) show data at $r = 2.35R_s$ and $r = 5R_s$ obtained from the large-angle and spectrometric coronagraph (LASCO) aboard the SOHO spacecraft. Also shown in Plates 5a-5d are simulated synoptic images from the MHD model, developed by processing simulated pB images in the same manner as the MLSO MKIII and LASCO data.

The simulated and actual synoptic images show many similar overall features, indicating that the structure of the streamer belt during WSM has been captured by the MHD model. With increasing height, the streamer belt thins because of the expansion of the magnetic field from the coronal holes. At $5R_s$, the streamer belt begins to have a sheet-like appearance similar to the heliospheric current sheet. Both the observations and the simulation show a dark region breaking up the streamer belt near 270°; this phenomenon is associated with the elephant's trunk coronal hole, discussed in more detail in the next section.

3.3. Comparison With Disc Images

Emission from the disc of the Sun provides another means of studying coronal structure. Coronal holes are typically identified from disc images of emission (at various wavelengths) by their low emission intensity relative to other regions of the solar atmosphere. Coronal holes are believed to be associated with open magnetic field regions. The expansion of the solar wind from coronal holes is thought to give rise to the lower plasma densities and temperatures responsible for the observed lower levels of emission. Absorption in the 10830 Å (He I) line is enhanced (that is, brightness is decreased) by increased EUV and X ray emission, so the footpoints of bright X ray loops appear dark and coronal holes appear bright in He 10830 Å images [*Harvey*, 1996]. The National Solar Observatory at Kitt Peak publishes daily maps of coronal hole boundaries deduced from He

10830 Å images and measurements of the photospheric magnetic field polarity. There is often a good (but not exact) correspondence between coronal holes identified in He 10830 Å and soft X rays [*Harvey*, 1996].

Perhaps the most conspicuous coronal feature observed during WSM was the elephant's trunk coronal hole that extended from the northern polar regions to the equator. The elephant's trunk was apparent in several different wavelengths, including SOHO extreme ultraviolet imaging telescope (EIT) images, NSO/Kitt Peak He 10830 maps, and Yokhoh soft X rays. This interesting feature was most visible around August 26-27 and provides another test of the model's ability to predict coronal structure.

To determine the boundary between open and closed field regions, we traced magnetic field lines from each pixel on the lower boundary. By delineating the regions where the field lines returned to the Sun (closed-field regions) from the regions where the field lines reached the outer boundary (open-field regions), we produced a map of the coronal hole boundaries predicted by the MHD model, under the assumption that open-field regions correspond to coronal holes observed in emission (or absorption) lines. Plate 6 shows the results of this calculation. Plate 6a shows tracings of the magnetic field with B_r mapped on the solar surface, as would have been seen on August 27, 1996. Plate 6b shows the same field tracings and the same view but with the open-field regions (black) and closed-field regions (gray) mapped on the surface of the Sun. For comparison, the NSO/Kitt Peak coronal hole boundaries and SOHO EIT images showing the elephant's trunk coronal hole are shown in Plates 6c-6e. It is apparent that the model has captured the extended coronal hole feature, although the observations show the coronal hole extending to even lower latitudes and hooking eastward into the active region.

We note that the model also predicts an equatorial coronal hole in the south (east of the elephant's trunk). A coronal hole in the south appears to be present in the EIT 195 Å (Fe XII) and 284 Å (Fe XV) images, though it is partially obscured by the bright emission from the nearby active region. However, it has not been identified as a coronal hole in the NSO/Kitt Peak map. This highlights one of the difficulties with trying to interpret magnetic field topology from spectroscopic measurements: a coronal hole can appear to be present in one wavelength but may not be visible in another. In the synoptic white-light image (Plate 5) a break appears in the streamer belt extending from both the north and the south. This feature is present in both the observations and the MHD computation and, according to the model, is caused by the northern and southern coronal holes "pinching" on either side of the active region. This dark region in the white-light data suggests that the southern equatorial coronal hole is indeed present. As discussed in section 3.3, the detection of a polarity reversal in the interplanetary magnetic field that maps back to the southern coronal hole extension further supports this interpretation.

Plate 7a shows a "synoptic" EIT 195 Å image, generated by assembling measurements taken at central meridian, similar to the construction of synoptic charts of the magnetic field. The measurements have been binned by sine(latitude), which has the effect of compressing the polar regions into a smaller area. The image shows the polar coronal holes and elephant's trunk for the WSM time period. Note that the coronal hole area in the northern polar regions is larger than in the south. This asymmetry in the coronal holes is enhanced because of the 7° tilt of the solar rotation axis present during this time period, but would still be visible even if there were no tilt. The southern equatorial coronal hole (visible in the daily images, as discussed above) is more difficult to see in the synoptic image, perhaps because it is obscured by the neighboring active region.

Plate 7b shows the coronal hole boundaries predicted by the MHD calculation, in the same sine(latitude) format as Plate 7a. Open-field regions are depicted as black, and closed-field regions are shown in gray. There are many qualitative similarities between the coronal holes identified in EIT and the open-field regions in the MHD model, including the presence of the elephant's trunk coronal hole and the larger area of northern coronal holes relative to southern. However, the coronal hole area in both the north and south is larger in the MHD model than in the EIT image. The most notable disagreement between the model and observations are the equatorial coronal holes in the north near 40° and 350° Carrington longitude. While a southward extension of the coronal hole boundary seems to be present in the EIT data near 40°, it is not nearly as pronounced as in the MHD calculation. Neither the EIT daily images nor the NSO/Kitt Peak daily coronal hole maps shows obvious equatorial coronal holes in these regions. These features are perhaps the most significant difference between the MHD model and Whole Sun Month observations, and we discuss them further in section 4.

We plot the open-/closed-field boundaries as a function of radius in Figure 2. Note the close association between the field topology at $r = 1.5R_s$ and $r = 2.5R_s$ and the plasma properties shown in Plate 3. At $5R_s$ the closed-field region resembles the heliospheric current sheet, and above this radius the field is essentially open everywhere. The magnetic field expands rapidly from the coronal holes; therefore, as shown in the next section, field lines that are located near the equator at large distance from the Sun frequently map back to much higher latitudes at the solar surface.

3.4. Inferring the Source Location of In Situ Solar Wind Measurements

One of the reasons for intense interest in coronal holes is because they are believed to be regions of open magnetic field where the solar wind expands outward. The solar wind is far from uniform and is often described

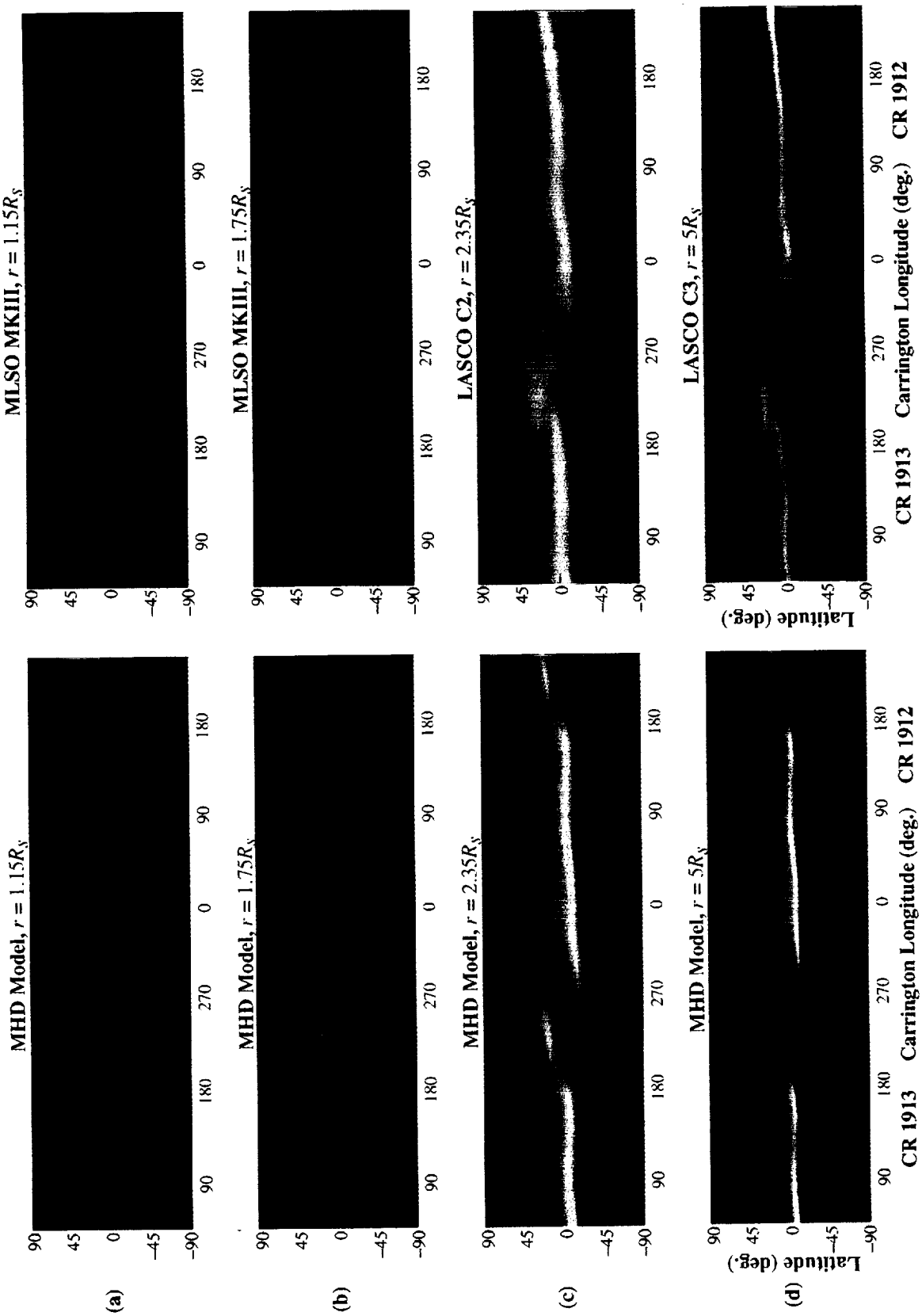

Plate 5. Comparison of the MHD model with white-light synoptic images. On the right, daily white-light data from the east limb have been assembled into charts of brightness versus latitude and longitude for different heights. On the left, simulated synoptic images for the MHD model have been created by processing simulated pB images in the same manner. Comparisons of the model with MLSO data at (a) $r = 1.15R_s$ and (b) $r = 1.75R_s$ are shown. (c) Comparison with large-angle and spectrometric coronagraph (LASCO) C2 data at $r = 2.35R_s$. (d) Comparison with LASCO C3 data at $r = 5R_s$.

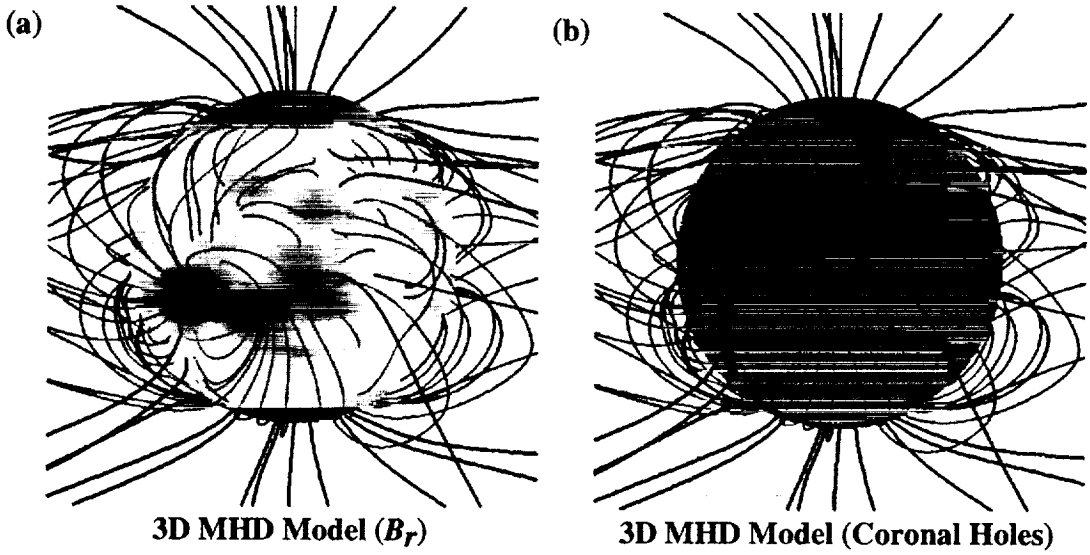

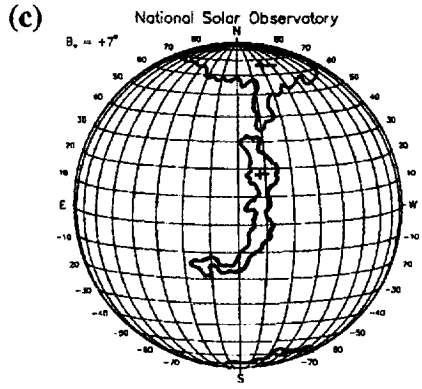

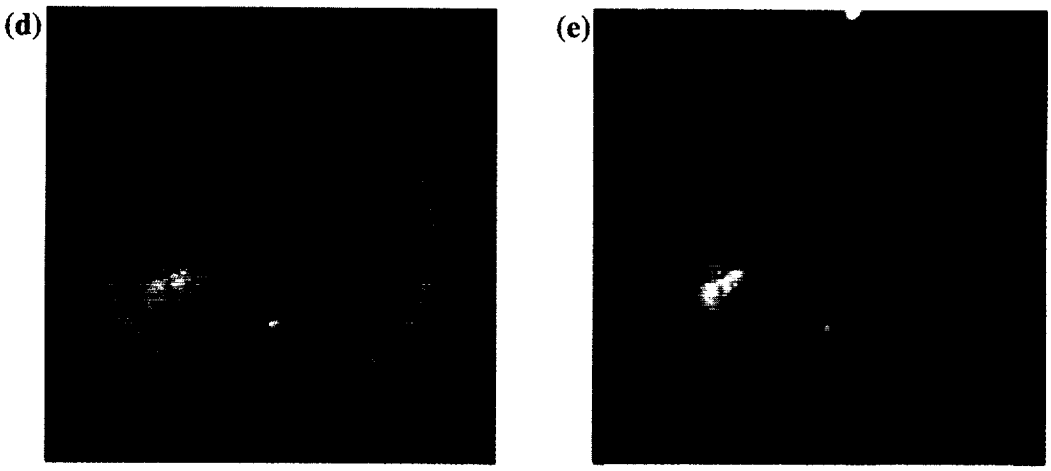

Plate 6. Comparison of the MHD model with coronal holes deduced from measurements of emission and absorption lines. (a) Magnetic field lines from the MHD model, as would be viewed on August 27, 1996. B_{r0} is contoured on the solar surface in the same format as Plate 4c. (b) Same as Plate 6a, with open-field regions shown in black and closed-field regions shown as gray. Assuming that open-field regions in the model correspond to coronal holes, a feature similar to the elephant's trunk coronal hole is produced by the model. (c) A coronal hole map for August 27, 1996, from NSO/Kitt Peak. The elephant's trunk coronal hole is clearly visible. Note that it actually extends below the equator. (d) An extreme ultraviolet imaging telescope (EIT) 195 Å (Fe XII) image for the same day. The elephant's trunk coronal hole is visible and very similar to the Kitt Peak coronal hole map. Note that a possible coronal hole is visible in the south, east of the active region. (e) Same as Plate 6d, but for an EIT 284 Å (Fe XV) image.

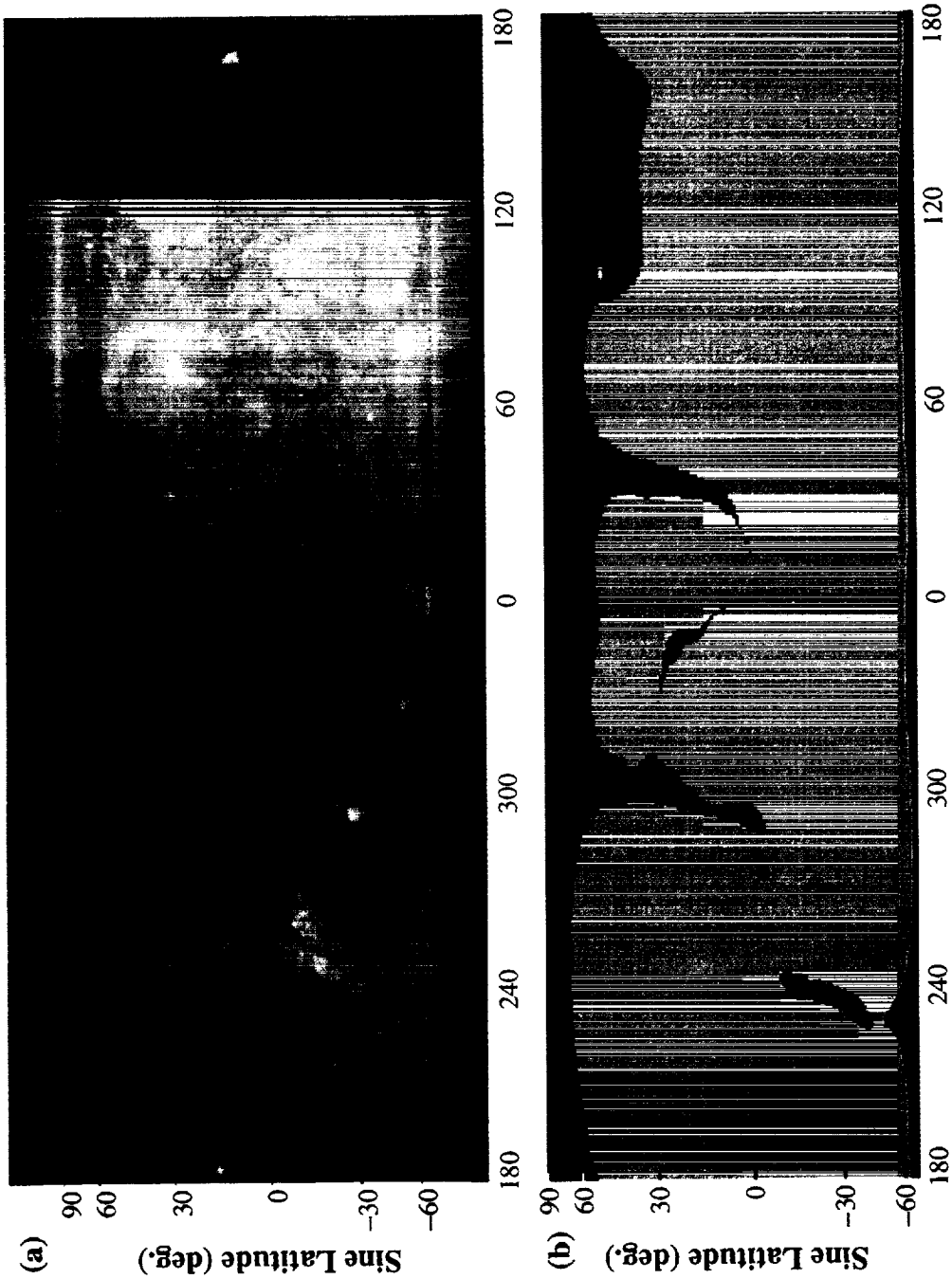

Plate 7. (a) An EIT 195 Å (Fe XII) synoptic image for the Whole Sun Month time period (see text). The elephant's trunk coronal hole near 300° Carrington longitude is clearly visible. A coronal hole in the south may be present but obscured by emission from the neighboring active region. During Whole Sun Month, the solar rotation axis was tilted about 7° toward Earth, making the northern polar regions more visible than those in the south. Even if no tilt were present, one finds that the coronal hole area in the north is larger than in the south. (b) Open (black) and closed (gray) regions predicted by the MHD computation. The 7° tilt of the solar rotation axis during this time period has been included. The elephant's trunk coronal hole and larger coronal holes in the north are present in the model. A prominent equatorial extended coronal hole is also present near 40° Carrington longitude.

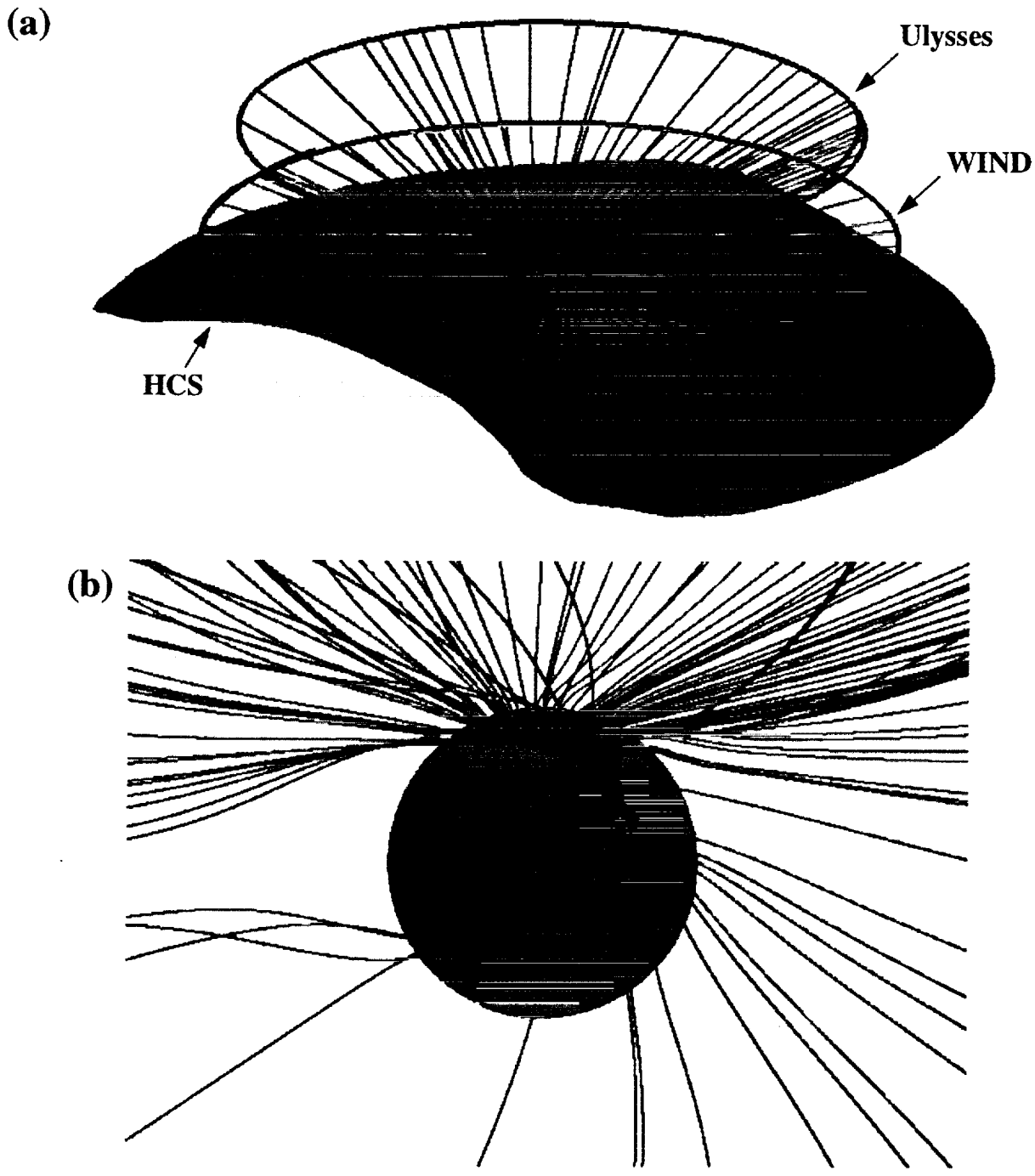

Plate 8. (a) Magnetic field lines in the MHD model, together with the heliospheric current sheet (HCS) and the Ulysses and WIND trajectories (mapped back to $15R_s$). The field lines traced from Ulysses (green) and WIND (cyan) are shown for data corresponding to the Whole Sun Month period. The Ulysses and WIND trajectories are shown in the Sun's rotating frame. (b) A close-up view of the field lines near the Sun. The model correctly predicts that Ulysses did not cross the HCS during Whole Sun Month but that WIND crossed briefly below the HCS and then returned to regions of positive polarity.

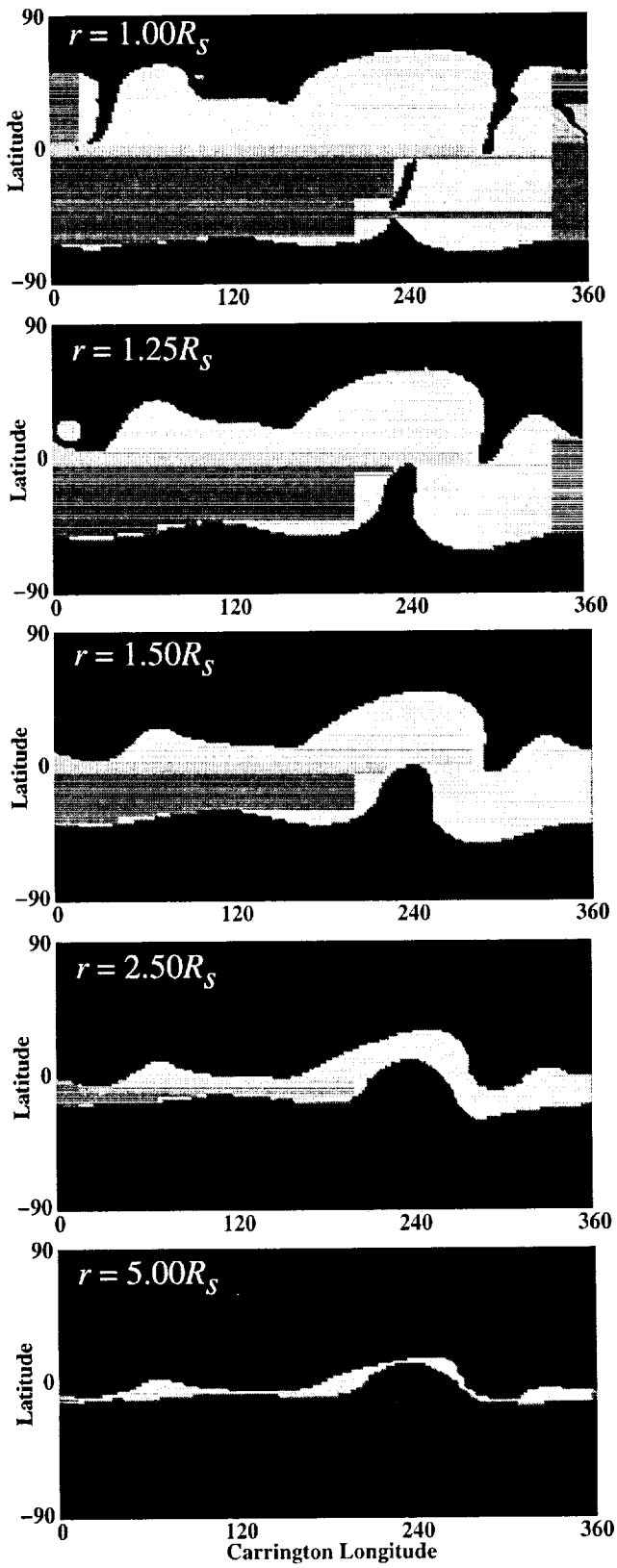

Figure 2. Open (black) and closed (gray) field line regions, as determined from the MHD computation, as a function of radius.

as being either "slow" (300-500 km/s) or "fast" (600-800 km/s). The solar origin of fast and slow solar wind streams is poorly understood. Measurements from the Ulysses spacecraft have demonstrated that uniformly fast solar wind is present at the poles of the Sun during solar minimum [*Phillips et al.*, 1995]. Spacecraft near the ecliptic plane, such as WIND, typically measure predominantly slow solar wind interrupted by occasional high-speed streams. Equatorial coronal holes have long been associated with recurrent high-speed solar wind streams near Earth [*Bohlin*, 1977; *Crooker and Cliver*, 1994; *Harvey*, 1996]; therefore the identification of features like the elephant's trunk coronal hole is regarded as particularly important for deducing the solar source of solar wind measured near the ecliptic plane. During the WSM time period, WIND observed predominantly slow wind but intervals of fast wind were indeed present. On the other hand, the Ulysses spacecraft (moving slowly southward after crossing the north pole of the heliosphere in April 1995) reached low enough latitudes ($\approx 28°$) that intervals of slow wind were measured. In fact, the WSM period corresponded to the first encounter of slow solar wind measured by Ulysses since its foray into northern latitudes in early 1995 [*Riley et al.*, this issue]. Thus both WIND and Ulysses saw transitions between fast and slow wind during WSM.

To investigate the solar origin of the features observed by Ulysses and WIND, we located the source regions of the solar wind at the Sun using the following technique. Since the MHD calculation was performed only to $30R_s$, we first mapped the locations from the spacecraft to $15R_s$ (to be well inside the domain of calculation), using a ballistic approximation in which the change in longitude is computed from the time interval required for a plasma parcel to travel from $15R_s$ to the spacecraft location, using the measured in situ solar wind velocity; we then used the MHD field lines to trace back from $15R_s$ to the solar surface. (Varying the mapping distance between $5R_s$ and $30R_s$ caused individual footpoints to change, but did not change overall trends.) Plate 8a shows tracings of field lines, including the Ulysses and WIND trajectories (mapped back to $15R_s$) and the heliospheric current sheet (HCS) (defined as the surface $B_r = 0$). Plate 8b shows a close-up of the field lines near the solar surface. Note that the WIND trajectory intersects the HCS during this time period, but the Ulysses trajectory does not. Therefore the MHD model predicts that two HCS crossings should have been observed by WIND during this time period, and no crossings should have been observed by Ulysses, which is consistent with the spacecraft magnetic field measurements, as described next.

Plate 9a shows the magnetic field polarity (determined from 1 hour spacecraft data, averaged over 6 hours) mapped back to the Sun, as well as the coronal hole boundaries deduced from the MHD model. The

top trace shows Ulysses measurements; the lower trace shows WIND measurements. The polarity of the measured magnetic field was determined by comparing the magnetic field direction angle Φ_B with the Parker spiral angle Φ_P (determined from the measured solar wind speed). Points for which Φ_B was within 45° of Φ_P were assigned positive polarity (shown in red); points for which Φ_B was within 45° of $\Phi_P - 180°$ were assigned negative polarity (shown in blue); for all other points, the spiral direction did not obviously correspond to inward or outward fields (shown in white). Interplanetary magnetic field measurements usually have a high level of fluctuations because of wave activity in the solar wind and sometimes from the passage of transients. Individual measurements may not lie along the spiral direction for either polarity, or may even have the opposite polarity, without the presence of an HCS crossing. Except for discrepancies of this kind, with a perfect model of the heliospheric magnetic field, the red points should always map back to positive polarity regions of the Sun and blue points should always map back to negative polarity regions.

For Ulysses observations (top trace in Plate 9a), we see that the predominant positive polarity for the magnetic field is both predicted by the model and measured at the spacecraft (red points mapping back to positive-polarity northern polar coronal holes). This is not surprising, as the spacecraft was still at high enough latitude to be well away from the HCS during this time period. For WIND, the model predicts that the spacecraft passed below the HCS (into negative polarity fields) near 240° Carrington longitude (at the Sun) and back above the HCS (into positive polarity fields) near 220° longitude. These are the points mapping back to the southern equatorial coronal hole. This first HCS crossing was predicted quite accurately by the model (blue points in the southern equatorial coronal hole). The passage of the spacecraft back to positive polarity appears to have occurred somewhat later than that predicted by the model, as evidenced by the clustering of blue points in the northern coronal holes between 170° and 220°.

An analysis of the WIND magnetic field and electron pitch angle data indicates that it is difficult to accurately identify the HCS crossing back to positive polarity fields. Indeed, WIND measured extended intervals of mixed polarity, during this time, prior to the return to positive polarity. There were inconsistencies between the crossings identified from the magnetic field data and the electron pitch angle data. The sharpness of the crossing from positive to negative polarity ("inbound") identified in the WIND data and the less clearly identified return to positive polarity ("outbound") is consistent with the shape of the HCS shown in Plate 8a: the HCS has a steeper gradient on the inbound crossing and a "glancing" encounter with the HCS on the outbound crossing. This may explain the apparent disagreement between the MHD model results and the magnetic field polarity measurements.

The WIND observations of negative polarity fields suggest that the southern equatorial coronal hole identified in section 3.2 is indeed present. This is clearly illustrated by the field lines in Plate 8, which shows that the magnetic field maps back to the southern equatorial coronal hole (negative polarity) when WIND crosses below the HCS.

The overall good agreement between the magnetic field polarities observed by Ulysses and WIND and those predicted by the MHD computations suggests that it is possible to use the model to deduce the source locations of features measured in interplanetary space. Plate 9b is in the same format as Plate 9a, except that measured solar wind speed for the WSM time period is now plotted, with red indicating the highest solar wind speeds and blue the lowest. The top (mostly red) trace is for Ulysses, which observed predominantly fast wind but measured some slow wind that maps back to longitudes near 240° on the Sun. WIND observed primarily slow wind, but there were two intervals of fast wind; one interval maps back to the elephant's trunk coronal hole and the other to near 120° longitude.

Plate 10 presents two views of the same solar wind source location mapping as shown in Plate 9b. Plate 10a shows the view from Earth on August 27; Plate 10b shows a polar view. A general trend one sees in these plates is that slow wind velocity usually maps back to regions close to the coronal hole boundaries; fast wind typically comes from deeper within coronal holes. Additional comparisons with solar wind speed determined from interplanetary scintillation measurements are consistent with this interpretation [*Breen et al.*, this issue].

4. Discussion

The data comparisons described in the previous sections show that the MHD model gives a good overall description of the solar corona observed during Whole Sun Month. The approximate shape of the streamer belt and coronal hole boundaries, including the elephant's trunk coronal hole, are reproduced by the model. Two HCS crossings for the WIND spacecraft were predicted by the model and, in fact, observed by the spacecraft.

Of course, many details of the observations do not match the computational results. For example, the elephant's trunk coronal hole extends to lower latitudes than predicted by the computation. The tilt and size of streamers observed on individual days sometimes differ from those predicted, and there are many fine-scale features in the observations that are not present in the computations. Also, even during solar minimum, the Sun's magnetic field is always evolving and a synoptic magnetic field map can yield, at best, an approximation of the state of the corona. For example, daily images show significant structural changes in the ele-

phant's trunk coronal hole during Whole Sun Month [*Zhao et al.*, this issue]. In fact, it is apparent from the white-light synoptic observations shown in Plate 5 that the elephant's trunk coronal hole changes significantly from Carrington rotation 1912 to Carrington rotation 1913.

Improvements to the computations can, in principle, resolve these differences. Some of the differences could be caused by errors in the determination of the polar fields, which are difficult to measure with line-of-sight magnetographs. Line-of-sight magnetographs also give no information about twist or shear in the magnetic field, and this could change the size and shape of streamers, as well as the connectivity of the magnetic field lines. Most importantly, the free energy in the magnetic field, which is expected to be largely in parallel currents in the corona (i.e., in the twist in the magnetic field), is not determined by line-of-sight magnetograms. Obviously, the level of energization of our simulated corona (and its propensity to launch coronal mass ejections) will be affected by this important lack of data. A full-disc vector magnetograph, such as is planned by the National Optical Astronomy Observatories (NOAO) Synoptic Optical Long-term Investigations of the Sun (SOLIS) project, can help to address these ambiguities. Vector information about the magnetic field at the photosphere can be incorporated into the MHD calculations, as has been done previously in modeling active-region magnetic fields [*Mikić and McClymont*, 1994; *Mikić et al.*, 1996b]. With improved computational speed and massively parallel computers, higher-resolution computations can be performed to capture details that are smaller than our present grid resolution. To study the evolution of coronal fields, we plan to perform time-dependent calculations using sequences of magnetograms to specify the magnetic flux evolution at the photosphere.

One question that arises from our study is the sensitivity of the MHD solution to the input parameters. As described in the introduction, the MHD computation requires boundary conditions for the density, temperature (or pressure), and radial magnetic field at the base of the corona (ρ_0, T_0, and B_{r0}, respectively). Observations of the photospheric magnetic field have been used to specify B_{r0}, but ρ_0 and T_0 have been specified as uniform quantities in latitude and longitude without any direct guidance from solar observations.

We can use the source-surface model to test the sensitivity of the MHD solutions to these parameters. In the source-surface model, the coronal magnetic field is computed from a specified magnetic flux distribution at the photosphere, assuming that the field is potential (current free) and becomes completely radial at some height (the height of the source surface). The source-surface height R_{ss} influences the position and shape of coronal hole boundaries. The lower the value chosen for R_{ss} is, the larger the coronal hole regions tend to be. Similar effects can be found by varying ρ_0 and T_0 in the MHD model. Coronal holes tend to be larger when ρ_0 and T_0 are larger, because increasing these quantities increases the kinetic energy ($\rho v^2/2$) of the solar wind relative to the magnetic energy ($B^2/8\pi$). We have found that the coronal hole boundaries in the MHD model and the source-surface model can often be similar for a given set of parameters. While there is not a unique correspondence between the boundary condition choices in the MHD computation and the R_{ss} used in the source-surface model, we can use the source-surface model as a proxy for how much the MHD solutions are likely to change for different ρ_0 and T_0. To test this sensitivity, we computed a sequence of source-surface models, using the same B_{r0} as in the MHD calculation. Figure 3 shows the coronal hole boundaries computed with the MHD model and with source-surface models with $R_{ss} = 2.2$, 2.5, and $2.7R_s$. Note that the coronal hole boundaries for the MHD calculation and the source-surface model with $R_{ss} = 2.2R_s$ are quite similar. We see that for these parameters, the size of the elephant's trunk coronal hole and the southern equatorial coronal hole vary somewhat, but they are robust features of this magnetic field map. On the other hand, the extended coronal hole boundary in the north near 40° longitude and the equatorial coronal hole near 350° longitude (discussed in section 3.2) are present at $R_{ss} = 2.2R_s$, are diminished at $R_{ss} = 2.5R_s$, and are absent at $R_{ss} = 2.7R_s$. We conclude that these features are likely to be very sensitive to the choice of ρ_0 and T_0 in the MHD computation. For example, a choice of a lower T_0 would yield smaller coronal holes and perhaps diminish or eliminate these features.

In general, the assumption of uniform ρ_0 and T_0 with latitude and longitude is likely to be as unrealistic as the choice of any specific value. This aspect of the calculations is illustrated by quantitative comparisons between the density in coronal holes (S.E. Gibson et al., submitted manuscript, 1998) and the MHD model. While the MHD calculations often show qualitative similarities with the data, the sharp brightness contrasts (sometimes approaching an order of magnitude) between coronal holes and streamers cannot be matched by an MHD computation using uniform ρ_0 and T_0. In principle, we could improve the model's correspondence with observations by using observed variations in coronal density and temperature to guide choices of $\rho_0(\theta, \phi)$ and $T_0(\theta, \phi)$. However, we believe that improvements to the physics in the model, rather than focusing on the fine tuning of parameters in the present model, are likely to yield more significant progress. Indeed, years of research using 1-D models [e.g., *Hollweg*, 1978; *Withbroe*, 1988; *Habbal et al.*, 1995] have shown that incorporating the (unknown) dynamic and thermodynamic process that heat the corona and accelerate the solar wind (albeit, in a parameterized fashion) is apparently necessary for obtaining realistic solar wind solutions. We are presently working on these improvements for multidimensional calculations.

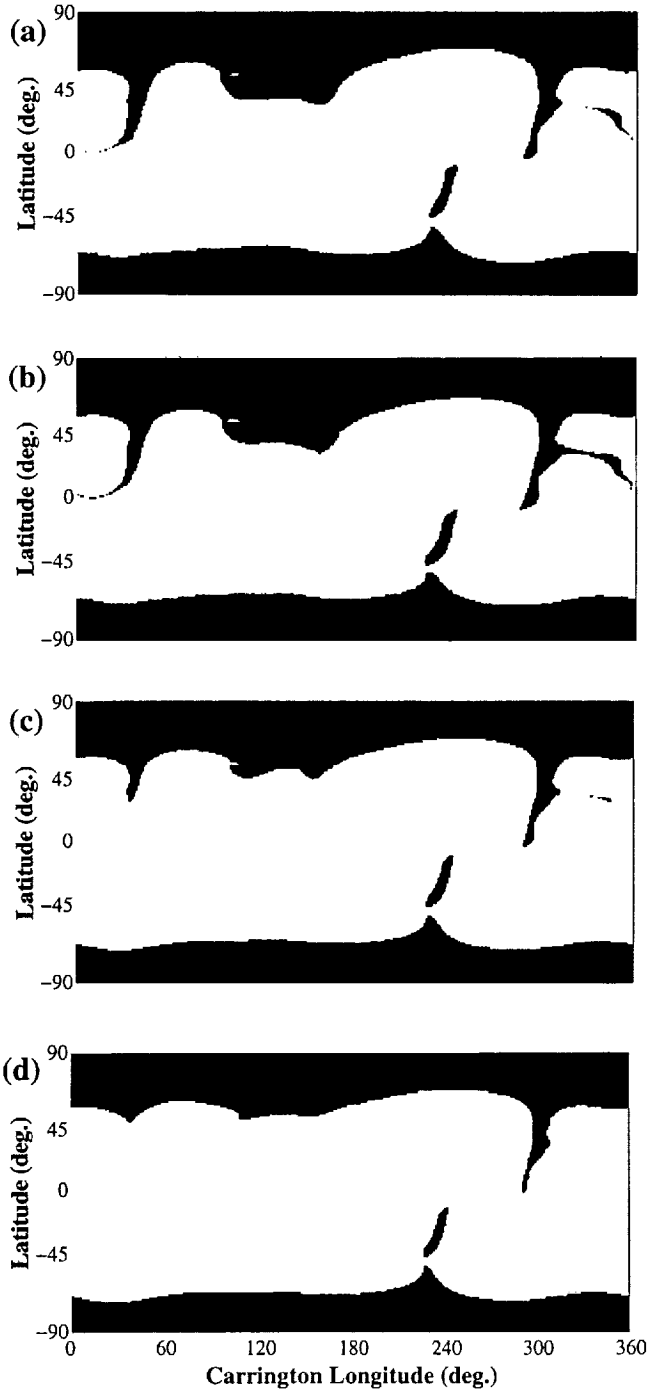

Figure 3. A comparison of coronal hole boundaries (open-field regions) (a) predicted by the MHD computation and source-surface models with source-surface heights of R_{ss} = (b) $2.2R_s$, (c) $2.5R_s$, and (d) $2.7R_s$. Open-field regions are shown in black, and closed-field regions are shown in white. The MHD computation and the source-surface model with $R_{ss} = 2.2R_s$ yield similar results. The coronal hole boundaries recede as R_{ss} is increased, but the elephant's trunk coronal hole (near 300° Carrington longitude) and the southern equatorial coronal hole (near 240° Carrington longitude) are robust features. Similar variations in the MHD result are likely to occur if ρ_0 and/or T_0 are increased (see text).

The need for an improved thermodynamic description in an MHD model is particularly pertinent when investigating the nature of coronal holes as observed in emission lines. The comparisons we have shown for coronal hole boundaries and the open-field regions predicted by the MHD model are, by definition, qualitative. The dark emission features identified as coronal holes clearly are strongly associated with magnetically open regions on the Sun, but the observations do not directly measure field topology. As we have seen for Whole Sun Month, images in different wavelengths can yield different interpretations of the coronal hole boundary. To make a quantitative comparison between coronal models and coronal hole observations requires a more sophisticated model that can be used to reproduce the emission measurement itself. For example, the emission lines observed by EIT arise from the excitation of iron ions, a trace species in the coronal plasma. The iron population in the corona is especially sensitive to temperature. The polytropic energy equation used here is inadequate for describing the temperature of the corona to the desired accuracy. In the future, we hope that with a more sophisticated treatment of thermodynamics in the energy equation, we can model the emission line measurements and thus obtain a clearer understanding of the true correspondence between the dark emission features on the Sun that are identified as coronal holes and regions of open magnetic fields.

Finally, we remark on inferences regarding solar wind sources. One of the fundamental questions in solar and heliospheric physics is the origin of the fast and slow solar wind. *Wang and Sheeley* [1990, 1994, 1995] have argued that the speed of the solar wind is primarily determined by the rate of magnetic flux-tube expansion, with slow wind occurring where the expansion factor is large. We have used the magnetic structure computed with the MHD model to infer the locations of solar wind properties measured by interplanetary spacecraft. We find that the slow wind typically maps back to near the boundaries of open-field regions, with fast wind coming from deeper within the open-field regions. *Neugebauer et al.* [1998] found a similar result for a comparison with Ulysses and WIND data during the Ulysses fast latitude scan (February–April, 1995). The flux-tube expansion factor is usually larger near the boundaries of open-field regions, so our results are not inconsistent with the Wang and Sheeley picture. However, by construction, our model will map any solar wind feature back to somewhere in an open-field region. Another idea that has been proposed for explaining the fast and slow nature of the solar wind is that coronal holes are the source of the fast wind, and time-dependent processes temporarily open closed-field regions and supply the slow wind. If this idea is correct, then a steady-state description of the corona will not suffice for determining solar wind source locations. Thus our results neither confirm nor rule out either of these interpretations.

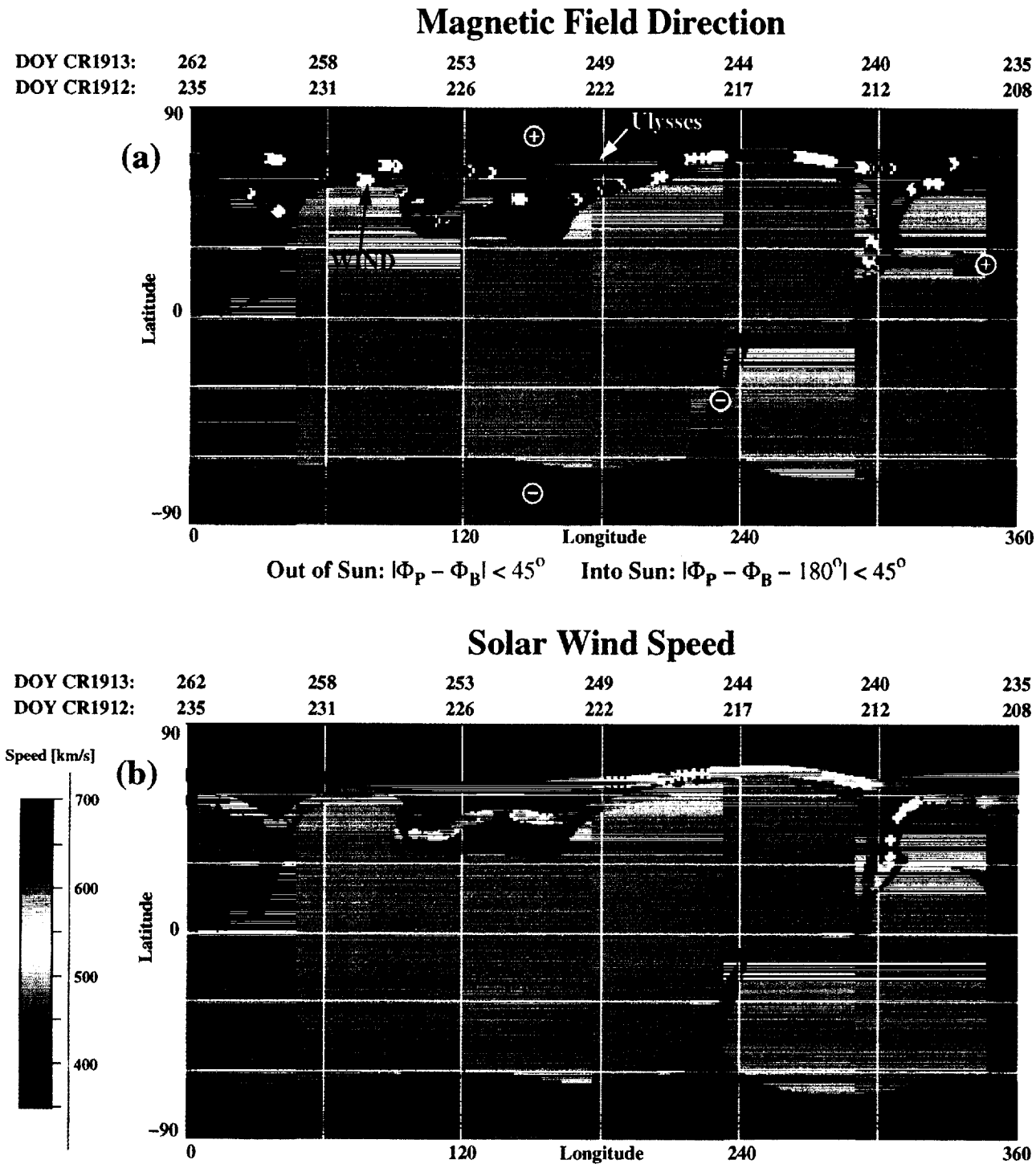

Plate 9. Mapping of interplanetary measurements back to the Sun using the MHD model. Mapped points are plotted versus heliographic latitude and Carrington longitude at the Sun, with coronal holes (open-field regions) predicted by the MHD computation shown in black and closed-field regions shown in gray. The polarity of the photospheric magnetic field in the coronal holes is also shown. (a) The magnetic field polarity measured by Ulysses and WIND. Red (blue) points indicate where positive (negative) polarity fields were measured. Ulysses observed predominantly positive polarity fields and no HCS crossings, consistent with the predictions of the MHD model. WIND observed an HCS crossing to negative polarity the maps to near 240° Carrington longitude, consistent with the MHD model (blue points mapping to the southern equatorial coronal hole with negative polarity). The crossing back to positive polarity fields occurs later than predicted by the model, as discussed in the text. (b) The solar wind speed mapped back to the Sun. Red shows the fastest speeds, and blue shows the slowest. The interval of slow wind measured by Ulysses maps to near the coronal hole boundary (near 240° longitude). Two intervals of fast wind were observed at WIND; one maps to the elephant's trunk coronal hole and the other to a southward extension of the northern coronal hole boundary near 120° longitude.

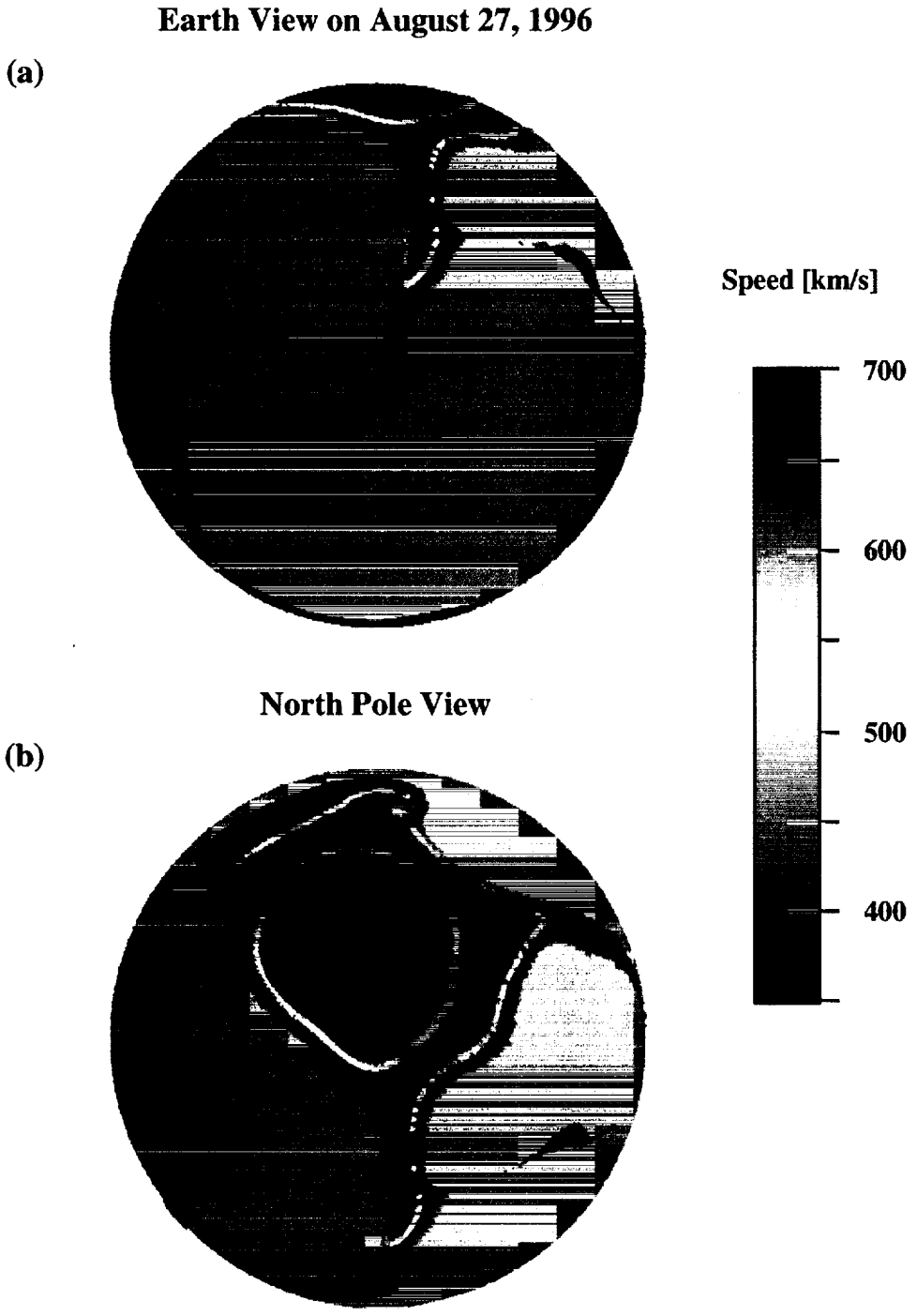

Plate 10. Solar wind speeds measured at Ulysses and WIND and mapped back to the Sun using the MHD model, using the same data shown in Plate 9b. Red shows the fastest speeds, and blue shows the slowest. (a) View as seen from Earth on August 27, 1996. The coronal holes (open-field regions) are shown in black. The highest-latitude trace shows Ulysses measurements. (b) View from above the solar north pole. Slow wind typically maps to near the boundaries of coronal holes, while fast wind typically maps to deeper within coronal holes.

Acknowledgments. We thank the National Solar Observatory at Kitt Peak for the use of their synoptic magnetic charts and daily coronal hole maps. The NSO/Kitt Peak data are produced cooperatively by NSF NOAO, NASA GSFC, and NOAA SEC. Data from the Mauna Loa Solar Observatory Mark III coronameter are courtesy of the High Altitude Observatory, National Center for Atmospheric Research (NCAR), Boulder, Colorado. NCAR is sponsored by NSF. The EIT data shown here are courtesy of the SOHO EIT Consortium. The LASCO data shown here are produced by a consortium of the Naval Research Laboratory (United States), Max-Planck-Institut fuer Aeronomie (Germany), Laboratoire d'Astronomie (France), and the University of Birmingham (United Kingdom). SOHO is a project of international cooperation between ESA and NASA. J. A. Linker and Z. Mikić were supported by the NASA Space Physics Theory, Supporting Research and Technology, and SOHO Guest Investigator programs, by NSF, and by NSF's Space Weather program (jointly funded by NSF and AFOSR). Computations were performed at the National Energy Research Supercomputer Center (NERSC) and the San Diego Supercomputer Center (SDSC). The work by P. Riley was performed under the auspices of the U.S. Department of Energy.

Janet G. Luhmann thanks Y. C. Whang and James Chen for their assistance in evaluating this paper.

References

Altschuler, M. D., and G. Newkirk, Magnetic fields and the structure of the corona, *Sol. Phys.*, *9*, 131, 1969.

Bagenal, F., and S. Gibson, Large-scale structure of the solar corona, *J. Geophys. Res.*, *96*, 17,663, 1991.

Billings, D. E., *A Guide to the Solar Corona*, Academic, San Diego, Calif., 1966.

Bogdan, T. J., and B. C. Low, The three-dimensional structure of magnetic atmospheres, II: Modeling the large-scale corona, *Astrophys. J.*, *306*, 271, 1986.

Bohlin, J. D., An observational definition of coronal holes, in *Coronal Holes and High Speed Wind Streams*, edited by J. B. Zirker, p. 27, Colo. Assoc. Univ. Press, Boulder, 1977.

Breen, A. R., Z. Mikić, J. A. Linker, A. J. Lazarus, B. J. Thompson, D. A. Biesecker, P. J. Moran, C. A. Varley, P. J. S. Williams, and A. Lecinski, Interplanetary scintillation measurements of the solar wind during Whole Sun Month: Comparisons with coronal and in situ observations, *J. Geophys. Res.*, this issue.

Crooker, N. U., and E. W. Cliver, Postmodern view of M-regions, *J. Geophys. Res.*, *99*, 23,383, 1994.

Endler, F. Interaction between the solar wind and coronal magnetic fields, Ph.D. thesis, Gottingen Univ., Gottingen, Germany, 1971.

Gibson, S. E, and F. Bagenal, The large-scale magnetic field and density distribution in the solar minimum corona *J. Geophys. Res.*, *100*, 19,865, 1995.

Gibson, S. E, F. Bagenal, and B. C. Low, Current sheets in the solar minimum corona, *J. Geophys. Res.*, *101*, 4813, 1996.

Gibson, S. E., F. Bagenal, D. Biesecker, M. Guhathakurta, J. T. Hoeksema, and B. J. Thompson, Modeling a simple coronal streamer during Whole Sun Month, *Proceedings of the Fifth SOHO Workshop, Eur. Space Agency Publ. ESA SP-404*, 319, 1997.

Habbal, S. R., R. Esser, M. Guhathakurta, and R. Fisher, Flow properties of the solar wind derived from a two-fluid model with constraints from white light and in situ interplanetary observations, *Geophys. Res. Lett.*, *22*, 1465, 1995.

Harvey, K. L., Coronal structures deduced from photospheric magnetic field and He I λ10830 observations, in *Solar Wind Eight*, edited by D. Winterhalter et al., *AIP Conf. Proc.*, *382*, 9, 1996.

Hoeksema, J. T., J. M. Wilcox, and P. H. Scherrer, The structure of the heliospheric current sheet: 1978-1982, *J. Geophys. Res.*, *88*, 9910, 1983.

Hollweg, J. V., Some physical processes in the solar wind, *Rev. Geophys.*, *16*, 689, 1978.

Linker, J. A., and Z. Mikić, Disruption of a helmet streamer by photospheric shear, *Astrophys. J.*, *438*, L45, 1995.

Linker, J. A., and Z. Mikić, Extending coronal models to Earth orbit, in *Coronal Mass Ejections, Geophys. Monogr. Ser.*, vol. 99, edited by N. Crooker, J. A. Joselyn, and J. Feynman, 269, 1997.

Linker, J. A., Z. Mikić, and D. D. Schnack, Coronal modeling and space weather prediction, in *Solar Drivers of Interplanetary and Terrestrial Disturbances, Conf. Ser.*, vol. 95, edited by K. S. Balasubramaniam, S. L. Keil, and R. N. Smartt, p. 208, Astron. Soc. Pac., San Francisco, Calif., 1996.

Lionello R., Z. Mikić, and D. D. Schnack, Magnetohydrodynamics of solar coronal plasmas in cylindrical geometry, *J. Comput. Phys.*, *140*, 172, 1998.

Mikić, Z., and J. A. Linker, Disruption of coronal magnetic field arcades, *Astrophys. J.*, *430*, 898, 1994.

Mikić, Z., and J. A. Linker, The large-scale structure of the solar corona and inner heliosphere, in *Solar Wind Eight*, edited by D. Winterhalter et al., *AIP Conf. Proc.*, *382*, 104, 1996.

Mikić, Z., and A. N. McClymont, Deducing coronal magnetic fields from vector magnetograms, in *Solar Active Region Evolution: Comparing Models with Observations, Conf. Ser.*, vol. 68, edited by K. S. Balasubramaniam and R. N. Smartt), p. 225, Astron. Soc. Pac., San Francisco, Calif., 1994.

Mikić, Z., J. A. Linker, and J. A. Colborn, A two-dimensional MHD model of solar wind acceleration (abstract), *Eos Trans. AGU*, *77* (17), Spring Meet. Suppl., S216, 1996a.

Mikić, Z., J. A. Linker, and D. D. Schnack, Modeling of active-region magnetic fields, in *Solar Drivers of Interplanetary and Terrestrial Disturbances, Conf. Ser.*, vol. 95, edited by K. S. Balasubramaniam, S. L. Keil, and R. N. Smartt, p. 108, Astron. Soc. Pac., San Francisco, Calif., 1996.

Neugebauer, M., et al., The spatial structure of the solar wind and comparisons with solar data and models, *J. Geophys. Res.*, *103*, 14,587, 1998.

Parker, E. N., *Interplanetary Dynamical Processes*, Wiley-Interscience, New York, 1963.

Phillips, J. L., et al., Ulysses solar wind plasma observations from pole to pole, *Geophys. Res. Lett.*, *22*, 3301, 1995.

Pizzo, V., The evolution of corotating stream fronts near the ecliptic plane in the inner solar system 2. Three-dimensional tilted dipole fronts *J. Geophys. Res.*, *96*, 5405, 1991.

Pneuman, G. W., and R. A. Kopp, Gas-magnetic field interactions in the solar corona, *Sol. Phys.*, *18*, 258, 1971.

Riley, P., J. T. Gosling, D. J. McComas, V. J. Pizzo, J. G. Luhmann, D. A. Biesecker, R. J. Forsyth, J. T. Hoeksema, A. R. Lecinski, and B. J. Thompson, Relationship between Ulysses plasma observations and solar observations during the Whole Sun Month campaign, *J. Geophys. Res.*, this issue.

Schatten, K. H., Current sheet model of the solar corona, *Cosmic Electrodyn.*, *2*, 232, 1971.

Schatten, K. H., J. M. Wilcox, and N. Ness, A model of interplanetary and coronal magnetic fields, *Sol. Phys.*, *6*, 442, 1969.

Suess, S. T., A. H. Wang, and S. T. Wu, Volumetric heating in coronal streamers, *J. Geophys. Res.*, *101*, 19957, 1996.

Usmanov, A. V., A global 3-D MHD solar wind model with Alfvén waves, in *Solar Wind Eight*, edited by D. Winterhalter et al., *AIP Conf. Proc.*, *382*, 141, 1996.

Wang, Y. M., and N. R. Sheeley Jr., The solar origin of long-term variations of the interplanetary magnetic field strength, *J. Geophys. Res.*, *93*, 11227, 1988.

Wang, Y. M., and N. R. Sheeley Jr., Solar wind speed and coronal flux-tube expansion, *Astrophys. J.*, *355*, 726, 1990.

Wang, Y. M., and N. R. Sheeley Jr., On potential field models of the solar corona, *Astrophys. J.*, *392*, 310, 1992.

Wang, Y. M., and N. R. Sheeley Jr., Global evolution of interplanetary sector structure, coronal holes, and solar wind streams during 1976-1993: Stackplot displays based on solar magnetic observations *J. Geophys. Res.*, *99*, 6597, 1994.

Wang, Y. M., and N. R. Sheeley Jr., Solar implications of Ulysses interplanetary field measurements, *Astrophys. J.*, *447*, L143, 1995.

Withbroe, G. L., The temperature structure, mass, and energy flow in the corona and inner solar wind *Astrophys. J.*, *325*, 442, 1988.

Zhao, X. P., and J. T. Hoeksema, Prediction of the interplanetary magnetic field strength, *J. Geophys. Res.*, *100*, 19, 1995.

Zhao, X. P., P. H. Scherrer, and J. T. Hoeksema, The changes of the boot-shaped coronal hole boundary during Whole Sun Month near sunspot minimum, *J. Geophys. Res.*, this issue.

Zidowitz, S., The coronal structure of the Whole Sun Month: A tomographic reconstruction, *J. Geophys. Res.*, this issue.

Zidowitz, S., B. Inhester, and A. Epple, Tomographic inversion of coronagraph images, in *Solar Wind Eight*, edited by D. Winterhalter et al., *AIP Conf. Proc.*, *382*, 165, 1996.

D. A. Biesecker and B. J. Thompson, NASA Goddard Space Flight Center, Code 682, Greenbelt, MD 20771. (email: doug@sungrazer.nascom.nasa.gov; thompson@eitv3.nascom.nasa.gov)

R. J. Forsyth, Blackett Laboratory, Imperial College, London SW7 2BZ UK. (email: r.forsyth@ic.ac.uk)

S. E. Gibson, Department of Applied Mathematics and Theoretical Physics, University of Cambridge, Silver Street, Cambridge, CB39EW UK. (email: sg273@damtp.cam.ac.uk)

A. J. Lazarus, Center for Space Research, Massachusetts Institute of Technology, Cambridge, MA 02139. (email: ajl@space.mit.edu)

A. Lecinski, High Altitude Observatory, National Center for Atmospheric Research, 3450 Mitchel Lane, Boulder, Colorado 80301. (email: alice@hao.ucar.edu)

J. A. Linker, Z. Mikić, and P. Riley, Science Applications International Corporation, 10260 Campus Point Drive, MS E3X, San Diego, CA 92121. (email: linker@iris023.saic.com; mikic@iris023.saic.com; uk2@iris023.saic.com)

A. Szabo, NASA Goddard Space Flight Center, Code 696, Greenbelt, MD 20771. (email: asz@lepasz.gsfc.nasa.gov)

(Received April 17, 1998; revised December 3, 1998; accepted December 3, 1998.)

PHYSICS OF PLASMAS VOLUME 6, NUMBER 5 MAY 1999

Magnetohydrodynamic modeling of the global solar corona*

Zoran Mikić,† Jon A. Linker, Dalton D. Schnack, Roberto Lionello, and Alfonso Tarditi
Science Applications International Corporation, 10260 Campus Point Drive, San Diego, California 92121

(Received 19 November 1998; accepted 21 January 1999)

A three-dimensional magnetohydrodynamic model of the global solar corona is described. The model uses observed photospheric magnetic fields as a boundary condition. A version of the model with a polytropic energy equation is used to interpret solar observations, including eclipse images of the corona, Ulysses spacecraft measurements of the interplanetary magnetic field, and coronal hole boundaries from Kitt Peak He 10 830 Å maps and extreme ultraviolet images from the Solar Heliospheric Observatory. Observed magnetic fields are used as a boundary condition to model the evolution of the solar corona during the period February 1997–March 1998. A model with an improved energy equation and Alfvén waves that is better able to model the solar wind is also presented. © *1999 American Institute of Physics.* [S1070-664X(99)94805-X]

I. INTRODUCTION

The sophistication of models of the solar corona has increased considerably since the idealized models of the 1980's (e.g., see Mikić[1] and Low[2] for examples of early models). This has been brought about by a confluence of three key elements. First, the collection of high-resolution observations of the Sun, both in space and time, has grown tremendously. For example, consider the changes in our perception of the Sun brought about by Yohkoh[3] images of the x-ray Sun; Ulysses measurements of the polar solar wind;[4] high-resolution white-light movies of solar granulation; high-resolution vector magnetographs of active regions;[5] Solar Heliospheric Observatory (SOHO) high-resolution images of the photospheric magnetic field, white-light coronagraph, and extreme ultraviolet (EUV) images of the corona, and energetic particle and solar wind composition measurements. The space-based observations are nicely complemented by an extensive archive of ground-based observations [in particular, magnetic field measurements at Kitt Peak National Solar Observatory (NSOKP) and Wilcox Solar Observatory (WSO); He 10 830 Å observations of coronal hole boundaries at NSOKP; Mauna Loa coronagraph images; and interplanetary scintillation (IPS) measurements]. Second, the power and availability of supercomputers has made two- and three-dimensional modeling routine; the increase in computing power that massive parallelism promises will extend the possibilities for realistic modeling even further. Third, the sophistication of the models themselves, both in their geometrical realism and the physics that has been included, has matured significantly.

The application of magnetohydrodynamic (MHD) coronal models to these solar observations has begun to exploit this confluence of capabilities. It is now possible to make direct comparisons between observations and models of the solar corona, as illustrated below. The development of this modeling capability is especially timely, since the observations from present missions [including the recently launched transition-region and coronal explorer (TRACE) mission] and coming missions [Solar-B, set for launch in 2004, will provide high-resolution measurements of vector magnetic fields, x-ray, and EUV emission in active regions; the Solar-Terrestrial Relations Observatory (STEREO) will take coronal images from multiple viewpoints; and Solar Probe will explore the inner solar corona] have challenged our understanding of the Sun.

To fully exploit the available data it is necessary to apply sophisticated models that use observational data as inputs and that produce observable quantities as outputs. Through this interplay of observations and theory we can improve our understanding of the Sun and heliosphere. In this paper we show examples of how large-scale models of the solar corona can be used to make detailed comparisons with observations.

II. POLYTROPIC MHD MODEL

A self-consistent description of the large-scale solar corona requires the coupled interaction of magnetic, plasma, and solar gravity forces, including the effect of the solar wind. For simplicity we first describe a "polytropic model," in which an adiabatic energy equation with a reduced polytropic index γ (i.e., smaller than 5/3) is used.[6] This is a crude way of modeling the complicated thermodynamics in the corona with a simple energy equation. The primary motivation for using a reduced γ is the fact that the temperature in the corona does not vary substantially (the limit $\gamma \to 1$ corresponds to an isothermal plasma). A typical choice, used here, is $\gamma = 1.05$. Detailed comparisons of our results with coronal observations indicate that while this model matches many features of the corona (as shown below), it is not accurate enough to quantitatively reproduce the properties of the corona and solar wind. In particular, this simple model fails to reproduce the fast (~800 km/s) and slow (~400 km/s) solar wind streams[4] that are measured at Earth, nor does it reproduce the contrast in density and temperature that is observed

*Paper D2I2.4 Bull. Am. Phys. Soc. 43, 1700 (1998).
†Invited speaker.

between streamers and coronal holes. An improved model that does not suffer from these limitations is presented in Sec. IV.

Theoretical arguments indicate that magnetic reconnection is crucial to describe the structure and dynamics of the solar corona.[7–9] Yohkoh observations also present strong evidence for the importance of magnetic reconnection.[10] We therefore include the effect of plasma resistivity (with the important caveat that numerical models require the resistivity to be enhanced compared to coronal values[11]). In the resistive MHD model, the coronal plasma is described by the following equations:

$$\nabla\times\mathbf{B}=\frac{4\pi}{c}\mathbf{J}, \tag{1}$$

$$\nabla\times\mathbf{E}=-\frac{1}{c}\frac{\partial\mathbf{B}}{\partial t}, \tag{2}$$

$$\mathbf{E}+\frac{1}{c}\mathbf{v}\times\mathbf{B}=\eta\mathbf{J}, \tag{3}$$

$$\frac{\partial\rho}{\partial t}+\nabla\cdot(\rho\mathbf{v})=0, \tag{4}$$

$$\rho\left(\frac{\partial\mathbf{v}}{\partial t}+\mathbf{v}\cdot\nabla\mathbf{v}\right)=\frac{1}{c}\mathbf{J}\times\mathbf{B}-\nabla p-\nabla p_w+\rho\mathbf{g}+\nabla\cdot(\nu\rho\nabla\mathbf{v}), \tag{5}$$

$$\frac{\partial p}{\partial t}+\nabla\cdot(p\mathbf{v})=(\gamma-1)(-p\nabla\cdot\mathbf{v}+S), \tag{6}$$

where $\mathbf{B}$ is the magnetic field, $\mathbf{J}$ is the electric current density, $\mathbf{E}$ is the electric field, ρ, $\mathbf{v}$, p, and T are the plasma mass density, velocity, pressure, and temperature, and the wave pressure p_w represents the acceleration due to Alfvén waves (see Sec. IV). The gravitational acceleration is $\mathbf{g}=-g_0\hat{\mathbf{r}}/r^2$, η is the resistivity, ν is the kinematic viscosity, and S represents energy source terms. The plasma pressure is $p=(n_e+n_p)kT$, where n_e and n_p are the electron and proton densities; for a hydrogen plasma, $n_e=n_p$. The polytropic model is defined by setting $\gamma=1.05$ and $S=0$ in Eq. (6), and zero Alfvén wave pressure in Eq. (5), $p_w=0$.

We have developed a three-dimensional code (3D)[11,12] to solve the MHD equations (1)–(6) in spherical coordinates (r,θ,ϕ). This code has been used extensively to model the 2D and 3D corona, including the structure of helmet streamers,[13–15] coronal mass ejections,[11,16–19] and the long-term evolution of the solar corona and heliospheric current sheet (see Sec. III). Related methods have been developed by Usmanov[20,21] and Pisanko.[22] The following boundary conditions are used.[14,17,19] The radial magnetic field B_r is specified at the solar surface $r=R_s$ (e.g., from synoptic magnetic field observations at NSOKP and WSO, or from full-disk magnetograms). This field may evolve in time (see Sec. III). The boundary conditions on the velocity are determined from the characteristic equations along $\mathbf{B}$. The plasma pressure, as well as the plasma density in regions where the radial velocity is positive, are specified at $r=R_s$. (In the calculations presented here, the boundary values of p and ρ were chosen to be uniform.) Characteristic equations are also used at the upper radial boundary, which is placed beyond the sonic and Alfvén points (typically at $r=30R_s$, although we have performed simulations that have included Earth's orbit in the domain,[19] and beyond).

Typical parameters for the quiet corona[23] yield a value for the Lundquist number of $S\sim10^{13}$. Since it is not possible to perform well-resolved numerical computations[11] at this large value of S, we must content ourselves with calculations at lower, but still substantial, values of $S\sim10^3-10^4$. We also use finite viscosity ν corresponding to a viscous diffusion time $\tau_\nu\sim10^2\div10^3\tau_A$, where $\tau_\nu=R_s^2/\nu$, $\tau_A=R_s/v_A$ is the Alfvén transit time, and v_A is the Alfvén speed. At the lower values of S used in the simulations we expect that the static current sheets in the solution (e.g., the heliospheric current sheet) will form in approximately the correct location, but will be broader than those in the corona.

Pneuman and Kopp[24] developed the first 2D model of helmet streamer equilibria by solving the steady-state MHD equations. Our approach, and that used in many other calculations, is to integrate the time-dependent MHD equations to steady state.[25–29] The following initial condition is used. For the given B_r distribution at $r=R_s$, a potential magnetic field ($\nabla\times\mathbf{B}=0$) is calculated in the corona, and a transonic spherically symmetric wind solution[6] is used to specify p, ρ, and $\mathbf{v}$. The MHD equations are integrated in time until the plasma and magnetic fields settle into equilibrium. The final state has closed magnetic field regions (helmet streamers), where the solar wind plasma is trapped, surrounded by open fields (coronal holes), where the solar wind flows freely along magnetic field lines, accelerating to supersonic speeds. This model has also been used to study dynamic events in the corona, including coronal mass ejections (CMEs);[11,16–19] this aspect will not be addressed in the present paper.

A. Comparison with eclipse images

Total solar eclipses offer an excellent opportunity to observe coronal streamers. The white-light polarized brightness of the corona that can be measured during an eclipse can be simulated from our MHD solution by integrating the electron density along the line of sight in the plane of the sky (convolved with a scattering function[30] and filtered with a radially graded filter to mimic the effect of instrument "vignetting"). Our first attempt to model the corona[13,14] was performed subsequent to the eclipse of 3 November 1994, observed in Chile. Since then, we have made three *predictions*, before the actual eclipse date, using magnetic field data from the previous solar rotation, for the eclipses of 25 October 1995,[19] seen in Vietnam and India; 9 March 1997, seen in Siberia, China, and Mongolia; and 26 February 1998, seen in the Caribbean. These predictions were published on the World Wide Web prior to the eclipses. We used NSOKP and WSO synoptic magnetic field maps for the calculations. The comparison of simulated polarization brightness with eclipse images is shown in Fig. 1. Comparisons with Mauna Loa MK3 coronagraph observations on several days during the solar rotations surrounding the eclipses have confirmed that the basic large-scale three-dimensional structure of the streamer belt has been captured in the model. The agreement between the model and the eclipse images is quite good,

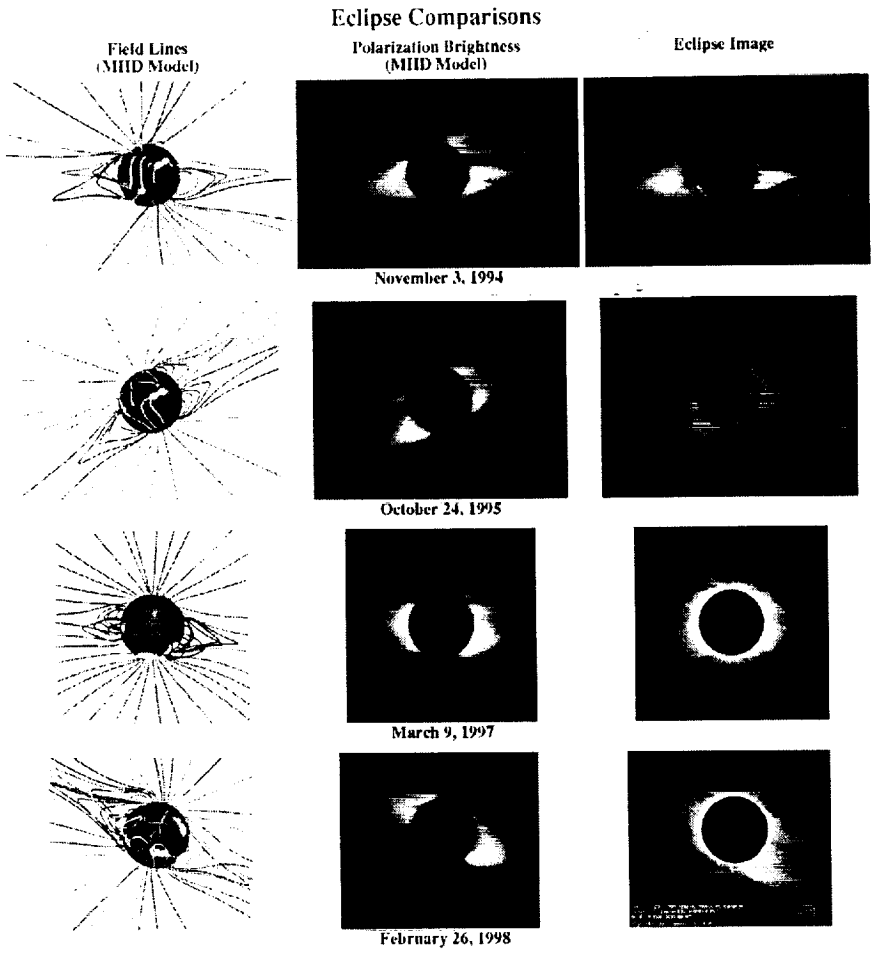

FIG. 1. Comparison of MHD computations of the solar corona with total solar eclipse observations. The 3 November 1994 eclipse was modeled subsequent to the eclipse; the other three calculations were predictions, performed in advance of the eclipse date, using magnetic field data from NSOKP and WSO. All the images are shown with geocentric north up, except for the 1997 eclipse, which has solar north up. (The sources of the eclipse images are listed in the Acknowledgments section.)

especially considering that three of the cases are predictions. Note, however, that these eclipses occurred close to solar minimum, when the large-scale structure of the Sun changes slowly between solar rotations. We are planning to predict the state of the corona during the forthcoming total solar eclipse in August 1999, which will be seen in central and eastern Europe, the Middle East, and western Asia. This prediction will be our most challenging yet, since this eclipse will occur close to solar maximum, when the structure of the corona is expected to be considerably more complicated, and changing more rapidly, than for the cases we have simulated previously.

B. Comparison with Ulysses measurements

The coronal magnetic field not only defines the structure of the solar corona, but the position of the heliospheric current sheet (HCS), and the regions of fast and slow solar wind as well. Understanding how the Sun influences the structure of the inner heliosphere requires an accurate mapping of the photospheric magnetic field into the corona and beyond. Source–surface models[31–38] provide predictions of the structure of the magnetic field in the corona and heliosphere. Source–surface models are relatively simple to apply, and have yielded important insights into the structure of the heliosphere, but a number of aspects of the Ulysses data are not described well by these models.[39–41] In particular, the latitudinal profile of the radial magnetic field and the extent of the HCS predicted by source–surface models show significant discrepancies from Ulysses observations. During May–June 1993 the Ulysses spacecraft, which was located at 30 °S latitude, ceased to observe sector boundary (i.e., HCS) crossings.[39] The "classic" Wilcox source–surface model[34,35] predicted that Ulysses would cross the heliospheric current sheet, whereas the MHD simulation correctly predicted no crossing.[13,19] The radial magnetic field from the MHD computation shows little latitudinal variation, consistent with Ulysses observations, in contrast to the source–surface model result. This agreement with Ulysses data indi-

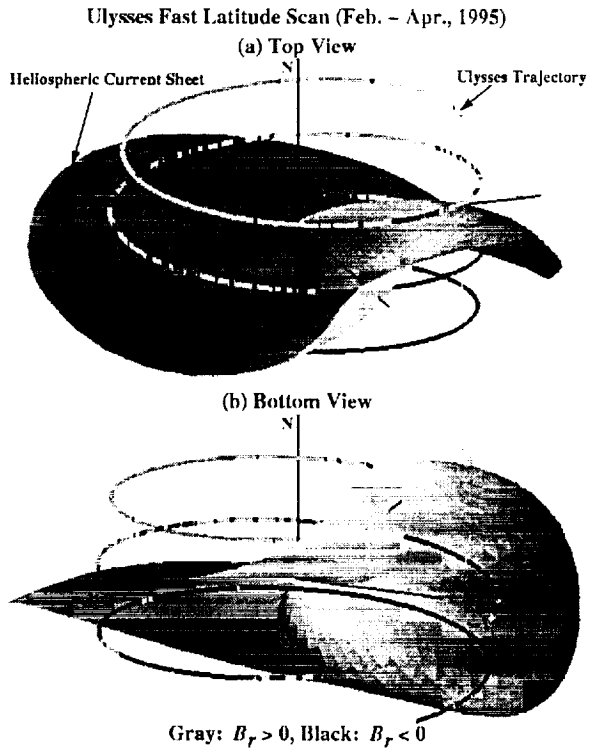

FIG. 2. Heliospheric current sheet for Carrington rotation 1892 and the Ulysses trajectory (February–April, 1995), in the rotating frame of the Sun. The color of the trajectory indicates the polarity of the magnetic field, as measured by Ulysses. Two views of the HCS are shown, (a) from above the HCS, and (b) from below the HCS. The large-scale polarity of the magnetic field is consistent with that predicted by the MHD model (positive above the HCS, negative below); the short-scale differences may be due to Alfvén waves and to structures that have not been included in the limited-resolution calculation. The MHD calculation was performed up to 400 solar radii. Ulysses was at a distance of ~1.4 astronomical units (AU) from the Sun at this time.

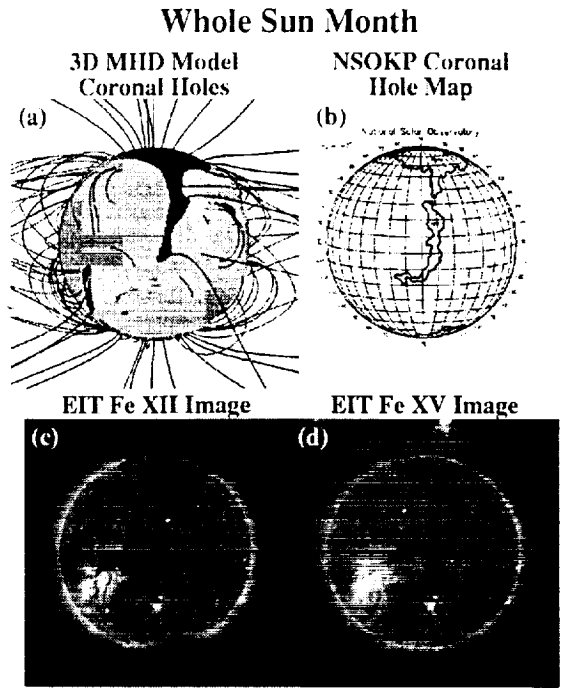

FIG. 3. Comparison of the MHD model with coronal holes seen in disk measurements on 27 August 1996. The "elephant's trunk" coronal hole (extending from the north pole past the equator) can be seen in both the simulation and the data. The NSOKP coronal hole map is deduced from He 10 830 Å images. The SOHO/EIT images are in EUV wavelengths.

cates that MHD computations may provide a better way of mapping phenomena in the solar wind back to their origin in the solar corona.

The Ulysses fast latitude scan (February–April, 1995) was a time period during which the Ulysses spacecraft traversed rapidly from southern polar latitudes of the Sun to northern polar latitudes, and offers another opportunity to test the MHD model.[19] Figure 2 shows that the HCS structure predicted by the MHD model generally matches Ulysses measurements of the magnetic field polarity. A more detailed analysis of the HCS crossings[19] shows consistency between the measurements and the model. We also used the MHD model (by tracing magnetic field lines back to the Sun, in conjunction with ballistic mapping in the region outside the computation) to deduce the solar origin of plasma observed at Ulysses. The results suggest that the fast solar wind generally comes from deeper within coronal holes than does the slow wind.[42]

C. Whole Sun Month comparison

MHD modeling is particularly useful for studying the solar corona and solar wind when a coordinated set of observations is available, since it can help to synthesize different measurements into a coherent picture. The Whole Sun Month campaign (WSM; 10 August–8 September, 1996) brought together a wide range of space and ground-based observations during solar minimum. Our MHD model was used to interpret coronagraph and EUV images,[15,43] interplanetary scintillation measurements of the solar wind speed,[44] and the structure of corotating interaction regions (CIRs) as deduced from energetic particle measurements.[45]

The "elephant's trunk" coronal hole, an equatorial extension of the northern polar coronal hole, named on account of its shape, was perhaps the most conspicuous coronal feature observed during WSM, and was apparent in several different wavelengths, including SOHO Extreme Ultraviolet Imaging Telescope (EIT) images, NSOKP He 10 830 Å maps, and Yohkoh soft x rays. It was most visible around 26–27 August 1996. Figure 3 shows tracings of the magnetic field from the MHD model as they would appear on 27 August 1996, with coronal holes (i.e., regions with open field lines, colored black) and closed-field regions (gray) mapped on the surface of the Sun. For comparison, NSOKP coronal hole boundaries and SOHO/EIT EUV images are also shown. It is apparent that the MHD model reproduces the elephant's trunk coronal hole,[15] although the observations show that the coronal hole extends to lower latitudes than predicted by the model.

We also investigated the solar origins of features observed by the Ulysses and Wind[46] spacecraft during WSM. The slow solar wind maps back close to coronal hole bound-

aries, while the fast wind typically comes from deeper within coronal holes, a pattern similar to that seen during the Ulysses fast latitude scan (Sec. II B). The model also predicts HCS crossings by Wind (but not by Ulysses) during the WSM time period.[15] Wind HCS crossings similar to those predicted were in fact observed.

III. MODELING CORONAL EVOLUTION

In the previous section we used our model to find steady-state coronal solutions for a given distribution of photospheric magnetic field. This approach is limited to the study of the long-time properties of the solar corona. In reality, even if we neglect large-scale eruptions like coronal mass ejections, the corona is changing continuously, even during times of solar minimum. This changing structure is driven by changes in the photospheric magnetic field; active regions emerge and disperse continuously during the solar cycle. We have extended our model to incorporate the evolution of the photospheric magnetic field, so that we can now follow the evolution of the corona. This gives us the capability to study the long-term evolution of the corona (as shown below), the detailed evolution during a time period of interest (e.g., during Whole Sun Month), as well as the ability to study theoretically the coronal consequences of changes in photospheric magnetic flux.

When we seek steady-state solutions of Eqs. (1)–(6), we set the tangential component of the electric field at the boundary, $\mathbf{E}_{t_0}$, to zero. This keeps B_{r_0} (B_r at $r=R_s$) fixed in time. To make the flux evolve to match observed changes, it is necessary to specify a nonzero $\mathbf{E}_{t_0}$. In general, $\mathbf{E}_{t_0}$ can be expressed as $\nabla_t\times\Psi\hat{\mathbf{r}}+\nabla_t\Phi$, where Ψ and Φ are arbitrary functions (of θ and ϕ) and ∇_t indicates tangential derivatives (in the θ-ϕ plane at $r=R_s$). The potential Φ changes $\mathbf{E}_{t_0}$ without changing the flux B_{r0}, and can be used to control the transverse magnetic field (i.e., the shear and the normal electric current), whereas the potential Ψ changes the flux. Since line-of-sight magnetograms do not provide information about the transverse component of the magnetic field, we only consider the case $\Phi=0$ here. Note that a nonzero Φ can be used to introduce shear into the field[18] and to match vector magnetic field measurements.[47] The potential Ψ is obtained by solving the equation $c\nabla_t^2\Psi=\partial B_{r_0}/\partial t$. Therefore, Ψ is evaluated as new solar magnetic field measurements become available, specifying the evolution of $\mathbf{E}_{t_0}$, which is used as a boundary condition for the MHD equations.

Thus, rather than computing a sequence of steady-state solutions for each set of magnetic field boundary values, our time-dependent MHD model now represents the actual state of the corona corresponding to the evolving magnetic field measured on the surface of the Sun. We have used a sequence of synoptic Kitt Peak magnetic field observations to study the evolution of the corona during the period 1 February 1997–18 March 1998 (14 Carrington rotations). This time interval covers the beginning of the new solar cycle, as the Sun emerges from solar minimum, and includes the emergence of high-latitude active regions. To model the evolution over a time interval of over a year is computationally prohibitive at present. In order to study the quasistatic evolution of the corona, we changed the photospheric magnetic field at a rate that was enhanced by approximately ten times compared to real time.[48] This approximation makes it impossible to study the detailed evolution of individual events, though it is still meaningful to study the quasistatic evolution of the large-scale structure of the corona. Figure 4 shows the evolution of the streamer structure, the coronal hole boundaries, and the heliospheric current sheet during this time period. Note the increase in complexity of the coronal magnetic field as the Sun emerges from solar minimum. The output of this model can easily be compared with coronal observations, as was demonstrated in Sec. II.

IV. IMPROVED MHD MODEL

Detailed comparisons of our model with observations, such as those presented in Sec. II, have forced us to confront the limitations of the polytropic MHD model. While the polytropic model matches many features of the corona, it does not reproduce the properties of the fast and slow solar wind or the large contrast in density and temperature between streamers and coronal holes. We have improved the model by including the physical mechanisms that describe the transport of energy in the corona and solar wind. One-dimensional models have been quite successful, despite their obvious geometrical limitations, in describing this interaction.[49,50] We have improved the energy equation in our model to include the effects of parallel thermal conduction, radiation loss, and parameterized coronal heating, and we have included a self-consistent model for Alfvén wave acceleration. The source term in the energy equation (6) is given by

$$S=-\nabla\cdot\mathbf{q}-n_e n_p Q(T)+H_{\rm ch}+H_d+D, \tag{7}$$

where $H_{\rm ch}$ is the coronal heating source, D is the Alfvén wave dissipation term, $H_d=\eta J^2+\nu\nabla\mathbf{v}:\nabla\mathbf{v}$ represents heating due to viscous and resistive dissipation, and $Q(T)$ is the radiation loss function.[51] In the collisional regime (below $\sim 10R_s$), the heat flux is $\mathbf{q}=-\kappa_{\parallel}\hat{\mathbf{b}}\hat{\mathbf{b}}\cdot\nabla T$, where $\hat{\mathbf{b}}$ is the unit vector along $\mathbf{B}$, and $\kappa_{\parallel}=9\times10^7T^{5/2}$ is the Spitzer value of the parallel thermal conductivity. The polytropic index γ now becomes the ratio of specific heats, $\gamma=5/3$. In the collisionless regime (beyond $\sim 10R_s$), the heat flux is modeled by $\mathbf{q}=\alpha n_e kT\mathbf{v}$, where α is a parameter.[52] Since it is presently not known in detail what heats the solar corona,[9] the coronal heating source $H_{\rm ch}$ is a parameterized function. A typical form is

$$H_{\rm ch}=H_0(\theta)\exp[-(r-R_s)/\lambda(\theta)], \tag{8}$$

where $H_0(\theta)$ expresses the latitudinal variation of the volumetric heating, and $\lambda(\theta)$ expresses the latitudinal variation of the scale length. [In practice, the variation can be expressed in terms of the magnetic topology (i.e., a proxy for the open and closed field regions) rather than the latitude θ.]

Since the acceleration of the solar wind by Alfvén waves occurs on spatial and time scales that are below the resolu-

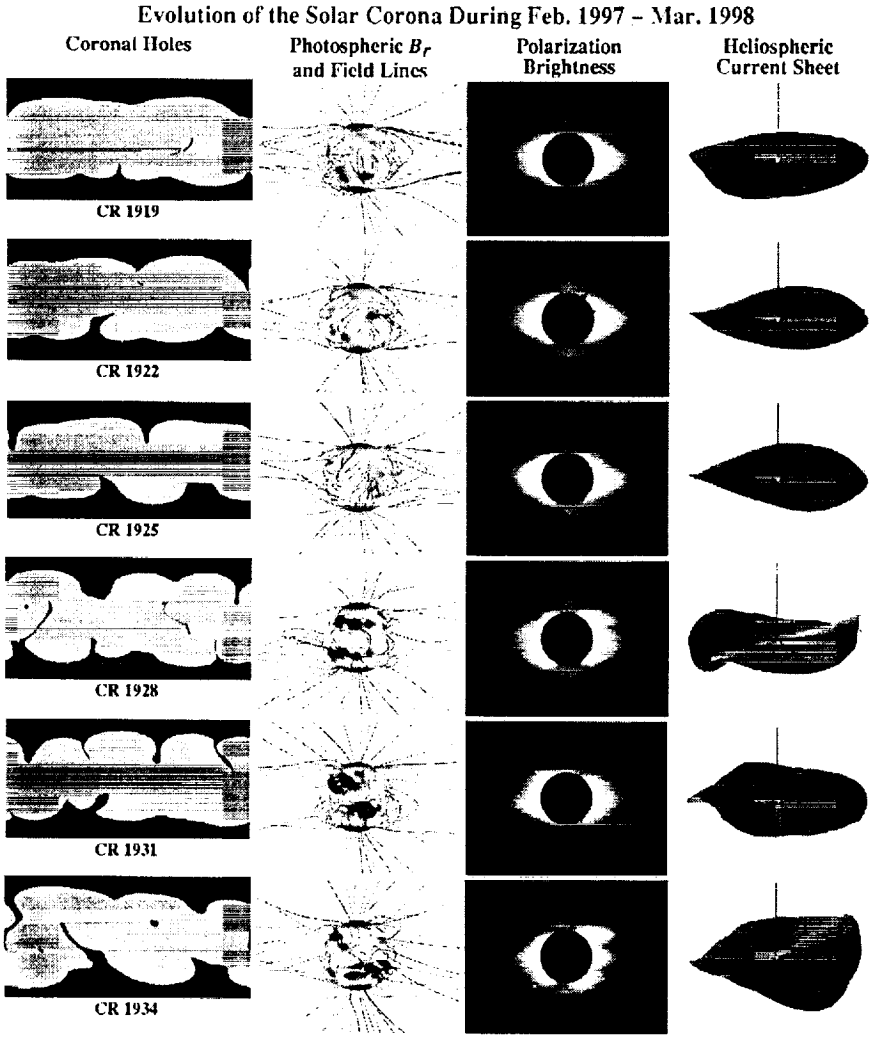

FIG. 4. The changing structure of the solar corona during the period February 1997–March 1998, Carrington rotations (CR) 1919–1934, as illustrated by coronal hole maps (longitude vs latitude, with gray/black indicating closed/open field regions), field line traces with the radial magnetic field shown on the surface of the Sun, polarization brightness, and the shape of the heliospheric current sheet. The HCS is shown up to 30 solar radii. The photospheric magnetic field was set as a time-dependent boundary condition on the 3D MHD simulation using NSOKP synoptic maps.

tion of our global numerical model, the wave pressure p_w is evolved using a WKB approximation[53] for the time-space averaged Alfvén wave energy density ϵ:

$$\frac{\partial \epsilon}{\partial t} + \nabla \cdot \mathbf{F} = \mathbf{v} \cdot \nabla p_w - D, \tag{9}$$

where $\mathbf{F} = (3/2\mathbf{v} + \mathbf{v}_A)\epsilon$ is the Alfvén wave energy flux, $v_A = B/\sqrt{4\pi\rho}$ is the Alfvén speed, and $p_w = \epsilon/2$. The Alfvén wave velocity is $\mathbf{v}_A = \pm \hat{\mathbf{b}} v_A$; in a multidimensional implementation, it is necessary to transport two Alfvén wave fields (waves parallel and antiparallel to $\mathbf{B}$), which are combined to give ϵ. The Alfvén wave energy density ϵ is related to the space-time average of the fluctuating component of the magnetic field δB by $\epsilon = \langle \delta B^2 \rangle / 4\pi$. The dissipation term D expresses the nonlinear dissipation of Alfvén waves in interplanetary space and is modeled phenomenologically.[52]

The boundary $r = R_s$ is now chosen to be at the top of the transition region, at a given temperature (say $T_0 = 500\,000$ K). The density at $r = R_s$ is determined by balancing radiation loss, thermal conduction, and heating within the chromosphere and transition region.[49] In this formulation, the only boundary conditions required from observations are on the radial magnetic field. Instead of specifying a nonuniform temperature at the coronal base to express the observed variation of temperature between streamers and coronal holes, as would be required in the polytropic model, we now specify the distribution of coronal heating. By investigating how MHD solutions compare with observations it will be possible to test different coronal heating models, and, eventually, when the coronal heating process is better understood, to relate the heating source to physical quantities.

This formulation has been applied to a 2D (axisymmet-

ric) model of the corona. Extensive tests show that a nonuniform heating profile, together with Alfvén waves, can reproduce the speed, mass flux, density, and temperature of the fast and slow solar wind at Earth. The coronal density contrast is much improved compared to the polytropic model: coronal streamers are 5–10 times denser than coronal holes. The model is presently being extended to 3D.

V. CONCLUSION

The last decade has seen a marked increase in the sophistication of models of the solar corona. Present models have improved geometrical realism, improved physics, are able to use solar observations directly as boundary conditions on the calculations (e.g., measured photospheric magnetic field), and can model the evolving solar corona. We have presented comparisons between a 3D MHD model and observations of coronal and heliospheric structure. The agreement between simulated coronal structure and observations is encouraging, implying that the models are mature enough for detailed analysis. Such 3D models will undoubtedly find increased use in interpreting solar observations and developing up-to-date models of the solar corona. Yet it must be recognized that we have only begun to "scratch the surface" of what is possible. Despite these advances, some of the fundamental theoretical questions in solar physics remain unsolved [e.g., what initiates CMEs and flares; what is the relationship between CMEs and flares; how do coronal magnetic structures emerge, evolve, and erupt; what heats the solar corona?]. Continued comparisons of model predictions and observations will help to answer these key questions and provide new insights into the physics of the corona.

ACKNOWLEDGMENTS

The authors thank Dr. Jack Harvey (NSOKP) and Dr. Todd Hoeksema (WSO) for kindly providing us with up-to-date magnetic field data for our eclipse predictions. Kitt Peak synoptic magnetic charts and coronal hole maps are courtesy of NSOKP, which is funded cooperatively by the National Science Foundation (NSF)/National Optical Astronomy Observatories (NOAO), the National Aeronautics and Space Administration (NASA)/Goddard Space Flight Center (GSFC), and the National Oceanic and Atmospheric Administration (NOAA)/Space Environment Center (SEC). EIT data are courtesy of the SOHO EIT consortium. SOHO is a project of international cooperation between NASA and the European Space Agency (ESA). Ulysses magnetic field data were obtained from the National Space Science Data Center. The 1994 and 1998 eclipse images are courtesy of the High Altitude Observatory, National Center for Atmospheric Research (NCAR) Boulder, CO. NCAR is sponsored by NSF. The 1995 eclipse image is courtesy of F. Diego and S. Koutchmy. The 1997 eclipse image is courtesy of Dr. E. Hiei of Meisei University and the National Astronomical Observatory of Japan. This research was supported by NASA Space Physics Theory Program Contract No. NAS5-96081, NASA Supporting Research and Technology Contract Nos. NASW-5017, NASW-4968, and NASW-98030, and NSF Grant Nos. ATM-9320575, ATM-9319517, and AMT-9613834. Computational facilities were provided by the U.S. Department of Energy at the National Energy Research Supercomputer Center and by NSF at the San Diego Supercomputer Center.

[1] Z. Mikić, Phys. Fluids B **2**, 1450 (1990).
[2] B. C. Low, Annu. Rev. Astron. Astrophys. **28**, 491 (1990).
[3] L. Acton, S. Tsuneta, Y. Ogawara, R. Bentley, M. Bruner, R. Canfield, L. Culhane, G. Doschek, E. Hiei, and T. Hirayama, Science **258**, 618 (1992).
[4] D. J. McComas, S. J. Bame, B. L. Barraclough, W. C. Feldman, H. O. Funsten, J. T. Gosling, P. Riley, R. Skoug, A. Balogh, R. Forsyth, B. E. Goldstein, and M. Neugebauer, Geophys. Res. Lett. **25**, 1 (1998).
[5] B. W. Lites, B. C. Low, V. Martínez Pillet, P. Seagraves, A. Skumanich, Z. A. Frank, R. A. Shine, and S. Tsuneta, Astrophys. J. **446**, 877 (1995).
[6] E. N. Parker, *Interplanetary Dynamical Processes* (Wiley, New York, 1963).
[7] E. R. Priest, *Solar Magnetohydrodynamics* (Reidel, Dordrecht, 1982).
[8] E. N. Parker, *Cosmical Magnetic Fields* (Clarendon, Oxford, 1979).
[9] E. N. Parker, *Spontaneous Current Sheets in Magnetic Fields* (Oxford, New York, 1994).
[10] S. Tsuneta, Astrophys. J. **456**, 840 (1996).
[11] Z. Mikić and J. A. Linker, Astrophys. J. **430**, 898 (1994).
[12] The numerical techniques used are similar to those described for a cylindrical code by R. Lionello, Z. Mikić, and D. D. Schnack, J. Comput. Phys. **140**, 172 (1998).
[13] Z. Mikić and J. A. Linker, *Solar Wind Eight: Proceedings of the Eight International Solar Wind Conference*, edited by D. Winterhalter, J. T. Gosling, S. R. Habbal, W. S. Kurth, and M. Neugebauer (American Institute of Physics, Woodbury, NY, 1996), Conf. Proc. Vol. 382, p. 104.
[14] J. A. Linker, Z. Mikić, and D. D. Schnack, *Solar Drivers of Interplanetary and Terrestrial Disturbances*, edited by K. S. Balasubramaniam, S. L. Keil, and R. N. Smartt (Astronomical Society of the Pacific, 1996), Conf. Series Vol. 95, p. 208.
[15] J. A. Linker, Z. Mikić, D. A. Biesecker, R. J. Forsyth, S. E. Gibson, A. J. Lazarus, A. Lecinski, P. Riley, A. Szabo, and B. J. Thompson, "Magnetohydrodynamic modeling of the solar corona during Whole Sun Month," J. Geophys. Res. (in press).
[16] J. A. Linker, Z. Mikić, and D. D. Schnack, *Proceedings of the Third SOHO Workshop—Solar Dynamic Phenomena and Solar Wind Consequences*, Estes Park, CO (European Space Agency, Paris, 1994), SP-373, p. 249.
[17] J. A. Linker and Z. Mikić, Astrophys. J. **438**, L45 (1995).
[18] Z. Mikić and J. A. Linker, *Coronal Mass Ejections*, edited by N. Crooker, J. Joselyn, and J. Feynman (American Geophysical Union, Washington DC, 1997), Geophys. Monograph 99, p. 57.
[19] J. A. Linker and Z. Mikić, *Coronal Mass Ejections*, edited by N. Crooker, J. Joselyn, and J. Feynman (American Geophysical Union, Washington DC, 1997), Geophys. Monograph 99, p. 269.
[20] A. V. Usmanov, *Solar Wind Eight: Proceedings of the Eight International Solar Wind Conference*, edited by D. Winterhalter, J. T. Gosling, S. R. Habbal, W. S. Kurth, and M. Neugebauer (American Institute of Physics, Woodbury, NY, 1996), Conf. Proc. Vol. 382, p. 141.
[21] A. V. Usmanov, B. P. Besser, J. M. Fritzer, and M. L. Goldstein, "Two-dimensional MHD simulation of the solar corona with WKB Alfvén waves," J. Geophys. Res. (submitted).
[22] Y. V. Pisanko, "A composite MHD model of an expanding corona and its application to the Whole Sun Month campaign," J. Geophys. Res. (submitted).
[23] E. N. Parker, Astrophys. J. **264**, 642 (1983).
[24] G. W. Pneuman and R. A. Kopp, Sol. Phys. **18**, 258 (1971).
[25] F. Endler, Ph.D. thesis, Gottingen University, 1971.
[26] R. S. Steinolfson, S. T. Suess, and S. T. Wu, Astrophys. J. **255**, 730 (1982).
[27] H. Washimi, Y. Yoshino, and T. Ogino, Geophys. Res. Lett. **14**, 487 (1987).
[28] J. A. Linker, G. Van Hoven, and D. D. Schnack, Geophys. Res. Lett. **17**, 2281 (1990).
[29] A. H. Wang, S. T. Wu, S. T. Suess, and G. Poletto, Sol. Phys. **147**, 55 (1993).
[30] D. E. Billings, *A Guide to the Solar Corona* (Academic, New York, 1966).
[31] K. H. Schatten, J. M. Wilcox, and N. Ness, Sol. Phys. **6**, 442 (1969).
[32] M. D. Altschuler and G. Newkirk, Sol. Phys. **9**, 131 (1969).
[33] K. H. Schatten, Cosmic Electrodyn. **2**, 232 (1971).

[34]J. T. Hoeksema, J. M. Wilcox, and P. H. Scherrer, J. Geophys. Res. **88**, 9910 (1983).
[35]J. T. Hoeksema, Adv. Space Res. **9**, 141 (1989).
[36]Y.-M. Wang and N. R. Sheeley, Jr., Astrophys. J. **392**, 310 (1992).
[37]Y.-M. Wang and N. R. Sheeley, Jr., Astrophys. J. **447**, L143 (1995).
[38]X. Zhao and J. T. Hoeksema, J. Geophys. Res. **100**, 19 (1995).
[39]E. J. Smith, M. Neugebauer, A. Balogh, S. J. Bame, G. Erdos, R. J. Forsyth, B. E. Goldstein, J. L. Philips, and B. Tsurutani, Geophys. Res. Lett. **20**, 2327 (1993).
[40]E. J. Smith, R. G. Marsden, and D. E. Page, Science **268**, 1005 (1995).
[41]A. Balogh, E. J. Smith, B. T. Tsurutani, D. J. Southwood, R. J. Forsyth, and T. S. Horbury, Science **268**, 1007 (1995).
[42]M. Neugebauer, R. J. Forsyth, A. B. Galvin, K. L. Harvey, J. T. Hoeksema, A. J. Lazarus, R. P. Lepping, J. A. Linker, Z. Mikić, J. T. Steinberg, R. von Steiger, Y.-M. Wang, and R. Wimmer-Schweingruber, J. Geophys. Res. **103**, 14587 (1998).
[43]S. E. Gibson, D. A. Biesecker, M. Guhathakurta, J. T. Hoeksema, A. J. Lazarus, J. A. Linker, Z. Mikić, Y. Pisanko, J. T. Steinberg, B. J. Thompson, and X. P. Zhao, "The three-dimensional coronal magnetic field during Whole Sun Month," to appear in Astophys. J.
[44]A. R. Breen, Z. Mikić, J. A. Linker, A. J. Lazarus, B. J. Thompson, P. J. Moran, C. A. Varley, P. J. S. Williams, D. A. Biesecker, and A. Lecinski, "Interplanetary scintillation measurements of the solar wind during Whole Sun Month: Linking coronal and *in situ* observations," J. Geophys. Res. (in press).
[45]A. Posner, V. Bothmer, B. J. Thompson, H. Kunow, B. Heber, R. Muller-Mellin, A. J. Lazarus, A. Szabo, Z. Mikić, and J. A. Linker, "In-ecliptic CIR-associated energetic particle events and polar coronal hole structures: SOHO/COSTEP observations for the Whole Sun Month campaign," J. Geophys. Res. (in press).
[46]M. H. Acuna, K. W. Ogilvie, D. N. Baker, S. A. Curtis, D. H. Fairfield, and W. H. Mish, Space Sci. Rev. **71**, 5 (1995).
[47]Z. Mikić and A. N. McClymont, *Solar Active Region Evolution: Comparing Models with Observations*, edited by K. S. Balasubramaniam and G. W. Simon (Astronomical Society of the Pacific, 1994), Conf. Ser. Vol. 68, p. 225.
[48]This simulation took 65 h of CPU time on a single processor of the Cray-T90 supercomputer. A real-time solution would take about 10 times longer. It may be possible to perform a real-time simulation once our code is ported to a massively parallel computer.
[49]G. L. Withbroe, Astrophys. J. **325**, 442 (1988).
[50]S. R. Habbal, R. Esser, M. Guhathakurta, and R. R. Fisher, Geophys. Res. Lett. **22**, 1465 (1995).
[51]R. Rosner, W. H. Tucker, and G. S. Vaiana, Astrophys. J. **220**, 643 (1978).
[52]J. V. Hollweg, Rev. Geophys. Space Phys. **16**, 689 (1978).
[53]S. A. Jacques, Astrophys. J. **215**, 942 (1977).

THE ASTROPHYSICAL JOURNAL, 518:L57–L60, 1999 June 10

THREE-DIMENSIONAL SOLUTIONS OF MAGNETOHYDRODYNAMIC EQUATIONS FOR PROMINENCE MAGNETIC SUPPORT: TWISTED MAGNETIC FLUX ROPE

T. AMARI[1]
DSM/DAPNIA, Service d'Astrophysique, URA 2052 associée au Centre National de la Recherche Scientifique, CEA-Saclay, F-91191 Gif sur Yvette Cedex, France; amari@discovery.saclay.cea.fr
J. F. LUCIANI
Centre National de la Recherche Scientifique, Centre de Physique Théorique de l'Ecole Polytechnique, F-91128 Palaiseau Cedex, France
AND
Z. MIKIC AND J. LINKER
Science Applications International Corporation, 10260 Campus Point Drive, San Diego, CA 92121
Received 1998 November 24; accepted 1999 April 1; published 1999 April 23

ABSTRACT

The search for a background magnetic configuration favorable for prominence support has been given a great deal of attention for several decades. The most recent theoretical studies seem to agree that a promising candidate for the support of the dense and cooler prominence material, which fulfills several of the theoretical and observational requirements such as twist, shear along the neutral line, and dips, is a magnetic flux rope. The most convincing models take an infinitely long periodic configuration that consists of a linear constant-α force-free magnetic field. These models, however, assume values of α that are close to its maximum possible value. In this Letter, we report our recent results, which show that it is indeed possible to produce a configuration that consists of a twisted magnetic flux tube embedded in an overlaying, almost potential, arcade such that high electric currents (and therefore values of α) are confined to the inner twisted magnetic flux rope. We present two MHD processes—corresponding to two different types of boundary conditions—that produce such a configuration. Our results show that the process associated variations of B_z at the photospheric level by applying an electric field involving diffusion is much more efficient for creating a structure with more twist and dips.

Subject headings: MHD — stars: coronae — stars: flare — stars: magnetic fields

1. INTRODUCTION

Prominences are sheets of cold material (about hundreds of times cooler and denser than the surrounding corona) supported by magnetic forces. They may either be quiescent structures outside active regions or participants in solar eruptive phenomena, such as coronal mass ejection or flares. Prominences are seen to lie above a neutral line separating regions of opposite polarity (Priest 1982). A global self-consistent model represents a complicated task because of the strong coupling between mechanical equilibrium and energy transport. Therefore, only two uncoupled problems have generally been considered so far. In the first class of problems the magnetic field is fixed while the energy equation is solved, while in the second one the global magnetic background configuration is sought for a given simplified energy equation or even without any energy equation (looking for a configuration favorable for prominence support, assuming that the prominence material just represents a small perturbation to the configuration).

Magnetic flux ropes represent good candidates for the second class of problems and have therefore been sought. They may contain twist, shear along the neutral line (Heyvaerts & Hagyard 1991), and dips (locations of the magnetic configuration at which the concavity is favorable to prominence material accumulation). They also represent a natural way to account for the total solar (internal plus external) magnetic helicity content, which must be globally conserved and is found in the corona if *helicity is injected* from the interior of the Sun (convection zone) into the corona (Low 1994). They must also play an important role by participating in *helicity ejection* (or redistribution at "infinity"—in the solar wind) during eruptive events, via instability processes in which the flux rope is either passive (if the overlaying structure is disrupted) or active (if the flux rope is at the origin of a kink-type instability related to the amount of twist or electric current profile) (Amari, Luciani, & Mikic 1999). Indeed, prominences have been observed in several eruptive active regions (Hundhausen 1988, 1994; Leka et al. 1993).

For configurations invariant by translation along the x-axis, if one assumes the background magnetic field to be potential and the prominence to be modeled by a thin cold massive current sheet, then for various possible boundary value problems (BVPs), no magnetic island can exist in the configuration (Aly, Amari, & Colombi 1990; Ridgway, Priest, & Amari 1991a, 1991b), which excludes any flux tube–like topology. It was even possible to prove rigorously that with the same assumption of axisymmetry and symmetry against the vertical z-axis, no force-free configuration (linear or even nonlinear) that corresponds to a strictly bipolar photospheric boundary condition having a dip in the configuration can be accessible by slow quasi-static shearing motions (Amari et al. 1991), a result that actually excludes not only flux ropes or configurations having magnetic islands, but extends to a more general class. Relaxing the assumption of strictly bipolar boundary conditions in the case of a constant-α linear force-free magnetic field defined in a half-strip, it was eventually possible (Amari & Aly 1992) to build a whole class of magnetic configurations having a flux rope topology for either bipolar (but allowing parasite boundary polarities), quadrupolar, or hexapolar con-

[1] Also at Centre National de la Recherche Scientifique, Observatoire de Paris, Laboratoire de Physique Solaire et de l'Heliosphere, F-92195 Meudon Principal Cedex, France.

figurations. However, one major drawback of these models is that all these configurations are obtained for large values of α, close to the maximum permitted value ($\alpha_M = \pi/L$ if L is the width of the strip). Aulanier & Demoulin (1998) substitute periodicity for axisymmetry (x-invariant field) in our previous models to get configurations matching observed structures, but keeping the same strong limitation on the large values of α, which is unrealistically large even in the far field region.

In this Letter, we report some new results that we have obtained in revisiting this problem of building a twisted flux tube in equilibrium in an overlaying arcade as the global background magnetic configuration (above a bipolar photospheric region) for prominence support, using a three-dimensional MHD approach corresponding to two different types of boundary conditions. In the first one, purely ideal photospheric motions are applied. In the second one, we apply an electric field that corresponds to diffusion of B_z. This has been used to model the dispersion of active region flux into the network (Wang, Sheeley, & Nash 1991), and it actually appears quite reasonable to consider that in a long-term evolution of an active region, photospheric diffusion does occur (van Ballegooijen 1999). It is, however, worth noticing that none of these assumptions is indeed necessary for the rest of this Letter; these processes may be simply regarded as tools for building equilibrium configurations as the solution of MHD equations, in the same way that one could derive the equilibrium solutions in the previous models on pure analytical grounds.

The Letter is organized as follows. In § 2, we present the three-dimensional MHD evolution (buildup of shear along the neutral line) of an initially arcade-like potential magnetic configuration. In § 3, we consider an ideal MHD process that adds up twist in a second phase to build a first type of twisted flux tube configuration, while in § 4 we present a diffusive MHD process that allows us to produce flux ropes with higher twist.

2. THE BUILDUP OF SHEAR

In what follows, the corona is represented by the half-space $D = \{z > 0\}$, which is filled up with a slightly resistive and viscous plasma. For the numerical computations, D is approximated by the finite box $\{0 < x < L_x, 0 < y < L_y, 0 < z < L_z\}$, whose size is large compared to the characteristic spatial scale of the system (which is our reference length). Typically we choose $L_x = L_y = L_z = 40$–60 and provide the domain with a nonuniform mesh ($111 \times 101 \times 70$ nodes). We first start at $t = 0$ with an initial potential (i.e., current-free) arcade-like configuration such that $\boldsymbol{B}[(x, y, z); 0] = \nabla\Psi(x, y, z)$, where Ψ is the unique solution of a Dirichlet-Neuman Laplace BVP. Its normal derivative on $\{z = 0\}$ corresponds to the distribution of B_z. It is taken as two elliptic Gaussian distributions symmetrically placed across the x-axis; their centers are $(0, \pm 0.8)$, their width is ($\delta x = 1$, $\delta y = 2$), and the normalization is such that the maximum value taken for B_z is 1. On the other (lateral) boundaries, we actually impose for Ψ the value taken by the scalar potential corresponding to the unique current-free magnetic field in the whole upper half-space $\{z > 0\}$ whose distribution of B_z on $\{z = 0\}$ coincides with the normal derivative of Ψ on the finite computational box and tends to zero at infinity. With this large box and this type of boundary conditions, the initial condition in the finite computational domain D mimics an arcade-like solution in the upper half-space $\{z > 0\}$.

For $t \geq 0$, we impose a twisting velocity field to the footpoints on the bottom of the box such that the normal component $B_z(x, y, 0)$ of the field on the boundary is preserved, which, as in Amari et al. (1996a, hereafter ALAT), corresponds to two large-scale parallel vortices rotating in the same direction with a maximum velocity not greater than $v_0 = 10^{-2}$ (then v_0 is small compared to the Alfvén speed $v_A = 1$). On the other faces of the box, we take the homogeneous Dirichlet condition $\boldsymbol{v} = 0$, which is natural for a viscous plasma in contact with a nonmoving wall. This type of velocity field corresponds to high shearing motions near the neutral line (very similar to those considered in Amari et al. 1996b in the axisymmetric case), while twisting motions are introduced as one move away from the neutral line on $\{z = 0\}$.

The system is then evolved by solving the MHD equations that write in a simplified nondimensionalized form (see Amari, Luciani, & Joly 1999; ALAT):

$$\rho \frac{\partial \boldsymbol{v}}{\partial t} = -\rho(\boldsymbol{v} \cdot \nabla \boldsymbol{v}) + (\nabla \times \boldsymbol{B}) \times \boldsymbol{B} \qquad (1)$$

$$-\nabla p + \nabla \cdot (\nu \rho \nabla \boldsymbol{v}) + \rho \boldsymbol{g},$$

$$\frac{\partial \boldsymbol{B}}{\partial t} = \nabla \times (\boldsymbol{v} \times \boldsymbol{B}) - \nabla \times (\eta j), \qquad (2)$$

$$\frac{\partial \rho}{\partial t} = -\nabla(\rho \boldsymbol{v}), \qquad (3)$$

$$\frac{\partial \rho}{\partial t} = -(\boldsymbol{v} \cdot \nabla) p - \Gamma p(\nabla \cdot \boldsymbol{v}) + H, \qquad (4)$$

$$j = \nabla \times \boldsymbol{B}, \qquad (5)$$

$$\nabla \cdot \boldsymbol{B} = 0, \qquad (6)$$

where $\boldsymbol{B}$ is the magnetic field and $\boldsymbol{v}$, ρ, and ν are, respectively, the velocity, mass density, and kinematic viscosity of the plasma, while η is the plasma resistivity. Since in coronal situations β is small (of the order of 10^{-3} or even smaller), typical simulations were done with these values or with $\beta = 0$. As in ALAT, in the latter case we are thus constrained to fix arbitrarily a mass density profile and of course to neglect the gravity term in equation (1). Here, we choose $\rho = B^2$, which ensures a constant Alfvén velocity. We have also tried other different density profiles (exhibiting a slower decrease with distance), but this does not lead to any difference in the results. Small values are used for the dissipation coefficients: $\nu = 10^{-2}$ to 10^{-3} for the kinematic viscosity and $\eta = 0$ for the first sequence of runs. The calculations of the evolution of the field are performed with the code METEOSOL, which uses a implicit/semi-implicit numerical scheme (ALAT; Amari et al. 1996b). We then start shearing the initial state, using a linear ramp of $10\tau_A$ to reach a maximum velocity of 10^{-2} at $t = 10$. The photospheric twisting motions are applied up to about $t = 200$. The time step used for the time advance is chosen between 0.05 and 0.1. Thanks to our numerical scheme, this allows us to effect the simulation in a reasonable computational time.

The system evolves quasi-statically through a sequence of force-free configurations. This type of boundary velocity profile allows to us build up a large amount of shear in the configuration along the neutral line (about 70°–75°, with 90° meaning a field aligned with neutral line), as is often observed in active regions (Heyvaerts & Hagyard 1991). At $t = 200$, the boundary velocity field is progressively switched off (with a linear ramp

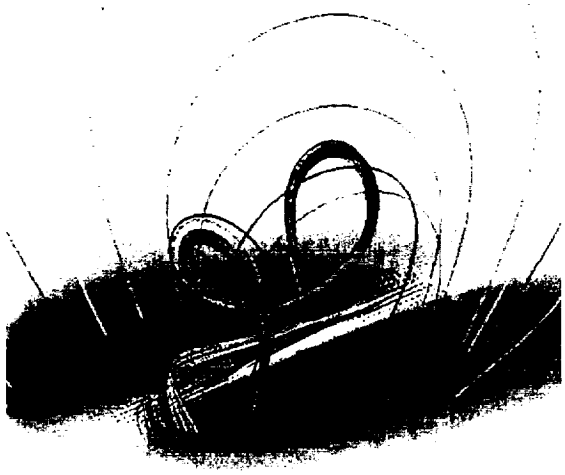

FIG. 1.—Configuration obtained at $t = 550$ after applying a localized boundary twisting vector field shown at the bottom of the figure (superposed to the photospheric image of the B_z distribution) to the equilibrium configuration obtained at the end of shear buildup (shearing motions followed by a relaxation phase) at $t = 400$.

of 10 time units) and the system is allowed to relax up to $t = 400$ to an accessible neighborhood equilibrium.

3. TWIST BUILDUP BY IDEAL MHD PHOTOSPHERIC MOTIONS

For $t \geq 400$, we now start applying a twisting boundary velocity field such that the free function ψ in equation (1) is given by two Gaussian distributions located on each side of the neutral line of this new initial configuration, as shown in Figure 1 (superposed to the photospheric image of B_z) with $v_0 = 10^{-2}$. This velocity field corresponds to two parallel vortices rotating in the same direction and located symmetrically with respect to the origin O of the plane [their center is $(\pm 1.4, \pm 0.5)$ with respect to O] and width equal to 0.4. The ramp function f, which is used to smoothly switch on or off the velocity field, is chosen to be linear. The configuration evolves through a sequence of force-free equilibria with a monotonically increasing energy. Figure 1 shows one of this intermediate equilibrium obtained at $t = 550$ after these twisting motions have been applied. We actually checked that the configuration relaxed toward an equilibrium by performing a viscous relaxation procedure (see ALAT; Amari et al. 1996b). The configuration clearly presents a twisted flux tube aligned along the neutral line and still confined by an overlaying arcade. The maximum value of $|\alpha|$ is 8.2 in our units. The concavity is directed upward in the central part of the tube, which implies (Amari et al. 1991) a configuration favorable to material support.

4. DIFFUSIVE PHOTOSPHERIC MHD PROCESS

Let us now consider again the sequence of equilibria obtained in § 3 with boundary shearing motions. Let us then apply $v_x(x, y, t) = v_y(x, y, t) = 0$ with $t_0 \in [0, 400]$ as boundary conditions for $t > t_0$ and apply a tangential electric field corresponding to diffusion of B_z on the boundary $\{z = 0\}$ only, while the domain $\{z > 0\}$ is treated ideally ($\eta = 0$). Let us take two particular cases:

1. $t_0 = 400$: In the first case, we choose as the initial state for this relaxation process the configuration obtained at the end of the process of shearing and ideal viscous relaxation considered in § 2. As shown on Figure 2 ($t = 480$), reconnection takes place on the sheared field lines (mainly along the neutral line; *left*), producing a large twisted flux tube (*right*). Although the net twist is about the same order as for the configuration obtained in § 3 (almost 3π) with an ideal process, the amount of flux from which the field lines that have the upward concavity originate is larger, leading to a much larger magnetic dip favorable for material support. Note that in the ideal MHD case considered in § 3, the twisting motions produce electric currents that tend to make the tube deviate from its axis, while we actually found that in the diffusive case the large electric currents (corresponding to $|\alpha|_{max} = 36.6$) are created by those currents originating from the highly sheared field lines and are strongly confined to the core of the twisted flux rope—along the tube axis—keeping the structure aligned with its axis.

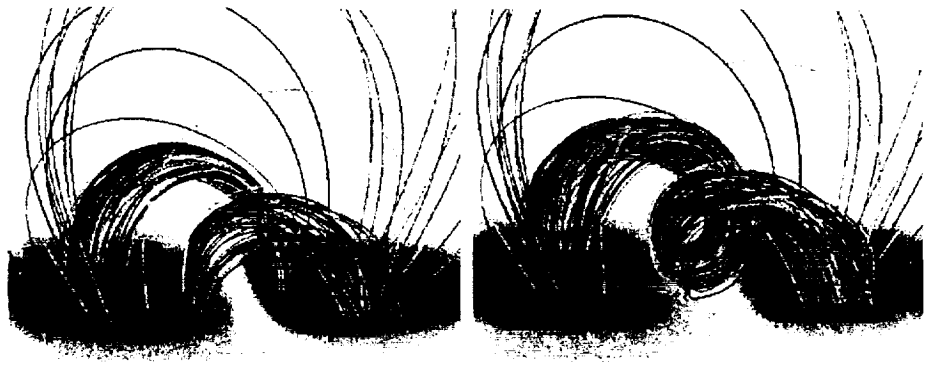

FIG. 2.—Evolution of the configuration (obtained at the end of shear buildup $t = 400$; *left*) from an arcade-like topology to a twisted flux rope–like topology (*right*), after applying an electric field corresponding to diffusive photospheric boundary conditions ($t = 480$).

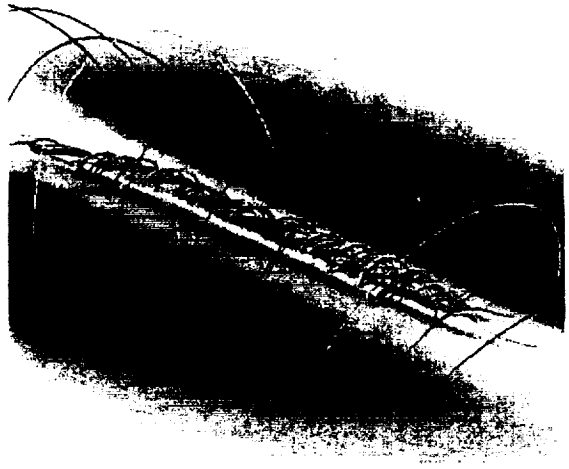

FIG. 3.—Configuration obtained at $t = 100$ by applying an electric field (corresponding to diffusive photospheric boundary conditions) to the configuration picked up at time $t = 20$ of the previous shear buildup phase. The strong electric currents confined in the core of the tube are responsible for more twist and magnetic dips than the configuration obtained with the ideal MHD fluid motions.

2. $t_0 = 20$: Let us now consider as a new initial state a configuration that is only slightly sheared. Figure 3 shows how after the same time as in case 1 a twisted flux tube aligned along the neutral line is produced. This flux rope is embedded into a confining potential arcade. The amount of twist is much larger than in case 1 (up to about 10 turns, although it is difficult to give a rigorous intrinsic definition of twist for an arbitrary three-dimensional configuration). The distribution of current (corresponding to $|\alpha|_{max} = 66.4$) is strongly nonlinear, and strong electric currents flow along the tube axis and are responsible for this higher twist and for a large number of dips in a flux rope having a smaller section than in case 1.

It appears clear that the diffusive MHD process discussed in this section is much more efficient for creating a flux rope having more dips (a bigger twist) than the purely ideal one. The configuration is confined by an overlaying arcade as is often observed in active regions. It is worth noticing that the fact that we have chosen $\eta \neq 0$ only on the boundary is not crucial.

Note that the two classes of boundary conditions may not be considered equivalent since the corresponding boundary electric fields are of fluid-type nature (for the ideal process) while purely resistive for the second class of process (the electric field cannot be written as a $\boldsymbol{v} \times \boldsymbol{b}$ fluid term, and its tangential component can be imposed a priori and depends on solar photospheric processes or the trace of the solar subphotospheric physical processes).

More various configurations (and boundary conditions) as well as their stability properties are currently under study and will be reported in a forthcoming paper. Note that our results may represent a new way for analyzing more consistent models in which more general MHD processes implying plasma effects could be taken into account in a following step.

We would like to thank A. van Ballegooijen for stimulating discussions. We wish also to thank NATO for its financial support. The numerical simulations performed in this Letter have been done on the CRAY supercomputers of the Commissariat à l'Energie Atomique and the Institut de Developpement et des Ressources en Informatique Scientifique of the Centre National de la Recherche Scientifique.

REFERENCES

Aly, J. J., Amari, T., & Colombi, P. 1990, in Solar Plasma Phenomena, ed. M. A. Dubois, F. Bely-Dubau, & D. Gresillon (Paris: Presse de L'ecole Polytechnique), 181
Amari, T., & Aly, J. J. 1992, A&A, 265, 791
Amari, T., Demoulin, P., Browning, P., Hood, A., & Priest, E. R. 1991, A&A, 241, 604
Amari, T., Luciani, J. F., Aly, J. J., & Tagger, M. 1996a, ApJ, 466, L39 (ALAT)
———. 1996b, A&A, 306, 913
Amari, T., Luciani, J. F., & Joly, P. 1999, SIAM Sci. Comput., in press
Amari, T., Luciani, J. F., & Mikic, Z. 1999, Plasma Phys. Controlled Fusion, 41, A779
Aulanier, G., & Demoulin, P. 1998, A&A, 329, 1125
Heyvaerts, J., & Hagyard, M. J. 1991, in Flares 22 Workshop, Dynamics of Solar Flares, ed. B. Schmieder & E. R. Priest (Paris: Obs. Paris), 1
Hundhausen, A. 1988, in Proc. Sixth International Solar Wind Conf., Vol. 1, ed. V. Pizzo, D. G. Sime, & T. E. Holzer (Boulder: NCAR), 181
———. 1994, Invited review talk at Current Trends in Astrophysical Magnetohydrodynamics (Boulder), unpublished
Leka, K. D., Canfield, R. C., McClymont, A. N., de La Beaujardiere, J. F., & Fan, Y. 1993, ApJ, 411, 370
Low, B. C. 1994, Phys. Plasmas, 1, 1684
Priest, E. R. 1982, Solar Magnetohydrodynamics (Dordrecht: Reidel)
Ridgway, C., Priest, E. R., & Amari, T. 1991a, ApJ, 367, 321
———. 1991b, ApJ, 385, 718
van Ballegooijen, A. A. 1999, in Magnetic Helicity in Space and Laboratory Plasmas (Geophysical Monograph Ser.; Washington: American Geophysical Union), in press
Wang, Y. M., Sheeley, N. R., & Nash, A. G. 1991, ApJ, 383, 431

Astron. Astrophys. 350, 1051–1059 (1999)

ASTRONOMY AND ASTROPHYSICS

An iterative method for the reconstruction of the solar coronal magnetic field

I. Method for regular solutions

T. Amari[1,2], T.Z Boulmezaoud[2,3], and Z. Mikic[4]

[1] CNRS URA 2052, Service d'Astrophysique CEA/Saclay, 91191 Gif sur Yvette Cedex, France
[2] CNRS, Observatoire de Paris, L.P.S.H. 92195 Meudon Principal Cedex, France
[3] Laboratoire d'Analyse Numérique, Université P.& M. Curie, 75252 Paris cedex 05 France
[4] S.A.I.C., 10260 Campus Point Drive, San Diego, CA 92121, USA

Received 17 February 1999 / Accepted 4 June 1999

Abstract. We present a method for reconstructing the coronal magnetic field, assumed to be in a non-linear force-free state, from its values given in the photosphere by vector magnetograph measurements. In this paper, that is the first of a series, we propose a method that solves the boundary value problem set in the functional space of regular solutions (i.e., that do not contain current sheets). This is an iterative method introduced by Grad and Rubin. It is associated with a well-posed boundary-value problem. We present some results obtained with this method on two exact solutions of the magnetostatic equations, used as theoretical magnetograms. Unlike some other extrapolations methods, that are associated with ill-posed boundary value problems, our method allows extrapolation to arbitrarily large heights, with no blowing up due to the presence in these methods of an intrinsic instability that makes errors growing up exponentially.

Key words: rodynamics (MHD) – Sun: corona – Sun: magnetic fields

1. Introduction

The magnetic field dominates most of the corona, and it is probably the origin of a large variety of structures and phenomena, such as flares, Coronal Mass Ejections, prominences and coronal heating (Priest 1982). Unfortunately the magnetic field is not yet observationally accessible in the tenuous and hot plasma that fills the corona (see Sakurai 1989, Amari & Demoulin 1992, and references therein). One possible familiar approach consists in solving the equations of a model (defined by some reasonable assumptions about the physical state of the corona) as a Boundary Value Problem (BVP), the boundary conditions being taken to be the measured values of the magnetic field in the denser and cooler photosphere: this is the so called *Reconstruction* problem of the coronal magnetic field. Many problems have been encountered since the early attempts of Schmidt (1964), as the observational problems to get rid of the ambiguity that remains in the transverse component of the photospheric magnetic field (Amari & Demoulin 1992, McClymont et al. 1997, and references therein), or the problems related to the choice of boundary conditions that make a well set BVP (Aly 1989)

In the simplest approximation the coronal magnetic field is current-free. This only requires the longitudinal component of the photospheric field as a boundary condition (Schmidt, 1964), and the solution can be computed using either a Green's function method or Laplace solver methods for the magnetic field or the vector potential. The mathematics of the various related BVPs (e.g., their well-(or ill-) posedness properties), are also known (Aly 1987, Amari et al. 1998).

In many active regions, where the magnetic configuration is known to have stored free energy, the current free assumption is not relevant. One can then introduced the so-called constant-α force-free hypothesis, which allows for the presence of electric currents in the corona. The magnetic field is computed, for a given value of α, from its longitudinal component by using either Fourier transform (Nakagawa et al. 1973, Alissandrakis 1981) or Green's function (Chiu & Hilton 1977, Semel 1988) techniques. Other spectral methods have been recently proposed (Boulmezaoud et al. 1998). It is also possible to solve it by regularizing an ill-posed BVP (in which the three components of the magnetic field are used) (Amari et al. 1998). However, the non-regularization or partial regularization of the so called Vertical Integration Method (VIM), leads in general to an amplification of errors (Wu et al. 1990 and referncess therein, Cuperman et al. 1990a-b, Cuperman et al. 1991, Demoulin et al. 1992). In addition the total energy of the linear force-free field in an unbounded domain such as the exterior of a star shaped domain is infinite, and is in general infinite in the case of the upper half space (except for some particular periodic solution satisfying some special conditions, Alissandrakis 1981, Aly 1992). Moreover the electric currents are uniformly distributed, while observations clearly show strong localized shear along the neutral line of many active region magnetic configurations (Hagyard 1988, Hofmann & Kalman 1991).

Send offprint requests to: T. Amari

Modeling such strong localized electric currents needs to assume that the coronal magnetic configuration is in a non-linear, force-free state. In this case one can distinguish two types of methods associated to different classes of BVPs, Extrapolation Methods and Reconstruction Methods. In the first class of methods the three components of the magnetic field are used as boundary conditions. The equations are thus vertically integrated step by step, from the photosphere towards the corona, without incorporating any type of asymptotic boundary conditions. This give rise to the VIM (Wu et al. 1990 and references therein, Cuperman et al. 1990a-b, 1991, Demoulin et al. 1992). This method, associated to an ill-posed boundary value problem, has not yet been proved to be convincingly regularized, still ending with an exponential growing of the errors with height, prohibiting extrapolation up to reasonable heights. The second class of methods considers a BVP that only requires the normal component of the field on the boundary (B_n) and the normal component of the electric current say, where $B_n > 0$. Now the problem is considered in the whole domain and the solution is globally sought. It has been tackled by the use of iterative methods introduced by Grad and Rubin (Grad & Rubin 1958, Sakurai 1981, Sakurai et al. 1985) and by the Resistive MHD Relaxation Method (Mikic & McClymont 1994, Jiao et al. 1997). Roumeliotis (1997) presented a Relaxation Method in which the three components of the magnetic field are used at the photospheric level. Another method (see Amari & Demoulin 1992), is the Method of Weighted Residuals (Pridmore-Brown 1981). This method is based on the minimization of two residuals, one associated with the Laplace force that has to vanish for a force-free magnetic field, and the other one with the difference between the directions of the observed transverse photospheric magnetic field and of the computed one. However, some aspects, such as the choice of test functions to be used for scalar products, as well as some other points concerning the definite positiveness of one functional to be minimized, are not yet clear. Other computational schemes such as collocation or least square methods have also been proposed in Amari & Demoulin (1992), but they have not been tested so far.

Sakurai (1981, 1985) presented a Green's function approach of the Grad-Rubin formulation. Practically, the standard Green-Function formulation is however numerically expensive, since at each step of the iterative scheme one would need to compute an integral over the whole volume to get the value of the magnetic field at each point! An alternative approach proposed by Sakurai (1981, 1985) is to discretize the integral involving the Green's function by introducing "finite-element"-like discretization for the electric currents. The process thus consists in starting from an initial current-free field line, putting current on it, and then retracing the correct perturbed field line carrying the electric current just put on. In this method, the field lines are discretized into a finite number of nodes (which define the degrees of freedom of the problem) and the nodes locations then become the unknowns of the problem for tracing the field lines. The latter are determined by solving a system of nonlinear algebraic equations, whose convergence is related in some sense to the absolute value of α, and has not been proved to hold for large values of α.

In this paper we consider another class of Grad-Rubin Methods that used the vector potential representation of the magnetic field. The paper is organized as follows. In Sect. 2 we present the general problem that is solved. In Sect. 3, we present the class of Grad-Rubin-like computational methods for solving the non-linear force-free case. We introduce in particular a new Vector Potential formulation in Sect. 4. We then present some results obtained with our method when applied to some particular known solutions in Sect. 5. Sect. 6 gathers concluding remarks.

It should be noted that a portion of the present study has been published in the proceeding of a conference (Amari et al. 1997).

2. The problem

The set of equations that describe the equilibrium of the coronal magnetic field in the half-space $\Omega = \{z > 0\}$, when plasma pressure and gravitational forces are neglected, are the well known force-free equations (Parker 1979):

$$\nabla \times \mathbf{B} = \alpha(\mathbf{r})\mathbf{B} \quad \text{in} \quad \Omega, \tag{1}$$

$$\nabla \cdot \mathbf{B} = 0 \quad \text{in} \quad \Omega, \tag{2}$$

in which $\alpha(\mathbf{r})$ as well as $\mathbf{B}$ are unknowns.

The analysis of set of characteristics curves of this system, which is in general nonlinear (Grad and Rubin 1958, Parker 1995), shows that this system has a mixed elliptic-hyperbolic type structure. This complex structure of the problem (already known in fluid mechanics as the Beltrami field equations) makes this problem a formidable task to solve, and still makes it an open field of research in applied mathematics (Laurence & Avellaneda 1993), even in bounded domains. Moreover the astrophysical constraints, as seeking a solution in a domain that may be unbounded as $\Omega = \{z > 0\}$ add another non-trivial difficulty.

This mixed nature implies the requirement of two types of boundary conditions:

- First of all, the elliptic part, resulting from the assumption that the RHS of Eq. (1) is given (the electric current), is rather well known, since it is nothing else than the Biot and Savart law, and just requires the value of B_n on $\partial\Omega$ to compute $\mathbf{B}$ in the whole domain, as expected for any elliptic problem:

$$B_n|_{\partial\Omega} = b_0, \tag{3}$$

  where b_0 is a given regular function.
- Then from Eqs. (1)-(2) one gets a hyperbolic equation for α (for $\mathbf{B}$ given):

$$\mathbf{B}.\nabla\alpha(\mathbf{r}) = 0, \tag{4}$$

  and therefore one may give the value of α in the part $\partial\Omega^+$ of $\partial\Omega$ where $B_n > 0$, say:

$$\alpha|_{\partial\Omega^+} = \alpha_0, \tag{5}$$

where α_0 is a given regular function. Note that this type of boundary condition is sufficient if one reasonably assumes that every field line of the coronal magnetic field has its two footpoints connected to the boundary $\partial\Omega$. Configurations having non-connected field lines (magnetic islands) would otherwise lead to the impossibility of transporting information from the boundary $\partial\Omega$ (Aly 1988).

Because Ω is unbounded, one may also require the asymptotic boundary condition:

$$\lim_{|\mathbf{r}|\to\infty} |\mathbf{B}| = 0. \tag{6}$$

3. Grad-Rubin approach

Let us follow the approach that was proposed by Grad and Rubin (1958). The previous underlying mixed elliptic-hyperbolic structure of the system of equations is exploited by introducing the following sequences of hyperbolic and elliptic linear BVPs:

$$\mathbf{B}^{(n)}.\nabla\alpha^{(n)} = 0 \quad \text{in} \quad \Omega, \tag{7}$$

$$\alpha^{(n)}|_{\partial\Omega^+} = \alpha_0\,, \tag{8}$$

and

$$\nabla\times\mathbf{B}^{(n+1)} = \alpha^{(n)}\mathbf{B}^{(n)} \quad \text{in} \quad \Omega, \tag{9}$$

$$\nabla\cdot\mathbf{B}^{(n+1)} = 0 \quad \text{in} \quad \Omega, \tag{10}$$

$$B_z^{(n+1)}|_{\partial\Omega} = b_0\,, \tag{11}$$

$$\lim_{|\mathbf{r}|\to\infty} |\mathbf{B}^{(n+1)}| = 0\,. \tag{12}$$

with $\mathbf{B}^0$ the unique solution of:

$$\nabla\times\mathbf{B}^0 = 0 \quad \text{in} \quad \Omega, \tag{13}$$

$$B_z^0|_{\partial\Omega} = b_0\,, \tag{14}$$

$$\lim_{|\mathbf{r}|\to\infty} |\mathbf{B}^0| = 0\,, \tag{15}$$

that is given by (Aly 1989):

$$\mathbf{B}^0 = \nabla\phi^0\,, \tag{16}$$

$$\phi^0(\mathbf{r}) = \frac{1}{2\pi}\int_{\partial\Omega} B_z(\mathbf{r}')\frac{dx'\,dy'}{|\,\mathbf{r}-\mathbf{r}'\,|}\,. \tag{17}$$

These sequences of problems must be proved to converge towards the solution of the original BVP defined by Eqs. (1) and (2) provided with the set of boundary conditions given by Eqs. (3),5). One can use them to address theoretical issues such as i) existence of solution ii) uniqueness iii) continuity of the solution with the respect to the boundary conditions. These three points define a well-posed BVP in the sense of Hadamard (1932) and has been discussed for other BVP associated to extrapolation methods (Low & Lou 1991, Amari et al. 1998). Note that the last point is important because of the presence of errors in the measurements of the photospheric magnetic field and of the possible non-force-free character of the field at the photospheric level, where pressure and dynamic forces can play a non-negligible role (Aly 1989, McClymont et al. 1997). Of course those three points depend on the functional space in which one seeks the solution, and in particular on the the regularity of the solution (Amari 1991).

Bineau (1972), considered this BVP in the Holder functional spaces (set of functions sufficiently regular and whose derivatives are also regular enough, Brezis 1983). The BVP is then proved to be well-posed when $\alpha < \alpha_c$. However, this proof rests on the following assumptions: (i) The domain Ω is bounded. (ii) The field $\mathbf{B}_0$ as well as $\mathbf{B}$ have a simple magnetic topology (then they must not vanish in Ω). It is however possible to show the existence of a solution for Ω bounded, in more general spaces (when $(\alpha,\mathbf{B}) \in L^\infty \times H^1(\Omega)$), that is in a functional space such that solution may admit separatrices surfaces, null points, and current sheets, (Boulmezaoud, Amari & Maday, in preparation). Uniqueness of the solution has not yet been proved.

4. A vector potential formulation

4.1. Gauge for B_n fixed on $\partial\Omega$

To ensure that $\mathbf{B}$ is divergence free (Eq. (2)) we use the vector potential representation for $\mathbf{B}$. Since in BVP (10)-(12) $B_n|_{\partial\Omega}$ is fixed, the vector potential $\mathbf{A}$ should be determined such that

$$\mathbf{B} = \nabla\times\mathbf{A} \quad \text{in} \quad \Omega, \tag{18}$$

$$B_n|_{\partial\Omega} = b_0 \tag{19}$$

This representation is not yet unique, since if $\mathbf{A}$ is a potential for $\mathbf{B}$ then:

$$\hat{\mathbf{A}} = \mathbf{A} + \nabla\phi \tag{20}$$

where ϕ is an arbitrary scalar function, is also a vector potential for $\mathbf{B}$. Uniqueness is obtained by the choice of a particular gauge. There are several possible choices (Dautray & Lions 1982), but these do not in general take into account Eq. (11) (one well known choice is for example $\nabla\cdot\mathbf{A} = 0$ and $A_n|_{\partial\Omega} = 0$).

Our gauge is fixed by imposing that $\mathbf{A}$ *is the unique vector potential such that*:

$$\mathbf{B} = \nabla\times\mathbf{A} \quad \text{in} \quad \Omega, \tag{21}$$

$$\nabla\cdot\mathbf{A} = 0 \quad \text{in} \quad \Omega, \tag{22}$$

$$\nabla_t\cdot\mathbf{A}_t = 0 \quad \text{on} \quad \partial\Omega \tag{23}$$

where the subscript t in ξ_t stands for the trace (when it exists) of the operator or the field ξ on the boundary (in particular in cartesian coordinates: $\nabla_t\cdot\mathbf{g} = \partial_i g_i + \partial_j g_j$ on the plane $\Sigma_k = \{\mathbf{r}\cdot\hat{n}_k = constant\}$ with $(i,j,k) := (x,y,z)$ and $\hat{n}_k$ standing for the unit vector normal to the current boundary plane Σ_k). Note also that one readily gets:

$$\partial_n\mathbf{A}_n = 0 \quad \text{on} \quad \partial\Omega, \tag{24}$$

where $\nabla_n(f) = \hat{n}\cdot\nabla f$. The proof that $\mathbf{A}$ is unique is straightforward since from Eqs. (20)-(23) one gets that ϕ is the unique solution of a Laplace equation:

$$\Delta\phi = 0 \quad \text{in} \quad \Omega, \tag{25}$$

$$\phi = \phi_0 \quad \text{on} \quad \partial\Omega \tag{26}$$

(note that ϕ_0 is also obtained once solving a Laplace equation on $\partial\Omega$, and is also unique once ϕ_0 is prescribed on the border Γ of the boundary $\partial\Omega$).

Then with this choice of Gauge, $\mathbf{A}$ is the unique vector potential that satisfies:

$$\mathbf{B} = \nabla \times \mathbf{A} \quad \text{in} \quad \Omega, \tag{27}$$

$$\nabla \cdot \mathbf{A} = 0 \quad \text{in} \quad \Omega, \tag{28}$$

$$\nabla_t \cdot \mathbf{A}_t = 0 \quad \text{on} \quad \partial\Omega \tag{29}$$

$$\mathbf{A}_t = \nabla^\perp \chi \quad \text{on} \quad \partial\Omega \tag{30}$$

$$\partial_n \mathbf{A}_n = 0 \quad \text{on} \quad \partial\Omega \tag{31}$$

where $\nabla^\perp$ is the operator defined on $\partial\Omega$ such that $\nabla^\perp \cdot \nabla = 0$ (i.e., $\nabla^\perp \chi = \nabla_t \chi \times \hat{n}$) and where χ is the unique solution of

$$-\Delta_s \chi = b_0 \quad \text{in} \quad \partial\Omega, \tag{32}$$

$$\chi = 0 \quad \text{or} \quad \partial_n \chi = 0 \quad \text{on} \quad \Gamma. \tag{33}$$

where Δ_s is the Laplacian operator on $\partial\Omega$ (i.e., $\Delta_s f := \nabla_t^2 f$)

4.2. BVP for A

One can then rewrite BVP(10)-((12) in terms of the potential vector $\mathbf{A}$ that is then the unique solution of the following BVP (referred to hereafter as BVP-A):

$$\nabla \times \mathbf{A}^{(n)} . \nabla \alpha^{(n)} = 0 \quad \text{in} \quad \Omega, \tag{34}$$

$$\tag{35}$$

$$\alpha^{(n)}|_{\partial\Omega^+} = \alpha_0 . \tag{36}$$

and

$$-\Delta \mathbf{A}^{(n+1)} = \alpha^{(n)} \nabla \times \mathbf{A}^{(n)} \quad \text{in} \quad \Omega, \tag{37}$$

$$\mathbf{A}_t^{(n+1)} = \nabla^\perp \chi \quad \text{on} \quad \partial\Omega. \tag{38}$$

$$\partial_n \mathbf{A}_n^{(n+1)} = 0 \quad \text{on} \quad \partial\Omega \tag{39}$$

$$\lim_{|\mathbf{r}| \to \infty} |\mathbf{A}^{(n+1)}| = 0. \tag{40}$$

The solution $\mathbf{A}^{(n+1)}$ of the linear elliptic mixed Dirichlet-Neumann BVP is in general regular ($\mathbf{A}^{(n+1)} \in C^2(\Omega) \cup C^1(\partial\Omega)^3$).

One can then prove that:

$$\forall n \geq 1 ;, \mathbf{A}^{(n)} \quad \text{satisfies} \quad \nabla \cdot \mathbf{A} = 0 \quad \text{in} \quad \Omega,$$

Proof: Applying the operator $\nabla \cdot$ to both sides of Eq. (37) and using Eq. (2) for $\mathbf{B}^n$, one gets:

$$-\Delta(\nabla \cdot \mathbf{A}^{(n+1)}) = \nabla \cdot (\alpha^{(n)} \nabla \times \mathbf{A}^{(n)}) \tag{41}$$

$$= \nabla \times \mathbf{A}^{(n)} . \nabla \alpha^{(n)} = 0 \quad \text{in} \quad \Omega \tag{42}$$

$$\nabla \cdot \mathbf{A}^{(n+1)} = 0 \quad \text{on} \quad \partial\Omega, \tag{43}$$

Whence $\nabla \cdot \mathbf{A}^{(n+1)} = 0$ is the unique solution tending to zero at infinity for this BVP. Note that since the initial potential magnetic field $\mathbf{B}^{(0)}$ clearly satisfies $\nabla \cdot \mathbf{J}^{(0)} = 0$ (where $\mathbf{J}$ stands for the associated electric current), this property is preserved for all $n > 0$.

4.3. A two-level iteration procedure

Let us define the sequence $(\alpha_{0_p})_{1 \leq p \leq P}$ and the mononotic increasing sequence $(u_p)_{1 \leq p \leq P}$ such that:

$$\alpha_{0_p}(x) = u_p \alpha_0(x) \quad \text{for} \quad x \in \partial\Omega, \tag{44}$$

$$u_1 = \epsilon, \tag{45}$$

$$u_P = 1, \tag{46}$$

where ϵ is a "small enough" real number, and P is a "large enough" integer.

One can then generate a more general sequence of linear BVP for $(\mathbf{A}_p^{(n)}, \alpha_p^{(n)})_{n \geq 1, 1 \leq p \leq P}$ given by:

$$\nabla \times \mathbf{A}_p^{(n)} . \nabla \alpha_p^{(n)} = 0 \quad \text{in} \quad \Omega, \tag{47}$$

$$\tag{48}$$

$$\alpha_p^{(n)}|_{\partial\Omega^+} = \alpha_{0_p}. \tag{49}$$

and

$$-\Delta \mathbf{A}_p^{(n+1)} = \alpha^{(n)} \nabla \times \mathbf{A}_p^{(n)} \quad \text{in} \quad \Omega. \tag{50}$$

$$\mathbf{A}_p{}_t^{(n+1)} = \nabla^\perp \chi \quad \text{on} \quad \partial\Omega. \tag{51}$$

$$\partial_n \mathbf{A}_p{}_n^{(n+1)} = 0 \quad \text{on} \quad \partial\Omega \tag{52}$$

$$\lim_{|\mathbf{r}| \to \infty} |\mathbf{A}_p^{(n+1)}| = 0. \tag{53}$$

One may initialize the iteration procedure for $p = 0$, with the unique solution of BVP(13)-(15) (which would be equivalent to choose $u_0 = 0$). A possible choice for $(u_p)_{1 \leq p \leq P}$ is for P given:

$$u_p = p \frac{1}{P}, \tag{54}$$

$$\tag{55}$$

One clearly notices that for every value of p one needs to solve a sequence of linear BVPs for all $n > 0$. This corresponds to a progressive injection of α at the boundary which turns out to improve convergence of the classical Grad-Rubin scheme.

4.4. Numerical implementation

We have developed a code called EXTRAPOL, based on the method described in the previous sections.

- i) The computational domain Ω is supposed to be the bounded cubic box $[0, Lx] \times [0, Ly] \times [0, Lz]$ (instead of the infinite upper half space), that we discretize as Ω_h using a non-uniform structured mesh for finite difference approximation. This staggered mesh used for the the various components of the vector potential $\mathbf{A}$, the magnetic field $\mathbf{B}$ and α, is the same as the one used in our MHD code METEOSOL used for three-dimensional dynamic evolution (Amari et al. 1996).
- ii) We use as a boundary condition for BVP (37)-(40) on the lateral and top boundaries of the box, $\mathbf{B}_n = 0$, which owing to our gauge choice (Eqs. (22)-23)) is equivalent to impose

on these boundaries:

$$\mathbf{A}_t = 0 \tag{56}$$

$$\partial_n \mathbf{A}_n = 0 \tag{57}$$

This type of boundary conditions, whose aim is to mimic the far field behaviour at infinity (as one would expect for the magnetic field in the actual infinite half-space), implies that the top and lateral boundaries of the box have to be chosen sufficiently far away from the main region of interest. This can be achieved at relatively low cost since our mesh is not uniform, and therefore large cells can be put in the far-field region.

- iii) The various differential operators (Eqs. (47)-(53)) are then dicretized on this mesh to second order accuracy. The Laplacian operator (in the Dirichlet-Neuman BVP (50)-(53)) leads to a 7 diagonal sparse positive definite matrix. The corresponding linear system is solved by use of an iterative method, in which the matrix is not stored but the matrix-vector product is generated explicitly by the operator (and only one more array is stored for building a preconditioner to accelerate the convergence of the method). This memory space saving allows the method to be implemented on a workstation with reasonable central memory size, and not only on supercomputers. We actually run the code on both machine types although the results presented here correspond to runs performed on a CRAY C90 machine.
- iv) The numerical solution of Eqs. (47)-(49) is performed by using a characteristics method approach, since those curves are the field lines. Let $(\mathbf{X}; s)$ be the characteristics, solution of

$$\mathbf{X}' = \mathbf{B}(\mathbf{X}), \mathbf{X}(0) = \mathbf{q} \tag{58}$$

for $\mathbf{q}$ given in Ω_h (the prime symbol standing for differentiation with respect to the parameter that runs along the characteristics). Then for any node $\mathbf{q}_h \in \Omega_h$ on which α is defined, one gets α_h as

$$\alpha(\mathbf{q}_h) = \alpha_0(\mathbf{X}_{\partial\Omega^+}(\mathbf{q}_h)) \tag{59}$$

where $\mathbf{X}_{\partial\Omega^+}(\mathbf{q}_h) = \mathbf{X}(\mathbf{q}_h, s_{\partial\Omega^+})$ is the intersection of $\{\mathbf{X}(\mathbf{q}; s) : s < 0\}$ with $\partial\Omega^+$. Since α_0 is known at the nodes that do not in general coincide with $\alpha_0(\mathbf{X}_{\partial\Omega^+}(\mathbf{q}_h))$, an interpolation from its four nearest neighbors eventually gives $\alpha(\mathbf{q}_h)$. We have then derived two methods: **a)** In the first one, once a step is chosen for field line integration, one goes backwards along the characteristics using a second order predictor-corrector scheme. Clearly one can save computation time by avoiding going back up to $\partial\Omega^+$. This is achieved by marking the nodes in the domain where α has already been computed, and then linearly interpolating α from its nearest neighbors as soon as the current node is surrounded by such marked nodes. **b)** In a second method (Pironneau 1988) one avoids fixing a step by using a slightly less accurate scheme that consists in going backwards along the characteristics following the faces of each cubic cell that is centered on an α-node, approximating the characteristic curve by a polygonal line made of the segments $[\mathbf{q}^k, \mathbf{q}^{k+1}]$ where $\mathbf{q}^0 = \mathbf{q}_h$ and $\mathbf{q}^{k+1}$ is the intersection of the line $\{\mathbf{q}^k - \mu\mathbf{B}(\mathbf{q}^k)\}_{\mu>0}$ with the boundary ∂C_m of the cubic α-cell C_m that contains $\mathbf{q}^k$ and $\mathbf{q}^k - \eta\mathbf{B}(\mathbf{q}^k)$ (with $\eta > 0$). This method is then faster than the previous one since there is no step size to be fixed a priori. Unlike for the first method, in a non-uniform mesh, each cell is crossed in 'one step' only, which makes this method faster in the big cells region. Despite this difference in the computational speed we have kept the two methods available because of their slight accuracy difference.

5. Application to some known exact force-free solutions

We now test the scheme presented in the previous section by running our code EXTRAPOL on some analytical and semi-numerical exact solutions of the non linear force-free equations Eq. (1)-(2). The boundary values of these exact solutions are used as simulated magnetograms. Hopefully, in these cases one knows the solution above in the domain too, and compare the reconstructed and the exact solutions (which is not the case for the actual corona!). There are only very few known exact solutions of the force-free equations. Let us presents the results obtained with our code on two cases that have been also used by other methods such as the VIM (Demoulin et al. 1992) for the first one and the Resistive Relaxation Method (Mikic & McClymont 1994) for the second one. Note that another class of related solutions that will not be tested here are those found by Cuperman & Ditkowski (1991).

5.1. The Low (1982) solution

Our first target is the well-known solution of Low (1982) for which the magnetic field $\mathbf{B}$ is given by:

$$B_x = -\frac{B_0}{r}\cos\phi(r), \tag{60}$$

$$B_y = \frac{B_0 x_1 y_1}{r\rho^2}\cos\varphi(r) - \frac{B_0 z_1}{\rho^2}\sin\phi(r), \tag{61}$$

$$B_z = \frac{B_0 x_1 z_1}{r\rho^2}\cos\phi(r) + \frac{B_0 y_1}{\rho^2}\sin\phi(r), \tag{62}$$

where $x_1 = x - \frac{L_x}{2}$, $y_1 = y - \frac{L_y}{2}$, $z_1 = z + 1$, $\rho^2 = y_1^2 + z_1^2$, $r^2 = x_1^2 + \rho^2$. The generating function $\phi(r)$ is related to $\alpha(r)$ by:

$$\alpha(r) = -\phi'(r) \ . \tag{63}$$

We choose for the function ϕ

$$\phi(r) = r_0\alpha_m \tanh(r/r_0), \tag{64}$$

which owing to Eq. (63) gives:

$$\alpha(r) = -\frac{\alpha_m}{\tanh(r/r_0)} \ . \tag{65}$$

We fix hereafter $r_0 = 4$ and $\alpha_m = 0.2$

Our numerical box size corresponds to the choice $L_x = 48$, $L_z = 48, L_z = 48$. A non-uniform mesh with $51 \times 51 \times 51$ nodes was chosen as in Demoulin et al. (1992). The analytical solution is then computed on the mesh and in particular the values taken by B_z and α on the boundary provide boundary conditions for our force-free reconstruction procedure. We choose $P = 25$ in Eq. (53) (i.e., the parameter necessary to fix the outer iteration corresponding to the injection of α_0). Our method converges up to a Lorentz force of order 10^{-3} for a number of inner Grad-Rubin iterations $N_{iterations} = 6$. The numerical error is defined as in Amari et al. (1998). We also found that choosing $P = 15$ implies increasing $Ngradrub$ up to about 12 to reach a Lorentz force of the same order. Fig. 1 shows some field lines of the exact solution (top) and the the corresponding field lines obtained from our computation.

Some discrepancies (up to few percents) between the exact and the computed solution are found in the domain, and these can reach almost .2 for the field lines approaching the lateral boundaries of the box. These can be explained by our choice for the boundary condition ($B_n = 0$) on these boundaries for the computed solution, while the exact solution does not decrease fast enough and even more pathologically in the horizontal plane (see Amari et al. 1998). Note that because applying this boundary condition results in a difference between the computed and exact solution, but still allows to reach a force-free equilibrium. However this equilibrium shows a different behaviour than the exact solution near the boundary, but there is no intrinsic instability as in the VIM (Wu 1990 and references therein, Cuperman et al. 1990a-b, Demoulin et al.1992). It is worth noting that we have also performed some higher resolution run, with $Nx = 101, Ny = 101, Nz = 101$ which, unlike the VIM, gave even better results, allowing the boundaries to be pushed far away. Note that this "robustness" property (good behaviour while increasing spatial resolution) as well as the convergence of the method even for this type of lateral and top boundary conditions results from the well-posed formulation we have adopted, unlike for the VIM which is associated to an ill-posed mathematical problem (see Low & Lou 1991 and Amari et al. 1998). In this latter method errors increase exponentially with height (Demoulin et al. 1992) and this is a property intrinsic to the method (and not the numerical scheme used for the extrapolation), which implies that the computed solution will eventually diverge, while our solution never diverges for an arbitrarily large box. Actually the bigger is our box, the bigger the region of agreement between our solution and the exact one is, a property that we checked with the higher resolution run, pushing the lateral boundaries to $L_x = 120$, $L_z = 120$, $L_z = 120$.

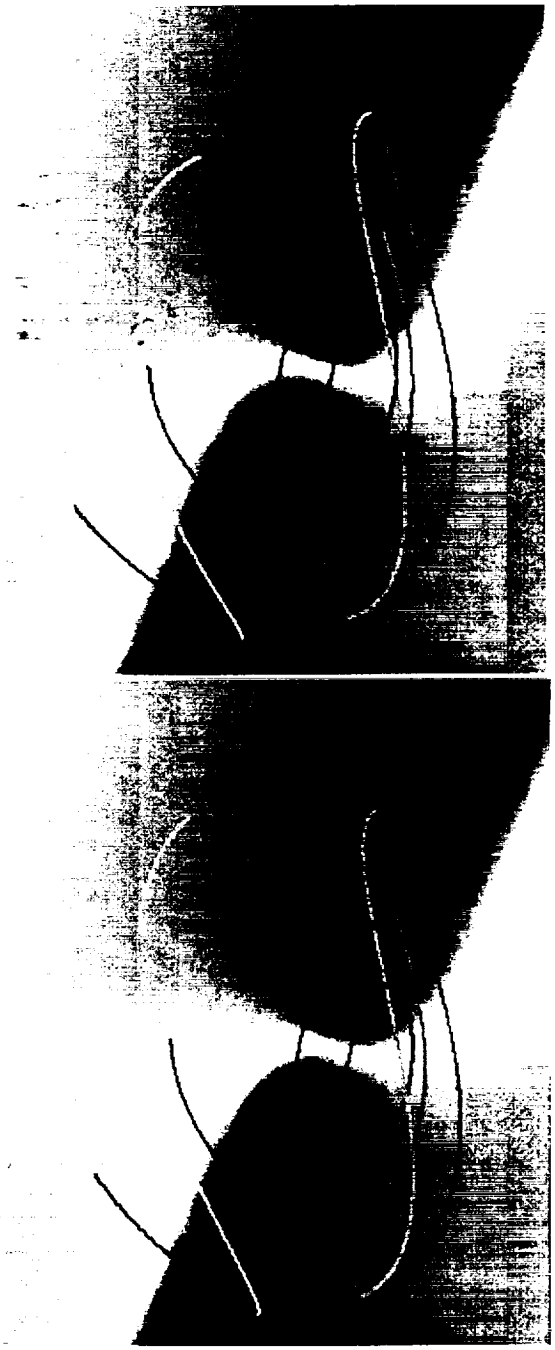

Fig. 1. Example of force-free reconstruction with the Vector Potential Grad Rubin Method compared to the exact analytical Low's (1982) solution. The computed solution (*bottom*), matches the exact solution (*top*) up to few percents in most of the interior of the computational box. Some discrepancies occur for field lines near the lateral and top boundaries because of the slow asymptotic decreasing behaviour of this particular solution, while the boundary condition $B_n = 0$ has been imposed on the boundaries in the computation.

5.2. Low & Lou's (1991) solution

We have also tried the particular case of the exact force-free solution presented in Low & Lou (1991). Unlike Low's (1982) solution, it requires some numerical calculations.

The solution is supposed to be axi-symmetric and writes in spherical coordinates:

$$B_r = \frac{1}{r^2 \sin\theta} \frac{\partial A}{\partial \theta} , \quad (66)$$

$$B_\theta = -\frac{1}{r \sin\theta} \frac{\partial A}{\partial r} , \quad (67)$$

$$B_\phi = \frac{1}{r \sin\theta} Q , \quad (68)$$

where $Q(A)$ is an a priori unknown function of $A(r,\theta)$, a solution of the nonlinear partial differential equation (see Low & Lou 1991). A family of solutions can be generated by choosing

$$A = \frac{P(\cos\theta)}{r^n} , \quad (69)$$

$$Q = aA^{1+\frac{1}{n}} , \quad (70)$$

for odd n, and a a real constant. P is then the solution of the following boundary-value problem:

$$(1-\cos^2\theta)\frac{d^2P}{d(\cos\theta)^2} + n(n+1)P + a^2\frac{1+n}{n}P^{1+\frac{2}{n}} = 0 , \quad (71)$$

$$P(-1) = P(1) = 0 . \quad (72)$$

We then solve numerically Eqs. (71)- (72). Usual transformations (Low & Lou 1991) then allow to get the solution in cartesian coordinates, in the upper half space.

Our numerical box is taken such that $L_x = 8$, $L_z = 8$, $L_z = 4$. A non-uniform mesh is generated with $N_x = 60$, $N_y = 60$, $N_z = 40$ with most of the cells concentrated in the inner stronger field region. Once BVP (71)-(72) is solved, one deduces the corresponding three components (B_x,B_y,B_z), the associated electric currents and $\alpha = \frac{dQ}{dA}$ on the same nodes (x_h, y_h, z_h) of the mesh used by our force-free reconstruction code EXTRAPOL, and then computes the solution. One then use $B_z(x_h, y_h, 0)$ and $\alpha(x_h, y_h, 0)$ (for the nodes in $\partial\Omega^+$ only) as boundary condition for the reconstruction procedure. We found that using $P = 20$ and 4 inner iterations($N_{iterations} = 4$) allows to decrease the Lorentz force down to values of order 10^{-3}.

Fig. 2 shows some field lines of the exact solution (top) and the corresponding field lines resulting from our reconstruction procedure. The errors, defined as for the previous case (Low's (1982) solution), are even less or of the order of 1% in the larger part of the domain, except again near the lateral and top boundaries where the imposed boundary condition $B_n = 0$ and the exact one disagree. Actually, those discrepancies are however smaller than those of the case of Low's (1982) model for the lateral boundaries because the magnetic field now decreases faster with distance. The case of the top boundary is different because of the existence, in the exact solution, of a pathological field-line in the center of the box that crosses almost vertically the top boundary while it has to match the applied boundary condition $B_n = 0$ in the calculation, which will be difficult to fulfill, even with a large box. Note that despite the much better asymptotic behaviour of this force-free solution for the magnetic field the electric currents are distributed on a scale that is still large, which results in a configuration that does not quickly approach

Fig. 2. Non linear force-free reconstruction (with the Vector Potential Grad Rubin Method) of the semi-numerical exact solution of Low & Lou (1990). The computed solution (*bottom*), and the exact solution (*top*) agree in most of the computed area. The existence of a pathological field line (in the exact solution) that crosses almost perpendicularly the top boundary, implies larger errors near this boundary since the computed solution corresponds to the boundary condition $B_n = 0$. The boundaries of the box are put far away enough from the inner stronger field area.

toward the potential field as it is often the case in the corona, outside regions of more localized electric currents.

6. Conclusions

In this paper, we have presented a numerical method for reconstructing the coronal magnetic field as a force-free magnetic field from its value given on the boundary of the domain. Let us summarize here the main points we have discussed and our main results:

(a) The boundary-value problem is formulated such that it corresponds to a well-posed mathematical problem: the normal component of the magnetic field is imposed on the boundary of the domain, and α only on that part of this boundary where $B_n > 0$. We impose $B_n = 0$ on the lateral boundaries so that α does not need to be specified on these boundaries, provided that these boundaries are put far enough to mimic the behaviour of the solution at infinity.

(b) We have derived a Grad Rubin Vector Potential formulation of this BVP to ensure div $\mathbf{B} = 0$ up to machine roundoff numerical errors. We have shown that this problem may be equivalent to solve a sequence of linear elliptic boundary-value problems for the Vector Potential, and hyperbolic ones for α. This current formulation is relevant for seeking regular enough solutions but not equilibria having current sheets. Weak formulations of these methods are however currently under study and would be reported in a next Paper of the series (Amari & Boulmezaoud 1999, in preparation). We have implemented this method in our computational code EXTRAPOL, in a relatively efficient numerical way. Other mathematical approaches allowing the existence of critical points in the configuration are also currently studied.

(c) We have successively applied our method to theoretical magnetograms obtained from two exact known solutions, the solutions of Low (1982) and Low & Lou (1991). The method converges up to a small residual Lorentz force, in a reasonable number of iterations. Some discrepancies between the exact solution and the reconstructed one occurred near the top or lateral boundaries of the computational box, and have been explained by the relatively bad asymptotic behaviour of Low's (1982) solution, or the existence of an almost vertical pathological field line in the solution of Low & Lou (1991), which makes difficult to match our applied boundary conditions on these boundaries ($B_n = 0$). Other approaches involving the assumption of potential field near the boundaries, or approximation of the Green formulae that can explicitly give the normal component at those boundaries are currently under development. Another approach could be to map the infinite upper half-plane onto the bounded square box by using a class of mappings that represent the generalization of conformal mappings used in two dimensions.

(d) Our formulation is better than the (VIM) (Wu 1985, Cuperman et al. 1990a-b, Demoulin et al.1992) since it corresponds to a mathematically well-posed boundary value problem. Although it may exhibit some residual discrepancies with the exact known solution, errors never increase exponentially up to blowing up as in the VIM. Moreover as it was shown by Bineau (1972) another consequence is that the solution is expected to be continuous respect to boundary conditions, at least for α not to large (Amari et al. 1998).

(e) Our method is different from Sakurai's (1981) approach in which, instead of solving an elliptic problem for $\mathbf{B}$, he uses a more local approach where the location of the nodes that discretize a given field line are computed once some electric currents (α) are injected in this field line, as the solution of non-linear system of equations that does not take into account the contribution of the whole computational domain (as one would expect in an elliptic problem). This approach allows a fast enough computation, which might be useful for some very concentrated (almost thin isolated) tube-like configurations, but it is not yet clear how this truncation procedure (by solving a single problem for each field line) may be involved in the numerical instabilities encountered in solving the nonlinear system for cases corresponding to large values of α. Indeed Sakurai's (1981) approach might be considered as a Lagrangian discretization method while we have presented a Eulerian type discretization that would be more suited to highly sheared magnetic configurations. The two methods should be worth to be kept and used for different types of data and configurations. The results presented in this Paper seem to be optimistic as regards the application of the method to simulated magnetograms. The next step currently under development is the application of this method to various sets of data provided by vector magnetographs. However there are several important points that need to be emphasized, and that make actual data much more difficult to handle than exact force-free solutions:

i) First of all data are much more noisy, because of the errors on the transverse magnetic field measurements that are larger than on the longitudinal one (Amari & Demoulin 1992, Klimchuk & Canfield 1993, McClymont et al. 1997). Other errors may also arise after the resolution of the 180° ambiguity that exists on the transverse component. These errors depend on the method that is used (Mikic & Amari 1999, in preparation). Eventually the non-force-free character of the photosphere (Aly 1989) may be taken into account. Actually from point (b) above, the well-posedness of our formulation (for at least α not too large), would make the solution not very sensitive to errors expected on the photospheric measurements. We are currently working on the project of simulating the error effects (Amari et al. 1999, in preparation) of these instrumental errors on the transverse field components, by introducing some random noise in the simulated data obtained from some highly sheared force-free solutions obtained by a relaxation code (Yang et al. 1986, Klimchuk & Sturrock 1992), and then reconstructing them with our method.

ii) Related to these errors, one may also find that, unlike theoretical magnetograms, actual data are far from smooth. This implies that any reconstruction method should be either robust or one will have to smooth the data prior to reconstruction, which may introduce possible added deviations from the sought solution, since there is no unique way of smoothing.

iii) One non negligible difficulty that has to be taken into account is the needs for computing α from the photospheric normal

components of the magnetic field and of the electric current. Weak field regions cannot be ruled out in a straightforward way since high shear can be localized near the neutral line (Hagyard 1988).

iv) One final point is that unlike for theoretical magnetograms, one never knows a priori the solution in the corona in order to check the reconstructed one. However an alternative can be the use of YOHKOH or SOHO/EIT data (for different heights). These data would have to be used a posteriori to check if the computed structures has such loops or "footpoints" that match the coronal observed ones, but not use these data set to fix a remaining free parameter such as α in linear force-free constant-α extrapolations!

Acknowledgements. The numerical computations presented in this paper have been performed on the CRAY supercomputers of the Commissariat à l'Energie Atomique and the Institut I.D.R.I.S of the Centre National de la Recherche Scientifique. This work benefits from a NATO Collaborative Research Grant support.

References

Alissandrakis C.E., 1981, A&A 100, 197
Aly J.J., 1987, Sol. Phys. 111, 287
Aly J.J., 1988, Internal communication. Saclay.
Aly J.J., 1989, Solar Phys. 120, 19
Aly J.J., 1992, Solar Phys. 138, 133
Amari T., 1991, In: Priest E.R., Hood A.W. (eds.) Advances in Solar System Magnetohydrodynamics. Cambridge University Press, p. 173
Amari T., Aly J.J., Luciani J.F., Boulmezaoud T.Z., Mikic Z., 1997, Solar Phys. 174, 129
Amari T., Boulmezaoud T.Z., Maday Y., 1998, A&A 339, 252
Amari T., Démoulin P., 1992, In: Proceedings of the Workshop: Méthodes de détermination des champs magnétiques solaires et stellaires. Observatoire de Paris, p. 187
Amari T., Luciani J.F., Aly J.J., Tagger M., 1996, ApJ 466, L39
Bineau M., 1972, Comm. Pure and Applied Math. 25, 77
Boulmezaoud T.Z., Amari T., Maday Y., 1998, SIAM. Scientific. Computing., submitted
Brezis H., 1983, Analyse Fonctionnelle, Theorie et applications. Masson, Paris
Chiu Y.T., Hilton H.H., 1977, ApJ 212, 873
Cuperman S., Ofman L., Semel M., 1990a, A&A 227, 227
Cuperman S., Ofman L., Semel M., 1990b, A&A 230, 193
Cuperman S., Démoulin P., Semel M., 1991, A&A 245, 285
Dautray R., Lions J.L., 1982, Analyse mathématiques et calcul scientifique. Masson, Paris
Démoulin P., Cuperman S., Semel M., 1992, A&A 263, 351
Grad H., Rubin H., 1958, In: Proc. 2nd Intern. Conf. on Peaceful Uses of Atomic Energy. Vol. 31, United Nations, Geneva, p. 190
Hadamard J., 1932, Le problème de Cauchy et les equations aux dérivées partielles linéaires hyperboliques. Herman, Paris
Hagyard M.J., 1988, Solar Phys. 115, 107
Hofmann A., Kalman B., 1991, A&A 241, 203
Jiao L., McClymont A.N., Mikic Z., 1997, Solar Phys. 174, 311
Klimchuk J.A., Canfield R.A., 1993, In: Simon G.W., Balasubramian K.S. (eds.) Proc. 14th NSO/SP Int. Summer Workshop, Solar Active Region Evolution: Comparing Models with Observations. ASP, San Fransisco, 23
Klimchuk J.A., Sturrock P.A., 1992, ApJ 385, 344
Laurence P., Avellaneda M., 1993, Geophys. Astrophys. Fluid Dynamics 69, 241
Low B.C., 1982, Solar Phys. 77, 43
Low B.C., Lou Y.Q., 1991, ApJ 352, 343
McClymont A.N., Jiao L., Mikic Z., 1997, Solar Phys. 174, 191
Mikic Z., McClymont A.N., 1994, In: Balasubramaniam K.S., Simon G. (eds.) Solar Active Region Evolution - Comparing Models with Observtions. ASP Conf Series
Nakagawa Y., Raadu M.A., Harvey J.W., 1973, Solar Phys. 30, 421
Parker E.N., 1979, Cosmical magnetic fields. Oxford University Press, New York
Parker E.N., 1995, Spontaneous current sheets in magnetic fields, with applications to stellar X rays. Oxford University Press, Oxford
Pironneau 0., 1988, Méthodes des éléments finis pour les fluides. Collection Recherches en Mathématiques Appliquées, Masson
Priest E.R., 1982, Solar Magnetohydrodynamics. D. Reidel Publishing Company, Dordrecht/Boston/Lancaster
Pridmore-Brown D., 1981, Aerospace report no ATR-81(7813)-1, The Aerospace Corporation, El Sequndo, CA
Roumeliotis G., 1997, ApJ 473, 1095
Sakurai T., 1981, Solar Phys. 69, 343
Sakurai T., 1989, Space Sci. Rev. 51, 11
Sakurai T., Makita M., Shibasaki K., 1985, In: Schmidt H.U. (ed.) Theoritical Problems in High Resolution Solar Physics. MPA-212, Max Planck-Institute, p. 312
Schmidt H.U., 1964, In: Physics of Solar Flares. NASA SP 50, p. 107
Semel M., 1988, A&A 198, 293
Wu S.T., Sun M.T., Chang H.M., Hagyard M.J., Gary G.A., 1990, ApJ 362, 698
Yang W.H., Sturrock P.A., Antiochos S.K., 1986, ApJ 309, 383

REPORT DOCUMENTATION PAGE

Form Approved
OMB No. 0704-0188

1. AGENCY USE ONLY (Leave Blank)	2. REPORT DATE	3. REPORT TYPE AND DATES COVERED
	March 22, 2000	Progress Report (Final) (6/16/98 - 8/15/99)

4. TITLE AND SUBTITLE
"The Structure and Dynamics of the Solar Corona" Final Progress Report

5. FUNDING NUMBERS
NAS5-96081

6. AUTHORS
Zoran Mikic

7. PERFORMING ORGANIZATION NAME(S) AND ADDRESS(ES)

Science Applications International Corporation
10260 Campus Point Drive MSW2M
San Diego, CA 92121-1578

8. PERFORMAING ORGANIZATION REPORT NUMBER
SAIC-00/8005:APPAT-239

9. SPONSORING/MONITORING AGENCY NAME(S) AND ADDRESS(ES)

NASA Headquarters Operation Office
Goddard Space Flight Center
Greenbelt, MD 20771

10. SPONSORING/MONITORING AGENCY REPORT NUMBER

11. SUPPLEMENTARY NOTES

12a. DISTRIBUTION/AVAILABILITY STATEMENT

12b. DISTRIBUTION CODE

13. ABSTRACT *(Maximum 200 words)*

This report details progress during the third year of our Space Physics Theory Contract. This is the Final Report.

14. SUBJECT TERMS
Solar Corona, Coronal Magnetic Field, Heliosphere, Magnetohydrodynamics

15. NUMBER OF PAGES
68

16. PRICE CODE

17. SECURITY CLASSIFICATION OF REPORT	18. SECURITY CLASSIFICATION OF THIS PAGE	19. SECURITY CLASSIFICATION OF ABSTRACT	20. LIMITATION OF ABSTRACT
UNCLASSIFIED	UNCLASSIFIED	UNCLASSIFIED	UL